5-1-2016

# Direct Dissolution and Electrochemical Investigation of Cerium and Uranium in Ionic Liquid

Janelle Droessler
*University of Nevada, Las Vegas*

# DIRECT DISSOLUTION AND ELECTROCHEMICAL INVESTIGATION OF CERIUM AND URANIUM IN IONIC LIQUID

By

Janelle Elizabeth Droessler

Bachelor of Science - Chemistry

Bachelor of Arts - Interdisciplinary Studies: Forensic Science

University of Nevada, Las Vegas

2009

A dissertation submitted in partial fulfillment

of the requirements for the

Doctor of Philosophy - Radiochemistry

Department of Chemistry and Biochemistry

College of Sciences

The Graduate College

University of Nevada, Las Vegas

May 2016

UNLV | GRADUATE COLLEGE

# Dissertation Approval

The Graduate College
The University of Nevada, Las Vegas

March 4, 2016

This dissertation prepared by

Janelle Elizabeth Droessler

entitled

Direct Dissolution and Electrochemical Investigation of Cerium and Uranium in Ionic Liquid

is approved in partial fulfillment of the requirements for the degree of

Doctor of Philosophy - Radiochemistry
Department of Chemistry and Biochemistry

David Hatchett, Ph.D.
*Examination Committee Co-Chair*

Kenneth Czerwinski, Ph.D.
*Examination Committee Co-Chair*

Ralf Sudowe, Ph.D.
*Examination Committee Member*

Patricia Paviet, Ph.D.
*Examination Committee Member*

Jacimaria Batista, Ph.D.
*Graduate College Faculty Representative*

Kathryn Hausbeck Korgan, Ph.D.
*Graduate College Interim Dean*

Abstract

Direct Dissolution and Electrochemical Investigation of Cerium and Uranium in Ionic Liquid

By

Janelle Elizabeth Droessler

Dr. Kenneth R. Czerwinski, Committee Co-Chair
Professor of Chemistry
Dr. David W. Hatchett, Committee Co-Chair
Professor of Chemistry
University of Nevada, Las Vegas

The solubility, coordination and speciation of f-elements in ionic liquids (ILs) has been the focus of numerous studies because the purely ionic systems have unique physical properties that can be exploited in comparison to aqueous, organic, or molten salt systems. Ionic liquids are thermally stable, have negligible vapor pressure, and are electrochemically stable at negative potentials that encompass the reduction potential of actinide species. Literature has suggested that the properties of ILs could potentially be utilized in the nuclear fuel cycle for separations and reprocessing. However, the solubility of f-elements in ILs has been significantly lower compared to traditional solvents. Additionally, further research is needed to understand the soluble f-element species in ILs and their electrochemical behavior.

Methods of direct dissolution for cerium carbonate and uranium carbonate and oxide species into the IL, n-trimethyl-n-butylammonium bis(trifluoromethanesulfonyl)imide [$Me_3N^nBu$][TFSI], were developed. These demonstrate pathways for introducing f-elements into ILs without the use of extra synthesis routes. The reduction/oxidation of soluble cerium and uranium (uranyl) species in IL is examined at Au, Pt, and GC (glassy carbon) electrodes. Multi-wave voltammetry is consistent with the reductive deposition from the IL solution. Scanning

electron microscopy (SEM) and energy dispersive X-ray spectroscopy (EDS) confirm the deposition of cerium and uranium species at Au electrodes.

Finally, an initial study of the separation of uranium from a lanthanide in ILs was attempted. The ability to electrodeposit and separate uranium from a mixture of uranium/neodymium in three ILs using electrochemical methods was investigated. The ILs contained the same TFSI anion and different cations. Electrochemical deposits obtained from the different ILs were rinsed and dissolved into 1 M $HClO_4$ for UV-Vis spectroscopy and ICP-AES analysis to determine the concentration of uranium relative to neodymium in the initial solutions and resulting deposits.

Many thanks to the following for funding support of this work.

1) Department of Energy National Nuclear Security Administration DE-NA0000979



2) Global Medical Isotope Systems (GMIS)

Acknowledgements

As my experience in grad school and research reaches the culmination, I have had a chance to reflect on the great fortune I have had to be shaped by so many incredibly gifted advisors and peers. To my co-advisors, Dr. Ken Czerwinski and Dr. David Hatchett, I thank you for the many ways each of you have taught me what you know and even more importantly, always supporting me along the way. I can only hope to continue growing and develop into as accomplished and respected an individual as yourselves.

I first entered the rad labs working alongside Edward Mausolf and Frederic Poineau, whose curiosity and drive are never ending and opened my eyes to an exciting area of chemistry. Thank you Ed, for all the stimulating scientific discussions and pushing me to join the program as well. Without you, I may have taken a different path. Another figure of inspiration and admiration for me has been Patricia Paviet, who provides an infectious attitude about the nuclear fuel cycle and education. In addition, I was lucky to work enough with some great peers, many of whom I also call a friend. I would also be remiss to not mention an outstanding team who helped make getting the research done possible: Trevor Low, Julie Bertoia, and Tom O'Dou.

Lastly, my deepest thanks and love goes to my family. I especially want to share my enduring admiration to my parents, Pamela and Ted Droessler, who have always led by example and provided endless support. It is because of you both that I have been able to invest in myself and my education, overcome obstacles to accomplish goals, and know that I am fortunate to find something I truly enjoy.

Table of Contents

Abstract ……..... iii

Acknowledgements ……..... vi

List of Tables ……..... xii

List of Figures ……..... xiv

List of Equations ……..... xxi

Chapter 1 – Introduction……..... 1

1.1 Motivation ..... 1

1.2 Overview of the Nuclear Fuel Cycle ..... 1

1.3 Overview of Ionic Liquids ..... 5

1.3.1 Solubility of f-elements in Ionic Liquids..... 6

1.3.2 Difficulties of f-element Chemistry in Aqueous Systems……. 7

1.3.3 Advantages of Ionic Liquids……..... 9

1.4 Applications of Ionic Liquids in the Nuclear Fuel Cycle……. 11

1.5 Organization of Dissertation……. 14

Chapter 2 – Experimental Methods ..... 16

2.1 Materials Synthesis ….. 16

2.1.1 $UO_2CO_3$ …….. 16

2.1.2 $U_3O_8$ ……..... 18

2.2 Lanthanide and Actinide Dissolutions ……. 20

2.2.1 Direct Dissolution of Cerium Carbonate …… 21

2.2.2 Direct Dissolution of Uranyl Carbonate and Uranium Oxide …… 22

2.3 Instrumentation and Analytical Methods..... 23
2.3.1 Ozone Generator ..... 23
2.3.2 Powder X-ray Diffraction (p-XRD)..... 25
2.3.3 Infrared Spectroscopy (IR) ..... 26
2.3.4 Ultraviolet-Visible Spectroscopy (UV-Vis) ..... 28
2.3.5 Liquid Scintillation Counting (LSC) ..... 30
2.3.6 Karl Fischer Titration..... 32
2.3.7 Electrochemical Methods …… 34
2.3.7.1 $Ag/Ag^+$ Non-Aqueous Reference Electrode ……..... 34
2.3.7.2 Cyclic Voltammetry ……..… 35
2.3.7.3 Amperometric Deposition ……..……..…… 37
2.3.8 Scanning Electron Microscopy (SEM) and Energy Dispersive X-ray Spectroscopy (EDS) ……... 38
2.3.9 Inductively Coupled Plasma – Atomic Emission Spectroscopy (ICP-AES) …..… 39
Chapter 3 – Electrochemical Study of Ferrocene, Acid, and Water in Ionic Liquid ……..... 41
3.1 Introduction ..... 42
3.2 Methods and Materials ..... 45
3.2.1 Chemicals and Solutions ..... 45
3.2.2 Preparation of the Reference Electrode and Ionic Liquid Samples ……..….. 46
3.2.3 Karl Fischer Titration …….. 46
3.2.4 Electrochemical Apparatus and Conditions..... 46
3.2.5 Water Reduction Using Dry Inert Gas and Molecular Sieves …… 47
3.2.6 Addition of HTFSI, Neutralizing, and Drying of Ionic Liquid ……...… 47

3.3 Effects on the Reference Electrode: A Study of Ferrocene, Acid, and Water in Ionic Liquid ……..…….….. 48

3.4 Electrochemical Determination of Water at an Au Electrode in Ionic Liquid……. 49

3.5 Conclusions …..……..... 59

Chapter 4 – Dissolution of Cerium Carbonate in Ionic Liquid and Electrochemical Studies ..... 61

4.1 Introduction ..... 61

4.2 Methods and Materials ..... 65

4.2.1 Chemicals and Solutions ……. 65

4.2.2 Karl Fischer Titration …….. 66

4.2.3 UV-Visible and IR Spectroscopy….....…….. 66

4.2.4 Electrochemical Apparatus and Conditions …… 67

4.2.5 Scanning Electron Microscopy and Energy Dispersive X-ray Spectroscopy (SEM/EDS) …….. 67

4.3 Direct Dissolution of $Ce_2(CO_3)_3 \cdot xH_2O$ into Ionic Liquid ……..…68

4.4 UV-Visible and IR Spectroscopy of Soluble Cerium in Ionic Liquid ..... 69

4.5 Electrochemistry of Soluble Cerium in Ionic Liquid ..... 74

4.6 Scanning Electron Microscopy and Energy Dispersive X-ray Spectroscopy (SEM/EDS) Analysis of Electrodeposits …….…...… 81

4.7 Conclusions …….. 84

Chapter 5 –Dissolution of Uranyl Carbonate and Uranium Oxide in Ionic Liquid and Electrochemical Studies ……..... 85

5.1 Introduction ..... 85

5.2 Methods and Materials ..... 90

5.2.1 Chemicals and Solutions ……. 90

5.2.2 Dissolution into Ionic Liquid ……..… 90

5.2.2.1 Uranyl Carbonate ……. 90

5.2.2.2 Uranium Oxide ($U_3O_8$) …… 91

5.2.3 Liquid Scintillation Counting ……. 93

5.2.4 Karl Fischer Titration ……...……... 93

5.2.5 UV-Visible Spectroscopy ……... 93

5.2.6 Electrochemical Apparatus and Conditions ……..... 94

5.2.7 Scanning Electron Microscopy and Energy Dispersive X-ray Spectroscopy (SEM/EDS) …….…… 94

5.3 Direct Dissolution into Ionic Liquid ..... 95

5.3.1 Uranyl Carbonate …… 95

5.3.2 Uranium Oxide ($U_3O_8$) ……..……. 97

5.4 UV-Visible Spectroscopy Results ..... 103

5.4.1 Uranyl Carbonate Dissolved in Ionic Liquid ..... 103

5.4.2 Uranium Oxide ($U_3O_8$) Dissolved in Ionic Liquid ..... 105

5.5 Electrochemistry …… 106

5.5.1 Voltammetry of Soluble Uranyl from Uranyl Carbonate Dissolved in Ionic Liquid ……..…… 106

5.5.2 Voltammetry of Soluble Uranyl from Uranium Oxide ($U_3O_8$) Dissolved in Ionic Liquid ……..……...… 113

5.6 Scanning Electron Microscopy and Energy Dispersive X-ray Spectroscopy (SEM/EDS) Analysis of Electrodeposits …….……. 115

5.7 Conclusions ..... 119

Chapter 6 – Initial Studies of Electrochemical Separation of Uranium from Neodymium in Ionic Liquids ..... 121

6.1 Introduction ..... 121

6.2 Methods and Materials ..... 124

6.2.1 Chemicals and Solutions ..... 124

6.2.2 Powder X-ray Diffraction ..... 125

6.2.3 Electrodeposition ..... 125

6.2.4 Extractions ..... 126

6.2.5 UV-Visible Spectroscopy ..... 126

6.2.6 Inductively Coupled Plasma – Atomic Emission Spectroscopy (ICP-AES) ..... 127

6.3 UV-Visible Spectroscopy of Soluble Uranium and Neodymium in Ionic Liquids ..... 127

6.4 Inductively Coupled Plasma – Atomic Emission Spectroscopy (ICP-AES) Results ..... 132

6.5 Conclusions ..... 135

Chapter 7 – Conclusions..... 136

References ..... 141

CurriculumVitae..... 153

List of Tables

**Table 1.** Composition of used nuclear fuel…… 2

**Table 2.** Reduction potentials of selected lanthanides and actinides in acidic aqueous solution…… 8

**Table 3.** Summary of the concentration of water in IL determined using Karl Fischer titration and the water concentration in each sample derived from the linear fit of plots for the water concentration as a function of the charge (Q) and peak current ($I_{pc}$) for the reduction of gold oxide (I′/II′) …….. 54

**Table 4.** Absorbance band assignments for the IR spectra of [$Me_3N^nBu$][TFSI] containing HTFSI and soluble Ce (10 mM and 100 mM). For comparison, the band assignments for [$Me_3N^nBu$][TFSI] from Solvionic are provided ……..… 72

**Table 5**. Summary of the proposed reactions and peak assignments for Au, Pt, and glassy carbon (GC) electrodes in IL containing HTFSI and soluble Ce ……..... 80

**Table 6.** Karl Fischer analysis of the water content of the dry and water-saturated [$Me_3N^nBu$][TFSI] before and after dissolution of $U_3O_8$ into the IL with oxidizing gas ..... 99

**Table 7.** Summary of the proposed reactions and peak assignments of an Au electrode in IL containing soluble $UO_2^{2+}$ and HTFSI ……..…….……. 108

**Table 8.** Melting point and viscosity of the ILs ……..... 124

**Table 9.** ICP-AES results presented as U:Nd ratios for each of the repeated electrodeposits at each potential (-1.2 V, -2.0 V, and -2.8 V) for the three ILs. The initial ration of U:Nd was also

determined from extractions. A separation factor (SF) is calculated ……...……...… 133

List of Figures

**Figure 1.** PUREX process flow sheet …… 4

**Figure 2.** The structure of [$Me_3N^nBu$] cation and [TFSI] anion ……. 10

**Figure 3.** Comparison of the electrochemical window at Pt, Au, and GC electrodes in 0.1 M $H_2O_4$ (dashed line) and the [$Me_3N^nBu$][TFSI] (solid line) …….. 10

**Figure 4.** Powder XRD comparison of the synthesized $UO_2CO_3$ against a database structure (Rutherfordine) ……...…. 18

**Figure 5.** Tube furnace set-up inside fume hood for $U_3O_8$ synthesis …….. 19

**Figure 6.** Powder X-ray diffraction pattern of $U_3O_8$ compared to the C2mm structure of $U_3O_8$ ……..……. 20

**Figure 7.** Ozone generation by corona discharge …… 24

**Figure 8.** Ozone production from Ozone Solutions OZV-8 from dry air …….....… 24

**Figure 9.** Schematic of an X-ray diffractometer …… 25

**Figure 10.** Diagram comparing excitation energy of a molecule by UV-Vis or IR light sources for spectroscopy ……..….. 27

**Figure 11.** Schematic of a UV-Vis spectrophotometer with a dual beam system …….. 29

**Figure 12.** Representation of the Mettler Toledo D-32 Karl Fischer coulometric titrator ……... 33

**Figure 13. (a)** graphical representation of cyclic voltammetry and the related electrochemical reactions as a result of applied potential, **(b)** typical cyclic voltammogram with assignment of cathodic and anodic peak potentials and currents ..... 35

**Figure 14.** Interaction of the electron beam within a sample producing secondary and backscatter electrons for SEM imaging and X-ray emissions for EDS spectroscopy …… 39

**Figure 15.** Cyclic voltammogram of 10 mM Ferrocene in [$Me_3N^nBu$][TFSI] containing **(a)** 0.089 %, **(b)** and 1.28 % water. **(c)** A background of [$Me_3N^nBu$][TFSI] containing 1.28 % water before the addition of ferrocene is provided for comparison. Scan rate 100 mV/s ……..…. 48

**Figure 16. (a)** Cyclic voltammogram of 10 mM Ferrocene in [$Me_3N^nBu$][TFSI] with 0.5 M HTFSI **(b)** and after adding sieves, 0.3778 % and 0.0583 % $H_2O$, respectively. **(c)** A background of [$Me_3N^nBu$][TFSI] containing 0.5 M HTFSI before the addition of ferrocene is provided for comparison. Scan rate 100 mV/s ……. 49

**Figure 17.** Cyclic voltammetry of gold electrode in [$Me_3N^nBu$][TFSI] containing increasing water. Scan rate 100 mV/s ……...…… 51

**Figure 18.** Linear fit of percent water in IL vs. charge under the peak. Reduction peak (solid circles), oxidation peak (open circles) ……..……... 53

**Figure 19.** Linear fit of percent water in IL vs. peak current. Reduction peak (solid circles), oxidation peak (open circles) ……..……. 53

**Figure 20. (a)** Cyclic voltammogram of water-saturated [$Me_3N^nBu$][TFSI], **(b)** after purging with dried nitrogen gas for 2 hours, **(c)** after purging with dried nitrogen gas for 4, 6, and 12 hours. Scan rate 100 mV/s ……... 55

**Figure 21. (a)** Cyclic voltammogram of water-saturated [$Me_3N^nBu$][TFSI], **(b)** after the first addition of molecular sieves, 2 hours, **(c)** after second and third additions of molecular sieves, 2 hours each. Scan rate 100 mV/s ……... 56

**Figure 22. (a)** Full scans and water determination at Au electrode of: initial dry [$Me_3N^nBu$][TFSI], **(b)** IL containing 0.5 M HTFSI, **(c)** neutralized, **(d)** final dried IL by molecular sieves. Scan rate 100 mV/s ……. 57

**Figure 23. (a)** The UV-Vis absorbance spectra of 10 mM Ce in [$Me_3N^nBu$][TFSI] containing 80 mM HTFSI and subsequent dilutions (2, 1, 0.5, 0.25, and 0.1 mM soluble Ce) versus a background of [$Me_3N^nBu$][TFSI] containing 80 mM HTFSI. The dilutions were achieved using [$Me_3N^nBu$][TFSI] containing 80 mM HTFSI. **(b)** Linear plot of the absorbance (254 nm) versus concentration of soluble Ce ……..….... 70

**Figure 24. (a)** IR absorbance spectra of [$Me_3N^nBu$][TFSI] containing 80 mM HTFSI (dashed line), and with 10 mM soluble Ce (solid line). **(b)** IR absorbance spectra of [$Me_3N^nBu$][TFSI] containing 800 mM HTFSI (dashed line) and with 100 mM soluble Ce (solid line) ……...…… 71

**Figure 25.** Cyclic voltammograms for **(a)** an Au disc electrode in [$Me_3N^nBu$][TFSI] containing 80 mM HTFSI (dashed line) and **(b)** an Au disc electrode in [$Me_3N^nBu$][TFSI] containing 80 mM HTFSI with 10 mM soluble Ce (solid line) from the direct dissolution. Scan rate = 50 mV/s ……... 74

**Figure 26.** Cyclic voltammograms for **(a)** Pt disc electrode in [$Me_3N^nBu$][TFSI] containing 80 mM HTFSI (dashed line), and **(b)** Pt disc electrode in [$Me_3N^nBu$][TFSI] containing 80 mM HTFSI with 10 mM soluble Ce (solid line) from the direct dissolution. Scan rate = 50 mV/s ……..……. 78

**Figure 27.** Cyclic voltammograms for **(a)** glassy carbon (GC) disc electrode in [$Me_3N^nBu$][TFSI] containing 80 mM HTFSI (dashed line), and **(b)** GC disc electrode in

[$Me_3N^nBu$][TFSI] containing 80 mM HTFSI with 10 mM soluble Ce (solid line) from the direct dissolution. Scan rate = 50 mV/s ……...……...……... 79

**Figure 28. (a)** The SEM image of a Ce species deposited on Au/mica electrode obtained from the cyclic voltammetry in [$Me_3N^nBu$][TFSI] containing 80 mM HTFSI and 10 mM soluble Ce. **(b)** EDS spectra of the thin Ce deposits. **(c)i.** EDS of thicker Ce deposits lightly after a single washing with ethanol and **(c)ii.** after four additional washings with ethanol ……..……..…… 83

**Figure 29.** Possible dissolution mechanism for $UO_2CO_3$ in [$Me_3N^nBu$][TFSI] ……..... 95

**Figure 30.** Total soluble U content from dissolution of 0.3 g $UO_2CO_3$ in 39.3 mL [$Me_3N^nBu$][TFSI] as a function of Ar degassing time. Concentration was determined based on liquid scintillation counting of $^{233}U$ in the solid …….……. 96

**Figure 31.** The IL before (left), during (middle), and after (right) dissolution of $U_3O_8$ ……..... 97

**Figure 32.** Rate of U3O8 dissolution into initially dry and water-saturated [Me3NnBu][TFSI] with the assistance of oxidizing gas (air feed gas, flow rate 1 L/min, ozone generator level 5). ……..……. 98

**Figure 33.** Comparison of the dissolution of U3O8 into dry Me3NnBuTFSI attempted with different feed gases for 72 hrs: Air, O2, N2, N2O. (flow rate 1 L/min, ozone generator level 5) ……..……..…. 101

**Figure 34.** UV-Vis absorbance spectra of 0.5 M HTFSI in water and in IL [$Me_3N^nBu$][TFSI]. Absorbance spectra after the direct dissolution of 50 mM $UO_2CO_3$ into deionized water and IL [$Me_3N^nBu$][TFSI] containing 0.5 M HTFSI …….……. 104

**Figure 35.** UV-Vis absorbance of soluble uranyl following the dissolution of $U_3O_8$ into dry $[Me_3N^nBu][TFSI]$, 25.2 mM $UO_2^{2+}$. For comparison, there also are absorbance spectra of dry $[Me_3N^nBu][TFSI]$ before and after being exposed to the oxidizing gas from the ozone generator for 120 hrs to simulate conditions of dissolution ……..…….. 106

**Figure 36.** Cyclic voltammetry of an Au electrode in soluble $UO_2CO_3$ (50 mM) in IL $[Me_3N^nBu][TFSI]$ containing 0.5 M HTFSI in the potential range between **(a)** 2.4 to -0.2 V, **(b)** 2.4 to -1.1 V and, **(c)** 2.4 to -2.1 V. Cyclic voltammetry of an Au electrode in IL $[Me_3N^nBu][TFSI]$ containing 0.5 M HTFSI in the potential range between 2.4 to -2.1 V is provided for comparison (dashed line). Electrode area = 7.07 x $10^{-2}$ $cm^2$, scan rate = 50 mV/s ……..…...… 107

**Figure 37.** Sequential cyclic voltammetry of an Au electrode in soluble $UO_2CO_3$ (50 mM) in IL $[Me_3N^nBu][TFSI]$ containing 0.5 M HTFSI in the potential range between 2.4 to -1.1 V for the first ~10 cycles. Cyclic voltammetry of an Au electrode in IL $[Me_3N^nBu][TFSI]$ containing 0.5 M HTFSI in the potential range between 2.4 to -2.1 V is provided for comparison (dashed line). Electrode area = 7.07 x $10^{-2}$ $cm^2$, scan rate = 50 mV/s …….…… 110

**Figure 38.** Sequential cyclic voltammetry of an Au electrode in soluble $UO_2CO_3$ (50 mM) in IL $[Me_3N^nBu][TFSI]$ containing 0.5 M HTFSI in the potential range between 2.4 to -2.1 V for the first ~4 cycles. Cyclic voltammetry of an Au electrode in IL $[Me_3N^nBu][TFSI]$ containing 0.5 M HTFSI in the potential range between 2.4 to -2.1 V is provided for comparison (dashed line). Electrode area = 7.07 x $10^{-2}$ $cm^2$, scan rate = 50 mV/s. **Inset**: Expansion of the reduction of gold oxide region for successive cycles during the deposition processes ……. 111

**Figure 39.** Cyclic voltammetry of an Au electrode in soluble $UO_2CO_3$ (~5 mM) in IL $[Me_3N^nBu][TFSI]$ containing 0.1 M HTFSI, as a function of scan rate (10, 25, 50, 75, 100 mV/s are shown for clarity) from +2.3 V to 0 V vs. Ag/AgCl. **Inset**: Plot of peak current versus the square root of the scan rate for scan rates of 5, 10, 25, 50, 75, 100, and 250 mV/s. Electrode area = 7.07 x $10^{-2}$ $cm^2$ ……...……. 112

**Figure 40.** Cyclic voltammetry of an Au electrode in soluble $UO_2^{2+}$ (25.2 mM) in IL $[Me_3N^nBu][TFSI]$ from the dissolution of $U_3O_8$ in the potential range between **(a)** 2.4 to -0.1 V, **(b)** 2.4 to -1.1 V, **(c)** 2.4 to -2.1 V, and **(d)** 2.4 to -2.6 V. Cyclic voltammetry of an Au electrode in IL $[Me_3N^nBu][TFSI]$ exposed to the ozone generator with air feed gas for 120 hrs in the potential range between 2.4 to -2.6 V is provided for comparison as a background (dashed line). Electrode area = 7.07 x $10^{-2}$ $cm^2$, scan rate = 100 mV/s ……...…. 114

**Figure 41.** Cyclic voltammetry of an Au electrode in soluble $U_3O_8$ (~50 mM) in IL $[Me_3N^nBu][TFSI]$ containing 0.1 M HTFSI, as a function of scan rate (10, 25, 50, 75, 100 mV/s are shown for clarity) from + 0.9 V to 0.3 V vs. Ag/AgCl. **Inset**: Plot of peak current versus the square root of the scan rate. Electrode area = 7.07 x $10^{-2}$ $cm^2$. Initial scan direction is from positive to negative potential ……. 115

**Figure 42.** SEM of **(a)** an Au electrode prior to electrochemical deposition, and after electrodeposition of uranium species from $UO_2CO_3$ dissolved into $[Me_3N^nBu][TFSI]$ containing 0.5 M HTFSI, **(b)** at x100 magnification, and **(c)** at x 500 magnification ……..116

**Figure 43.** EDS analysis of the U surface deposits on Au from Figure 42, with species labeled. The dashed line represents the EDS spectrum of the clean Au surface ……..... 117

**Figure 44.** Images of **(a)** an Au electrode after deposition of uranium species from $U_3O_8$ dissolved into $[Me_3N^nBu][TFSI]$ containing 3.27 M HTFSI **(b)** SEM at x35 magnification of the

deposit and **(c)** at x1000 magnification. Deposition for 48 hours at E = -1.8 V vs Ag/AgCl ……...…….. 118

**Figure 45.** EDS analysis of the U surface deposits on Au from Figure 44, with species labeled ..……...……..... 119

**Figure 46.** Cations (Left to right): n-trimethyl-n-butyl ammonium [$Me_3N^nBu$], 1-ethyl-3-methylimidazolium [EMIM], 1-methyl-1-propylpiperidinium [PMPip]. Anion: bis(trifluoromethanesulfonyl)imide [TFSI] …….…….. 123

**Figure 47.** UV-Vis spectra of 50 mM Nd in 1 M $HClO_4$ ……..…… 128

**Figure 48.** UV-Vis spectra of the mixed U and Nd in 1 M $HClO_4$ after extraction from the IL samples ……...…… 128

**Figure 49.** UV-Vis spectra of Deposit C obtained from -2.0 V applied for 12 hrs, Nd and U in [EMIM][TFSI], dissolved deposit in 1 M $HClO_4$ …….. 130

**Figure 50.** UV-Vis spectra of Deposit A obtained from -2.0 V applied for 12 hrs, Nd and U in [$Me_3N^nBu$][TFSI], dissolved deposit in 1 M $HClO_4$ ……. 130

**Figure 51.** UV-Vis spectra of Deposit B obtained from -2.0 V applied for 12 hrs to Nd and U in [PMPip][TFSI], dissolved deposit in 1 M $HClO_4$ ……...…….. 131

List of Equations

**Equation 1.** Dissolution of $Ln(CO_3)_3 \cdot xH_2O$ using HTFSI……... 7

**Equation 2**. Dissolution of $AnO_2(CO_3)$ using HTFSI……... 7

**Equation 3.** Platinum oxide formation potential ……... 8

**Equation 4.** Gold oxide formation potential ……. 8

**Equation 5.** Oxygen formation potential …….. 8

**Equation 6.** Hydrogen formation potential ……... 8

**Equation 7.** Dissolution of $Ce_2(CO_3)_3 \cdot xH_2O$ using HTFSI and formation of neutral $Ce(TFSI)_3$ complex in IL……..…….. 21

**Equation 8.** Dissociation of carbonic acid …….. 21

**Equation 9.** Dissolution of $Ce_2(CO_3)_3 \cdot xH_2O$ using HTFSI and formation of anionic $Ce(TFSI)_5^{2-}$ complex in IL ……... 21

**Equation 10.** Bragg's Law …….……. 26

**Equation 11.** Absorbance as a function of transmittance ……... 29

**Equation 12.** Beer-Lambert law …….. 29

**Equation 13.** first Karl Fischer reagent reaction …… 32

**Equation 14.** second Karl Fischer reagent reaction …… 32

**Equation 15.** Peak Current …….. 36

**Equation 16.** Nernst equation ……. 36

**Equation 17.** Formation of AuO, first reaction in formation of $Au_2O_3$ …….. 50

**Equation 18.** Formation of $Au_2O_3$, second reaction in formation of $Au_2O_3$ ……... 50

**Equation 19.** Reduction potential of $Ce^{4+}/Ce^{3+}$ ……..…… 62

**Equation 20.** Reduction potential of $Ce^{3+}/Ce^{0}$ …… 62

**Equation 21.** Dissolution of $UO_2CO_3$ using HTFSI ……..…….…… 88

**Equation 22.** Formation of $CeO^{\cdot 3+}$ from $Ce^{3+}$ and $O_3$ ……... 102

**Equation 23.** Formation of $Ce^{4+}$ from $CeO^{\cdot 3+}$ and $H^{+}$ ……... 102

**Equation 24.** Formation of $Ce^{4+}$ from $Ce^{3+}$ and $^{\cdot}OH$ ……..…….. 102

**Equation 25.** Formation of $H_2O$ from $OH^{-}$ and $H^{+}$ ……....…….. 102

**Equation 26.** Formation of $U_3O_9^{\cdot}$ from $U_3O_8$ and $O_3$ ……...… 102

**Equation 27.** Formation of $UO_2^{2+}$ and $H_2O$ from $U_3O_9^{\cdot}$ and $H^{+}$ ……...…… 102

**Equation 28.** Formation of $U_3O_9^{\cdot}$ and $N_2$ from $U_3O_8$ with NO ……..… 102

**Equation 29.** Formation of $UO_2^{2+}$ and $H_2O$ from $U_3O_9^{\cdot}$ And $H^{+}$ ……..…. 102

**Equation 30.** Separation Factor …… 121

# Chapter 1. Introduction

## 1.1 Motivation

The research presented in this dissertation was conducted to address the application of ionic liquids (ILs) in the electrochemical separations and recovery of materials relevant to the nuclear fuel cycle. The first part of the research effort focused on developing an alternative method for the direct dissolution of lanthanide and actinide species into an IL, n-trimethyl-n-butylammonium bis(trifluoromethanesulfonyl)imide $[Me_3N^nBu][TFSI]$. In the second part, characterization of the dissolved species in IL followed by the primary goal of recovering soluble lanthanide and actinide species using electrochemical methods. The fundamental investigations were conducted using both lanthanide (Ce) and actinide (U) species dissolved in the IL. Finally, the electrochemical separation of individual species from a binary Ln/An mixture (Nd/U) was examined. The ultimate goal of this research is to obtain and disseminate fundamental knowledge of lanthanide/actinide dissolution, and separation and recovery from $[Me_3N^nBu][TFSI]$, or similar ILs, for the development of electrochemical separations and recycling applications.

## 1.2 Overview of the Nuclear Fuel Cycle

Domestically, the U.S. Nuclear Regulatory Commission (NRC) is charged with regulating "all commercial reactors in the United States, including nuclear power plants that produce electricity, and university research reactors. The agency regulates the possession, transportation, storage and disposal of spent fuel produced by the nuclear reactors". As of October 2015 there are 99 commercial nuclear generating power reactors licensed by the United

States Nuclear Regulatory Commission (NRC) to operate, producing approximately 20% of the nation's total electric energy consumption. In addition, there are 31 licensed research and test reactors (2012)[1].

Natural uranium consists primarily of 99.274 % $^{238}U$ and approximately 0.720 % $^{235}U$. Most nuclear reactors however require enrichment of the fissile $^{235}U$ for effective sustained fission and energy production. The commercial nuclear reactors in the United States utilize a uranium dioxide ($UO_2$) fuel pellet which has been enriched in $^{235}U$ to between 3.5 and 5%.[2] After the fuel rods are removed from the reactor, they are typically transported to cooling pools where they stay for up to 10 years while the short-lived fission products decay and reduce the radioactivity of the used fuel before disposal or reprocessing, The majority of spent nuclear fuel still consists of uranium, which has already been through the processing of enrichment. The remainder is a mixture of fission products and transuranic activation products such as plutonium (**Table 1**).[3]

**Table 1.** List of the composition of used nuclear fuel (not including Xe which is a fission product gas) as determined by ORIGIN2 calculations after 30 MWd/kgM, 10 years cooling, and of material with an initial enrichment of 2.94% $^{235}U$.

| Element | Percentage by mass |
|---|---|
| U | 95.99 |
| Pu | 0.83 |
| Nd | 0.36 |
| Zr | 0.33 |
| Mo | 0.30 |
| Cs | 0.23 |
| Ce | 0.22 |
| Ru | 0.20 |
| Ba | 0.16 |
| Pd | 0.12 |

The NRC estimated that 45,000 tons of spent nuclear fuel was being stored in the United States.[1] Generally, there are two major processes for handling spent fuel and the highly radioactive fission products. One consists of storing the spent fuel in a pool to cool the material for a number of years while the short-lived fission products decay away. The spent fuel is then moved to specially designed dry cask storage. The goal is to transfer the waste to a long-term geologic repository. The spent nuclear fuel is shielded and packaged within the casks to prevent leaking and to provide optimal storage conditions. Currently, the United States follows this procedure with regards to spent nuclear fuel and has been termed an "once through" fuel cycle. However, to date there are no licensed long-term high level waste (HLW) repositories to store the spent fuel or final HLW products from commercial nuclear reactors.[1,4]

Reprocessing or other advanced recycling pathways have been suggested as an alternative to the "once through" fuel as it provides a considerable improvement in terms of nuclear waste management with a reduction in long term radiation hazard and a reduction in uranium disposal needs by partitioning uranium and plutonium from the raffinate. The concept of reprocessing used nuclear fuel was first developed in the United States in the 1950s and has since been adopted, in various forms, by other countries such as France, England, and Japan. The majority of used nuclear fuel can be reprocessed, reclaimed, mixed or enriched as required and used to produce fuel pellets for various reactor designs. In addition, other desirable trans-uranic and fission products may be obtained through a series of separations.

Plutonium-Uranium Extraction (PUREX) is a standard reprocessing method used within the industry.[4] A flow-sheet of PUREX (**Figure 1**) provides an overview of this process. The fuel rods are disassembled and the used fuel pellets are dissolved in nitric acid. The uranium and the resulting fission and activation products are initially in the aqueous phase and are contacted with

an organic phase containing the extractant tributyl phosphate (TBP) diluted in n-dodecane or hydrogenated polypropylene tetramer (HPT). The hexavalent uranium and tetravalent plutonium are extracted into the organic phase. In the next step, a reductant such as $U^{4+}$ is added to the system and the plutonium reverts to the aqueous phase as $Pu^{3+}$. The uranium can then be stripped from the organic phase by contacting with dilute nitric acid. While PUREX is effective at separating uranium from plutonium and the fission products, as a chemical process it also produces additional liquid radioactive waste.[4] Therefore, continued research efforts to find more efficient methods to reduce the number of steps or the amount of waste from the current reprocessing scheme remains a current world-wide research focus.

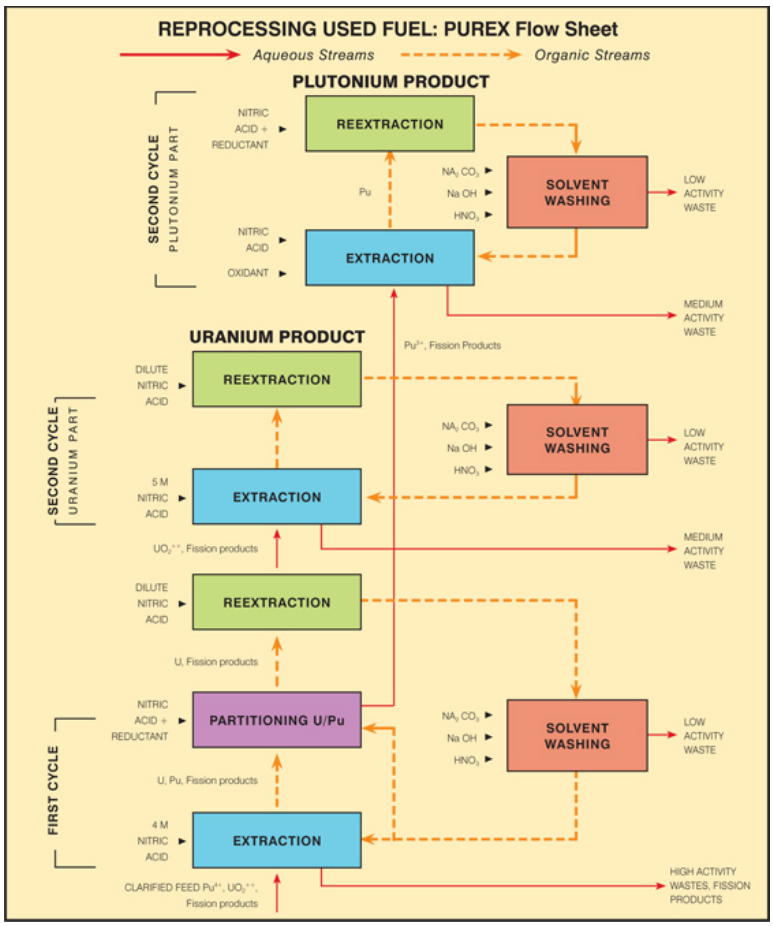


**Figure 1.** PUREX process flow sheet[5]

Recently there has been interest in the use of ILs for separations in recycling schemes.[6,7,8,9] Initial studies reveal ILs possess unique properties including relatively robust stability and inherent conductivity for electrochemical applications. However, there is a lack of fundamental research of actinides and lanthanides in IL solvents to assess the possible applications to the nuclear fuel cycle.

## 1.3 Overview of Ionic Liquids

The origins of ILs have been attributed to Paul Walden who first synthesized and studied the electrochemical application of ethylammonium nitrate in 1914.[10] The first generation ILs were based on chloroaluminate anions.[11] However, the properties and applications of chloroaluminates were not studied in detail until Osteryoung[12] rediscovered the potentials of chloroaluminate melts in the late 1970s. It was realized that haloaluminate based ILs had a limited scope as they were moisture sensitive and required a non–ambient conditions for their synthesis and applications. Subsequent advances led to the discovery of moisture-stable ILs in 1992 by Wilkes et al.[13] The second generation ILs have non–hydrolyzing or stable anions, such as $PF_6^-$, $BF_4^-$, $NO_3^-$, $CH_3COO^-$. The discovery of these moisture-stable ILs expanded possible applications into many branches of research including organic synthesis, catalysis, electrochemistry, and separation science.[13]

The second generation ILs are chemically stable, purely ionic solutions and are molten at temperatures lower than 373 K. Generally, the ion pair is comprised of a bulky, asymmetrical organic cation and an organic or inorganic anion. Properties of each IL are unique to a combination of a particular cation and anion. The large number of possible combinations has made these solvents popular as “designer solvents” because their properties can be tuned using

different cation/anion pairs. Some notable properties of ILs include low vapor pressure, an ability to dissolve organic and inorganic compounds, inherent conductivity, and a wide electrochemical potential window.[14]

### 1.3.1 Solubility of f-elements in Ionic Liquids

Any potential applications of ILs will be dependent upon the ultimate solubility of the f-element species in this solvent. To date the electrochemical study of lanthanides in IL is complicated by the inherent low solubility of the species in IL. Methods have been utilized to increase solubility including the direct dissolution of lanthanide species using preformed complexes prepared and isolated from aqueous solutions. For example, complexes prepared with bis(trifluoromethanesulfonyl)imide (TFSI)[15] of the general form, $Ln(TFSI)_3(H_2O)_3$ (Ln = La(III), Sm(III), and Eu(III))[16], have been successfully dissolved directly into the IL n-trimethyl-n-butylammonium bis(trifluoromethanesulfonyl)imide, $[Me_3N^nBu][TFSI]$. In addition, "task specific" ILs that contain acid functionalized cations have been used to dissolve a variety of lanthanide and some actinide metal oxides into ILs.[17,18] Using this method many trivalent lanthanides (e.g. $Sm_2O_3$, $Eu_2O_3$, and $Nd_2O_3$) and $UO_3$ were dissolved into the IL without addition of secondary acid species.[19]

The previous methods suggest that the use of acid functional groups may be beneficial in the dissolution and ultimate solubility of lanthanide and actinide species in ILs. However, the direct dissolution of f-element species in the ILs using secondary acid species common to the IL has not been extensively studied. For example, HTFSI has been utilized to produce protic ILs with a variety of different cations.[20] The evolution of hydrogen in IL solutions is demonstrated suggesting that the protons within the IL are at least partially dissociated from TFSI. The data suggests the direct dissolution of actinide/lanthanide carbonates may be possible using HTFSI to

increase the solubility in the IL. In this process the water and $CO_2$ content can be reduced to pre-dissolution conditions with degassing of the IL based on the following general reactions:

$$Ln_2(CO_3)_3 + 6\ HTFSI \rightleftharpoons Ln(TFSI)_3 + 3\ H_2CO_3 \longrightarrow 3\ H_2O\uparrow + 3\ CO_2\uparrow \quad \textbf{(Eq. 1)}$$

$$AnO_2(CO_3) + 2\ HTFSI \rightleftharpoons AnO_2(TFSI)_2 + H_2CO_3 \longrightarrow H_2O\uparrow + CO_2\uparrow \quad \textbf{(Eq. 2)}$$

Previous electrochemical studies provide the basis for a more detailed analysis of the interfacial processes associated with soluble lanthanide species in IL. However, a more comprehensive, systematic evaluation of the dissolution of lanthanide and actinide species in IL is required. Although there is evidence that task specific ILs can increase solubility of lanthanide oxides using acid functional groups,[17,18,19] there has been no clear evaluation of the addition of HTFSI on the solubility of f-elements in IL containing the common ion TFSI.[21,22]

### 1.3.2 Difficulties of f-element chemistry in aqueous systems

The measurement of the oxidation/reduction processes of f-elements at common electrodes (Au, Pt, or glassy carbon (GC)) is complicated by side reactions that occur at potentials that preclude the analysis of electropositive lanthanide and actinide species in aqueous solution. For example, the potential window at positive potentials is constrained by water oxidation or metal oxide formation. In addition, hydrogen evolution at negative potentials at both Pt and Au metal surfaces influences the negative potential limit that can be achieved for the reduction of electropositive f-element species. The ultimate electrochemical window that can be utilized in aqueous solution is 1.3 V to 2.5 V, depending upon electrode composition and potentials for the side reactions below:[23-25]

$PtO_2 + 4\ H^+ + 4e^- \rightleftharpoons Pt\ (s) + 2\ H_2O$ E° = 0.83 V vs. Ag/AgCl (**Eq. 3**)

$Au_2O_3 + 6\ H^+ + 6e^- \rightleftharpoons 2\ Au(s) + 3\ H_2O$ E° = 0.90 V vs. Ag/AgCl (**Eq. 4**)

$O_2 + 4\ H^+ + 4e^- \rightleftharpoons 2\ H_2O$ E° = 1.03 V vs. Ag/AgCl (**Eq. 5**)

$2\ H^+ + 2e^- \rightleftharpoons H_2$ E° = -0.20 V vs. Ag/AgCl (**Eq. 6**)

For comparison, **Table 2** provides the potentials, based upon thermodynamic values, for the reduction of some lanthanides and actinides in acidic aqueous solution. [26]

**Table 2.** Reduction potentials of selected lanthanides and actinides in acidic aqueous solution.

| Reaction | $E^o$ (V) vs. Ag/AgCl |
|---|---|
| $Ce^{3+} + 3e^- \rightleftharpoons Ce^0$ | -2.537 |
| $Sm^{3+} + 3e^- \rightleftharpoons Sm^0$ | -2.497 |
| $Eu^{3+} + 3e^- \rightleftharpoons Eu^0$ | -2.187 |
| $UO_2^{2+} + 4H^+ + 2\,e^- \rightleftharpoons U^{4+} + 2H_2O$ | +0.073 |
| $U^{4+} + 4\,e^- \rightleftharpoons U^0$ | -1.577 |
| $PuO_2^{2+} + 4H^+ + 2\,e^- \rightleftharpoons Pu^{4+} + 2H_2O$ | +0.833 |
| $Pu^{4+} + 4\,e^- \rightleftharpoons Pu^0$ | -1.447 |

It becomes apparent that in most cases the reduction potentials of the lanthanide and actinide species are significantly more negative than the potential associated with the hydrogen evolution side reaction is ~ -0.2 V for Pt and Au electrodes.[17,20,22] Carbon based electrodes can be used to extend the negative potential to ~ -0.6 V before hydrogen evolution is observed.[21] However, the ability to expand the potential window and systematically examine the thermodynamic electrochemical properties of f-elements is prohibitive in aqueous solutions due to the negative potential limit associated with the hydrogen evolution reaction.

More fundamental thermodynamic studies of f-element oxidation/reduction processes have been conducted in aqueous solutions using Hg electrodes. The controlled oxidation and reduction of f-elements at Hg electrodes can be accomplished in aqueous solution because stable amalgams with actinide and lanthanide ions and metals are formed. The Hg electrode provides more thermodynamically favorable reduction, while also minimizing competing side reactions such as hydrogen evolution.[27] The thermodynamic potentials have been established previously for the amalgamation of both lanthanide and actinides species from aqueous solutions at Hg electrodes.[28-31] However, the use of Hg metal electrodes in electrochemical processes is not ideal for recovery of lanthanide and actinide species and toxicity issues associated with the electrode remain a significant drawback to its use. The disadvantages associated with the previous electrochemical methods can be minimized using non-aqueous IL solutions.

### 1.3.3 Advantages of Ionic Liquids

The choice of cation/anion pair influences not only the physical properties of the resulting IL such as viscosity, density, and melting point but also the electrochemical window. Common cations used to prepare IL solutions include imidazolium, pyridinium, ammonium, phosphonium, and sulfonium ions paired with a variety of anions including halides, $BF_4^-$, $CF_3CF_2CF_2CO_2^-$, $N(CN)_2^-$, and $N(SO_2CF_3)_2^-$ [TFSI] to name a few.[32] Electrochemical windows for IL solutions are based on the reduction of the cation and oxidation of the anion at the electrode surface. The potentials for anion oxidation and cation reduction in IL solutions typically occur at more positive and negative potentials relative to water oxidation and hydrogen evolution, providing an expanded potential window. For reference, the structure for the IL, $[Me_3N^nBu][TFSI]$ is given in **Figure 2**. The electrochemical windows associated with common working electrodes in the IL, n-trimethyl-n-butylammonium bis(trifluoromethanesulfonyl)imide

([$Me_3N^nBu$][TFSI], **Figure 3**) provides absolute potential windows of approximately 4.5 V for Pt, 5.0 V for Au, and 6.0 V for GC, respectively.[33-36]

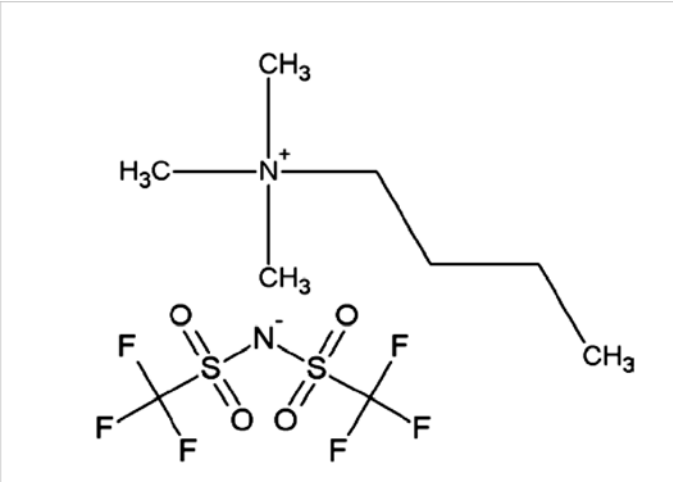


**Figure 2.** The structure of [$Me_3N^nBu$] cation and [TFSI] anion

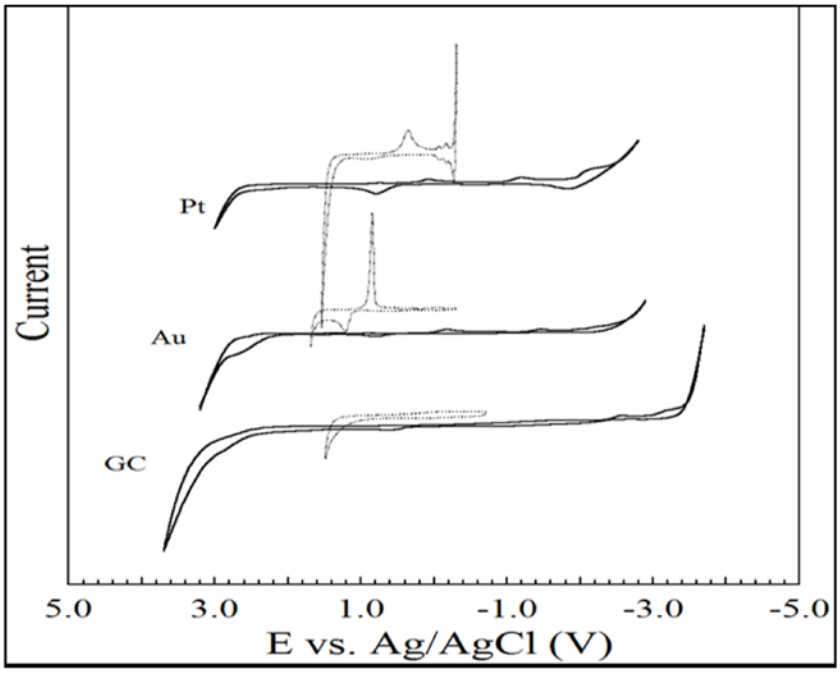


**Figure 3.** Comparison of the electrochemical window at Pt, Au, and GC electrodes in 0.1 M $H_2O_4$ (dashed line) and the [$Me_3N^nBu$][TFSI] (solid line)

Moreover, the potential windows provided by this IL encompass the thermodynamic potentials associated with the reduction of lanthanide and actinide species to metal.[24,26] Due to the relatively large potential window afforded by the [$Me_3N^nBu$][TFSI] for common working electrodes which encompasses the reduction potentials of lanthanides and actinides, it was chosen as the IL used in the course of these studies.

The electrochemical properties of trivalent lanthanides including La,[12] Tm,[37] Eu,[12,33,34] Sm,[12,38,39] Yb,[34,35] and Dy[40] in various IL solutions have been reported. The studies have examined the interfacial oxidation/reduction of the species in IL solution without surface deposition,[12,33,34] and the stepwise reduction and deposition of the metal species.[12,35,36] These studies provide the proof of principal that IL solutions can be utilized to examine both the interfacial oxidation/reduction and deposition of lanthanides from IL solutions. The oxidation/reduction of the ($M^{3+/}M^{2+}$) lanthanide couple have been resolved for Sm,[12] La,[12] Eu,[12,33] and Tm[33] in ILs. The electrochemical deposition of Eu and Sm has also been demonstrated from solutions containing $Sm(TFSI)_3$, $Eu(TFSI)_3$ using the IL solutions containing quaternary ammonium and phosphine cations with the bis(trifluoromethanesulfonyl)imide (TFSI) anion.[12,36] In addition, the electrochemical deposition of Dy from dimethylpyrrolidinium trifluoromethanesulfonate (DMPT) has been documented.[36] These studies demonstrate that the solution oxidation/reduction processes are encompassed within the potential window of many ILs. In many cases, sufficiently negative potentials can be achieved to also reduce the species to metal at electrode surfaces.

## 1.4 Applications of Ionic Liquids in the Nuclear Fuel Cycle

A review by Venkatesan et al. evaluates the possibilities of using ILs in nuclear fuel cycle applications.[6] The areas related to aqueous and non-aqueous reprocessing and nuclear waste management. Solvent extraction from aqueous solutions[7,41] has been utilized to introduce f-elements and species into ILs. Extraction is typically achieved by first dissolving the f-elements in nitric acid solutions (0.01 to 8 M were tested) followed by two-phase extraction of the soluble species into the IL using complexing agents such as TBP.[8,9] In regards to applications of ILs to aqueous reprocessing, Dietz[42] and Huddleston[43] investigated the use of IL to replace the traditional diluent (n-dodecane) in the PUREX process. In a similar study, Giridhar et al.[44,45] reported the solvent extraction of uranium (VI) by a solution of 1.1 M TBP in 1-butyl-3-methylimidazolium hexafluorophosphate ($bmimPF_6$) or $bmimNTf_2$ ($NTf_2$ = bis(trifluoromethanesulfonyl)imide) for comparison with the results of the traditional PUREX solvent 1.1 M tributylphosphate (TBP)/n-dodecane. These studies revealed favorable extraction when ILs are used in conjunction with extractants. More recently, species such as Pu(IV), Th(IV), and trivalent lanthanides have been extracted into IL without the need of additional complexing agent.[46,47] The results suggest that extraction may be an effective way of pre-concentrating f-elements in ILs.

In addition to the solvent extraction using 1.1 M TBP/IL, Giridhar et al. also investigated the electrochemical stability of the solvent at glassy carbon working electrode and voltammetric studies on the uranyl nitrate extracted 1.1 M TBP/IL phase.[8] The results demonstrated the possibility of recovering uranium (VI) as uranium oxide deposit at the working electrode. These findings suggested the feasibility of using IL as both the diluent for solvent extraction followed by recovery of oxides or metals by electrodeposition. This process was termed Extraction-Electrodeposition (Ex-El Process). This proposed Ex-El process avoids the traditional stripping

step in aqueous reprocessing which produces large amounts of aqueous waste. It also could avoid the chemical transformation steps to obtain desirables (e.g. U or Pu) as metals or oxides.

Previous work has established the use of molten salt systems (450 – 800 °C) to electrochemically recover certain desirables such as uranium and plutonium from used nuclear fuel.[48,49] The molten salt system however requires a specialized corrosion resistant cell, operation at the elevated temperatures, and produces caustic side reactions.[50] It was envisioned that if the process could be performed using ILs, which are liquid at or near room temperature, the disadvantages of the molten salt system could be removed or mitigated. Indeed, studies by Bhatt et al. on the electrochemistry of Sm(III), La(III), Eu(III) and Th(IV) in $[Me_3N^nBu][TFSI]$ reported redox potentials and reduction of Sm, La, and Eu to the metallic state.[11,12] The Th(IV) was reported to reduce to Th(0) but subsequently was converted to $ThO_2$ by moisture in the IL. The potential at which the thorium was found to undergo the reduction to Th(0) in the IL $[Me_3N^nBu][TFSI]$ was also more thermodynamically favorable when compared to similar deposition from LiCl-KCl and other non-aqueous solvents.[12] Studies such as these demonstrate that $[Me_3N^nBu][TFSI]$ encompasses the potentials for deposition of actinides and lanthanides to the metal if the presence of residual water in the IL can be minimized.

Despite the unique physical properties of ILs and the envisioned nuclear fuel cycle applications, Venkatesan et al. emphasize further research is needed in a number of areas to evaluate the potential for robust nuclear technology.[6] One consideration is that certain ILs exhibit some extent of aqueous solubility compared to the traditional PUREX diluent (n-dodecane) that may influence the physical properties including viscosity, density, and ionic solubility. These are important parameters related to efficiency during solvent extraction, and the occurrence of phase inversion and longer times for disengagement when using ILs have been reported. Additionally,

there is a need for further studies of parameters associated with electrochemistry for non-aqueous reprocessing such as viscosity, conductivity, electrochemical windows, kinetics of electron transfer, and methods to dissolve used nuclear fuel into IL. The authors, however, were of the opinion that all of these could be addressed through continued research and selection of the appropriate cation/anion pair for the IL most appropriate for the particular application through parameter optimization.

## 1.5 Organization of Dissertation

The research performed in support of this dissertation involved development and investigation of a method for direct dissolution of f-element (Ce and U) carbonate and/or oxide compounds into an IL (n-trimethyl-n-butylammonium bis(trifluoromethanesulfonyl)imide; $[Me_3N^nBu][TFSI]$) followed by subsequent investigation using electrochemical methods for the recovery and possible separation of uranium.

Chapter 2 provides an introduction to the materials, methods, and instrumentation concepts used during the course of the work. Each subsequent chapter, however, contains a different scope with sometimes different synthesis strategies or applied parameters to the discussed methods and instrumentation and therefore will contain a pertinent experimental section as well as the results and discussion followed by conclusions.

Chapter 3 discusses the selection of the particular IL chosen and compares it to the acidic aqueous system as well as studies performed on the non-aqueous $Ag/Ag^+$ IL reference electrode used within the electrochemical work. While $[Me_3N^nBu][TFSI]$ is considered hydrophobic a certain amount of water can exist within the IL up to a saturation point. An experiment was designed to investigate the water content up to saturation and electrochemical affects across a

spectrum of water content within the IL. An electrochemical method is applied for water determination and monitoring by utilizing the formation of gold oxide at an Au disc electrode. A correlation is determined between the resulting formation and integration of the gold oxide reduction peak to water content as an in-situ and non-destructive method for water determination within the IL. Methods of drying the wet IL by molecular sieves or purging with dried inert gas are also demonstrated.

Chapter 4 presents the direct dissolution of $Ce_2(CO_3)_3 \cdot xH_2O$ into the IL. The subsequent Ce in IL is characterized spectroscopically with UV-Vis and IR spectroscopy. Electrochemical methods including cyclic voltammetry and constant potential mediated deposition are presented. The obtained deposit is characterized by scanning electron microscopy (SEM) and energy dispersive X-ray spectroscopy (EDS).

Chapter 5 presents the direct dissolution of $UO_2CO_3$ and $U_3O_8$ into the IL. The subsequent $UO_2^{2+}$ in IL is characterized spectroscopically with UV-Vis and IR spectroscopy. Electrochemical methods including cyclic voltammetry and constant potential mediated deposition are presented. The obtained deposit is characterized by SEM and EDS.

Chapter 6 presents the separation of uranium achieved through electrodeposition from a mixed Nd/U in IL sample. Three different ILs all sharing the TFSI anion were compared across varying deposition potentials. The samples were studied by UV-Vis spectroscopy as well as being back-extracted into 1 M $HClO_4$ for UV-Vis spectroscopy and ICP-AES analysis of Nd and U content. A comparison of the Nd and U content of the sample before and after electrodeposition was used to determine approximate separation factors from the method and potentials applied. Some electrodeposited samples were cleaned and annealed for SEM/EDS analysis of the deposit as well

Finally, Chapter 7 provides an overall summary of the work with insights on areas of further work.

# Chapter 2. Experimental Methods

This chapter serves to provide background on the instruments and methods that are used within the research. The synthesis of the uranyl carbonate and uranium oxide materials is provided, as well as the basis for the concept of dissolution of these materials into the IL. In addition, each instrument or analytical method is described with an introduction to the basis of how it works as well as the particular model used within this work. Each subsequent chapter will provide more information and particular parameters relevant to the research covered within.

## 2.1 Materials Synthesis

### 2.1.1 $UO_2CO_3$

Most of the uranium sources available for use are either depleted uranium or natural uranium. These depleted uranium materials are radioactive with the activity dominated by $^{238}U$ (half-life 4.468E9 years). Therefore, evaluation of activity requires long count times, which is relevant for radioanalytical techniques such as liquid scintillation counting (LSC). Addition of an isotope of uranium with a shorter half-life such as $^{233}U$ (half life 1.592E5 years), is utilized to enhance the specific activity and allow for more rapid radioanalytical counting. The synthesis of the uranyl carbonate was based on literature procedures.[51-53] Uranyl carbonate was produced by adding 4.2 mL of 1.01 M solution containing dissolved uranyl nitrate hexahydrate ($UO_{2(}NO_3)_2{\cdot}6H_2O$) with 7.0 mL of 0.15 mM $^{233}U$ solution adjusted to a pH 4.03. Then ultra-pure water was used to reach a total volume of 50 mL. The pH of this solution was adjusted to 3.85 using $Na_2CO_3$ and $HNO_3$ in order to promote production of the uranyl monocarbonte species formation and precipitation. This solution was subsequently bubbled with $CO_2$ gas for

one week. The resulting precipitate was collected, washed with D.I. water, and freeze dried for 72 hours. The recovered precipitate was verified as being $UO_2CO_3$ by IR[54] and powder XRD analysis[54,55] as featured in **Figure 4** indicating a Rutherfordine match (uranyl monocarbonate). The resulting $UO_2CO_3$ contained about 0.025% $^{233}U$ by mass due to the spike added to the solution before precipitation.

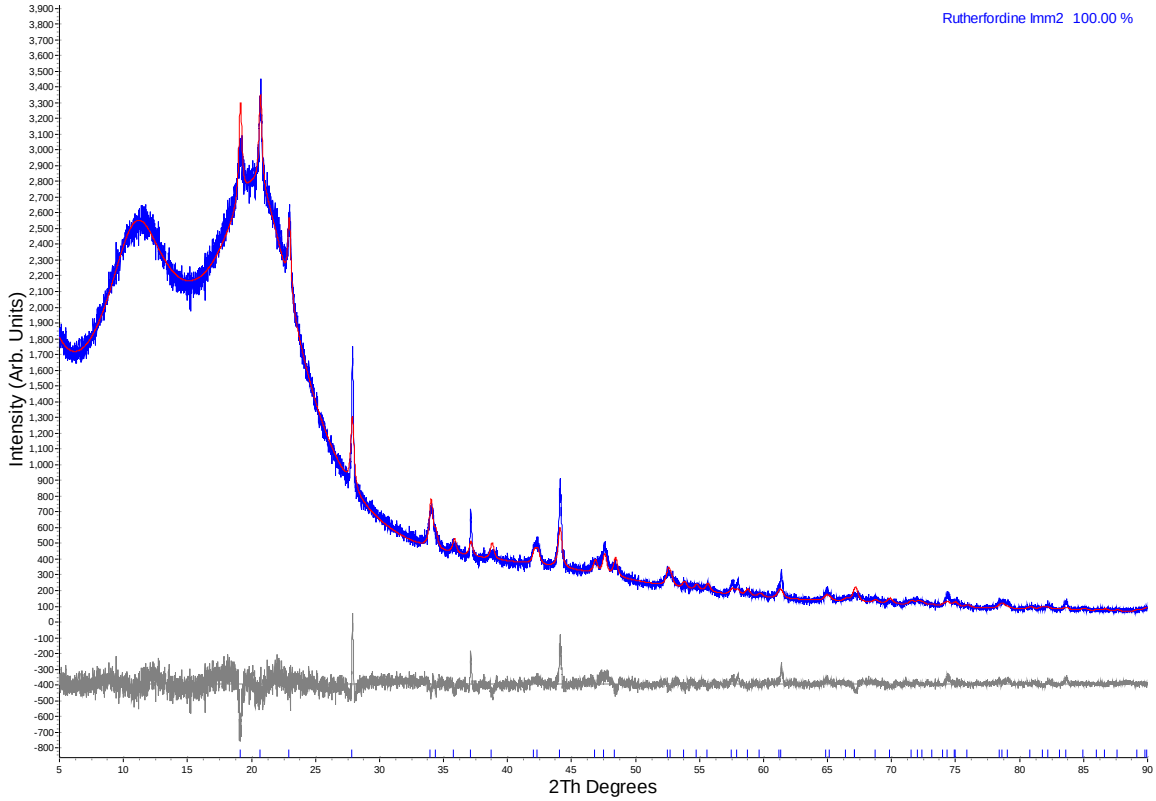


**Figure 4.** Powder XRD comparison of the synthesized $UO_2CO_3$ against a database structure (Rutherfordine)

### 2.1.2 $U_3O_8$

The uranium oxide used was prepared from depleted uranium (uranyl nitrate hexahydrate, $UO_2(NO_3)_2 \cdot 6H_2O$) that has been dissolved in ultra-pure water. A spike of $^{233}U$ in acidic solution is added so that the precipitated product contained the isotope in a small amount (0.024 - 0.03 %)

increasing the overall specific activity of the material for the experiments involving liquid scintillation counting. An ammonium diuranate ($(NH_4)_2U_2O_7$) product was precipitated by addition of concentrated ammonium hydroxide. The precipitate was collected by centrifugation and the base was added again until no further precipitation was observed. The supernatant was removed and the product transferred into a drying dish to dry in an oven for at least 48 hours at 200°C. The uranium product, now orange in color, was then removed from the box furnace and was next transferred to an alumina boat to be placed in a tube furnace (**Figure 5**). A glass wool trap was placed at the end of the tube and the gas was also passed through a water trap. The tube furnace was set up with flowing air and ramped up to 800°C for 3 hours, held at temperature for 6 hours, and then allowed to cool to room temperature.


**Figure 5.** Tube furnace set-up inside fume hood for $U_3O_8$ synthesis

The product was now a dark green to dark grey color and further ground with a mortar and pestle to provide a powder with higher surface area for characterization and dissolution. The

product has been prepared a number of times following this method and consistently confirmed by powder X-ray diffraction (XRD) as matching the diffraction pattern of α phase $U_3O_8$ (**Figure 6**).[56]

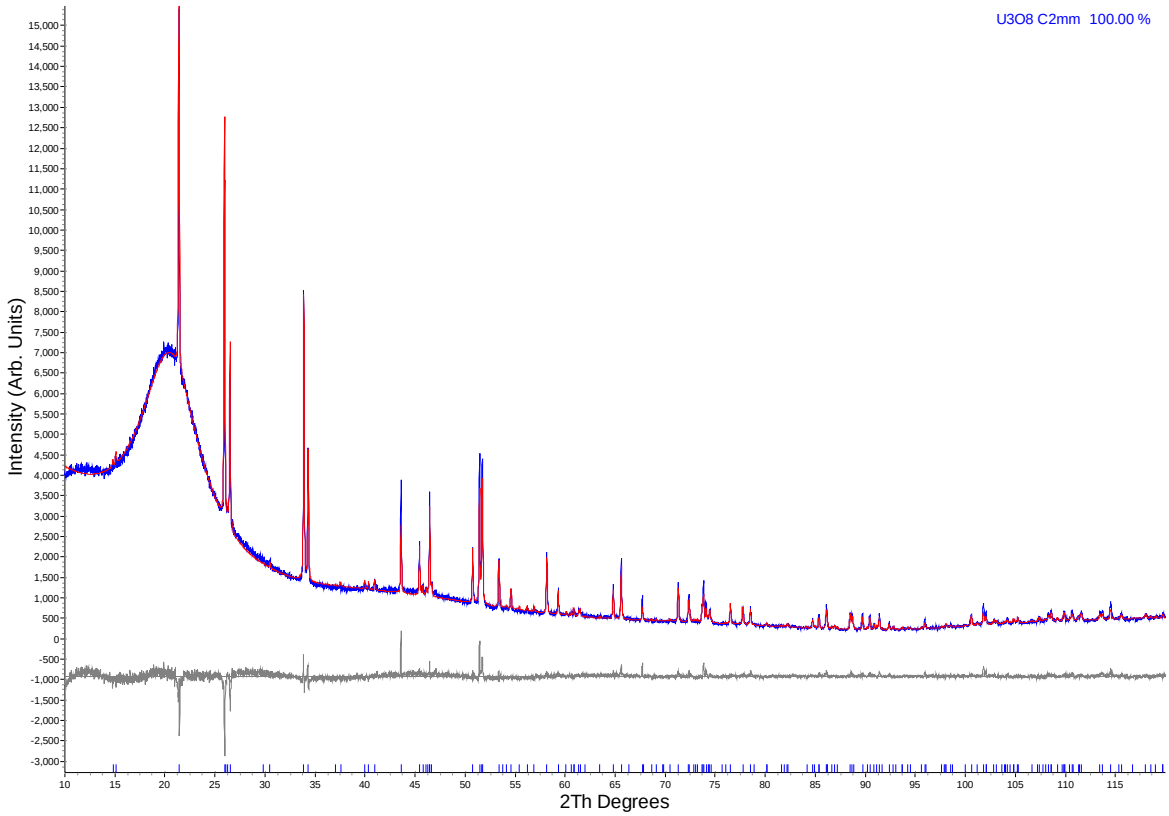


**Figure 6.** Powder X-ray diffraction pattern of $U_3O_8$ (synthesized April 2013) compared to the C2mm structure of $U_3O_8$.

## 2.2 Lanthanide and Actinide Dissolutions

The n-trimethyl-n-butylammonium bis(trifluoromethanesulfonyl)imide, $[Me_3N^nBu][TFSI]$, IL was obtained from Solvionic (≥ 99.5%). The acid common to the anion of the IL bis(trifluoromethanesulfonyl)amide, HTFSI, was used as received from Fluka (≥ 95.0%). Ultra pure water was produced by a Barnstead E-pure system to ≥ 18 Ω. Cerium carbonate,

$Ce_2(CO_3)_3{\cdot}xH_2O$, was also used as received from Alfa Aesar (99.999%). The uranyl carbonate, $UO_2CO_3$, and uranium oxide, $U_3O_8$, were synthesized as previously described and characterized by powder X-ray diffraction.

2.2.1 Direct Dissolution of Cerium Carbonate

Cerium carbonate ($Ce_2(CO_3)_3{\cdot}xH_2O$) was dissolved into $[Me_3N^nBu][TFSI]$ based on the following reactions:

$$Ce_2(CO_3)_3 \cdot xH_2O + 6\ HTFSI \rightarrow 2\ Ce(TFSI)_3 + 3\ H_2CO_3 + xH_2O \qquad (\textbf{Eq. 7})$$

$$3\ H_2CO_3 \rightarrow 3\ CO_2 \uparrow + (3 + x)\ H_2O \uparrow \qquad (\textbf{Eq. 8})$$

The mechanism assumes that Ce forms a neutral $Ce(TFSI)_3$ complex along with carbonic acid which decomposes to carbon dioxide gas and water. In addition, homoleptic lanthanide TFSI complexes with the general form $[Ln(TFSI)_5]^{2-}$ where Ln = Nd and Tb, have also been prepared in IL containing pyridinium cations. Thus the formation of a charged Ce complex is also possible[57] and followed once again with the decomposition of carbonic acid as shown in **Equation 9**:

$$Ce_2(CO_3)_3 \cdot x\ H_2O + 10\ HTFSI \rightarrow 2\ Ce(TFSI)_5^{2-} + 4\ H^+ + 3\ H_2CO_3 + x\ H_2O \qquad (\textbf{Eq. 9})$$

A stock solution of the IL $[Me_3N^nBu][TFSI]$ containing 2.811 g HTFSI (99.8 mM, 100 mL) was prepared. For the direct dissolution, 16 mL of the stock solution was diluted with $[Me_3N^nBu][TFSI]$ to 20 mL total volume (80 mM HTFSI) and the $Ce_2(CO_3)_3{\cdot}xH_2O$ (0.0461 g) was then added to the solution and stirred while bubbling with argon for 48 h to produce an IL

solution containing ~10 mM Ce. The 100 mM Ce solution was prepared using the same method with 0.463 g $Ce_2(CO_3)_3 \cdot xH_2O$ in 20 mL of IL containing 800 mM HTFSI. All solutions containing soluble Ce in IL were purged with desiccated argon to reduce water content before spectroscopic or electrochemical analysis and the final water content for the solutions was confirmed using Karl Fischer titration. The water following dissolution is from the decomposition of carbonic acid combined with the inherent water from the IL and cerium carbonate.

### 2.2.2 Direct Dissolution of Uranyl Carbonate and Uranium Oxide

Following a similar process as that used above for the dissolution of the lanthanide carbonate, a set of 50 mM $UO_2CO_3$ samples containing 0.2475 g $UO_2CO_3$ in 15 mL of deionized water or $[Me_3N^nBu][TFSI]$ with 0.5 M HTFSI were prepared. The uranyl carbonate completely dissolved in the aqueous solution within 10 minutes of mixing. In contrast, the dissolution of $UO_2CO_3$ in the IL did not occur after 24 hours. To facilitate the dissolution, 2 mL of 0.5 M HTFSI in $H_2O$ was added to the sample to enhance the deprotonation of the acid in the IL and increase solubility.[19,58] The sample was sonicated resulting in the complete dissolution of the solid and then centrifuged to assist the separation of two distinct phases (aqueous and IL) containing soluble species. The sample was purged with argon to eliminate the water phase until only the IL was visible.

The uranium oxide was directly dissolved into wet or dry $[Me_3N^nBu][TFSI]$ both with and without HTFSI using oxidizing gas(es) produced by an ozone generator (Ozone Solutions OZV-8) with compressed air feed gas. During experimentation a number of gases were used both with and without active ozone generation: air, oxygen, nitrogen, and nitrous oxide (provided by Praxair and Airgas). The feed gas to the ozone generator was passed through a drierite column

prior to entering the generator to protect the unit and maximize the efficiency of the ozone and oxidizing gas production. The ozone generator production was set to level 5, and the gas flow was ~ 1 L/min to the unit.[59] Off-gas from the dissolution cell was evacuated inside a fume hood after passing through a water bubbler. The dissolution was monitored visually and tracked by taking liquid scintillation samples at various times for radioanalytical counting. More information for the sampling for LSC is presented in that section below.

When "wet" IL was used, a portion of the $[Me_3N^nBu][TFSI]$ was contacted with ultra-pure water and allowed to separate into separate phases. The water-saturated IL is allowed to stay in contact with the water phase until use. The "dry" IL was prepared by adding dried 3Å molecular sieves to the $[Me_3N^nBu][TFSI]$, such as 10 – 12 g of sieves for 40 mL of IL. The IL was contacted with the sieves overnight and stored that way.

## 2.3 Instrumentation and Analytical Methods

### 2.3.1 Ozone generator

The ozone used for dissolutions was obtained operating an Ozone Solutions OZV-8 generator. Ozone is produced by corona discharge. The bonds between some of the oxygen atoms are broken which produces $O^{\cdot}$ radicals. The $O^{\cdot}$ radicals can then recombine with other $O_2$ to produce the ozone ($O_3$) as depicted in **Figure 7**.

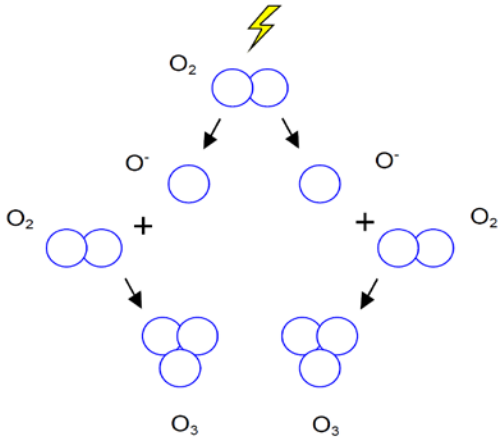


**Figure 7.** Ozone generation by corona discharge[59]

This ozone generator can be used with either dry air or oxygen gas. According to the ozone generation curves provided by the manufacturer, the settings used for dissolution of ~1 L/min flow-rate using dry air feed gas at level 5 (50%) would result in ~ 0.65 g/hr of $O_3$ production (**Figure 8**).[59] The ozone output doubles when operated with oxygen feed gas.

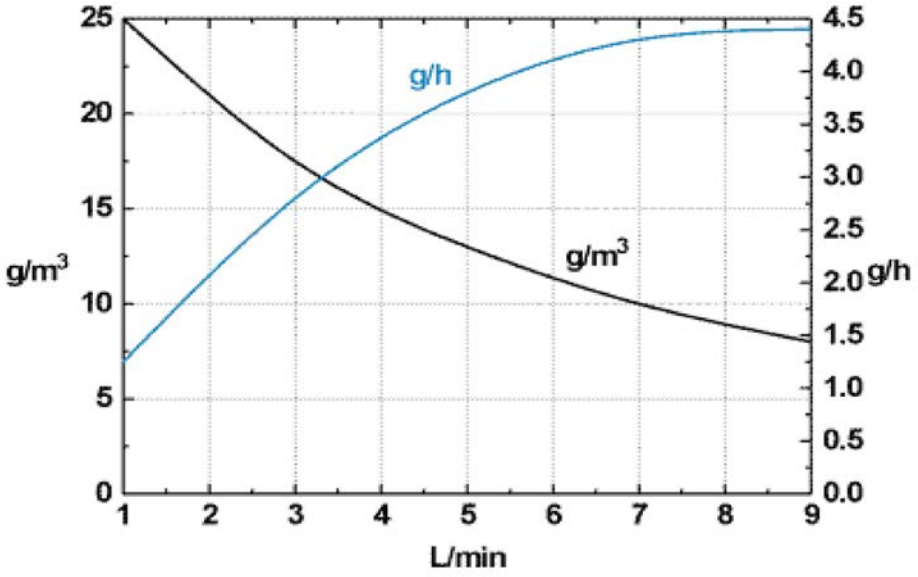


**Figure 8.** Ozone production from Ozone Solutions OZV-8 from dry air[59]

### 2.3.2 Powder X-Ray Diffraction (p-XRD)

Powder X-ray diffraction (p-XRD) is a powerful and common tool for the identification of solid crystalline phases, but does not require the material to be a single crystal. The instrument has been shown to identify crystalline phases present within a sample. However, if a sample is amorphous a suitable diffraction pattern may not be obtained for characterization. XRD works through the detection of X-rays diffracted from a primary X-ray beam incident to a thin layer of powder sample (**Figure 9**). The resulting diffraction pattern is governed by Bragg's law (**Eq. 10**) and is indicative of the compound or relative mixture of compounds in the sample.[60] An experimentally obtained diffraction pattern can then be compared to a standard in the literature or database.

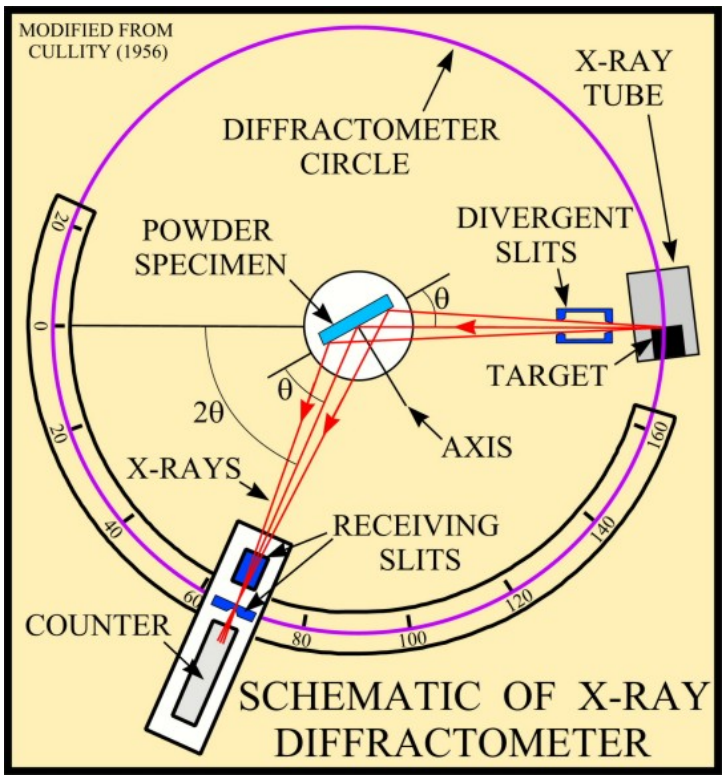


**Figure 9.** Schematic of an X-ray diffractometer

Bragg's Law:

$$2d(\sin\theta) = n\lambda \quad \textbf{(Eq. 10)}$$

Where:

d = lattice interplanar spacing of the crystal

θ = x-ray incidence angle (Bragg angle)

λ = wavelength of the characteristic x-rays

n = integer

Samples for powder XRD analysis should be homogenous and fine in particle size. These conditions are typically achieved by first grinding the material into a powder and then applying it to the sample holder using a compatible liquid solvent. For radioactive materials, the samples are placed in either a sealed holder engineered for confinement or affixed using high X-ray transmittance materials.

The chemical composition and homogeneity of materials were characterized using a Bruker D8 Advance powder X-ray diffractometer configured with Ni-filtered Cu $K_\alpha$ (1.54059 Å) radiation and a silicon strip detector (Lynxeye). The materials were ground to a powder and spread in a thin layer over a low-background single crystal silicon wafer sample holder using ethanol. Patterns were taken using 40 mV and 40 mA from 10 to 120° 2θ. Bruker TOPAS 4.2 was then used to perform the Rietveld structure refinement. The Inorganic Crystal Structure Database (ICSD) was used to input the structure parameters for comparison and identification.

### 2.3.3 Infrared (IR) Spectroscopy

Infrared (IR) spectroscopy is a complimentary technique to ultraviolet-visible spectroscopy (UV-Vis) because it provides information concerning vibrational and rotational

transitions of molecules. When energy in the mid IR region is passed through the sample, the excitation energy is not as high as that of the UV-Vis region and lower energy transitions are induced (**Figure 10**). These vibrational and rotational transitions are influenced by the chemical species providing information regarding functional groups and their interactions within the sample. Discrete vibration and rotation levels can be observed when the frequency of the energy level is equal to the frequency of the IR light source. Infrared absorption will only occur if the energy of the beam matches the excitation energy of the molecule and if there is a change in the electric dipole moment of the molecule. Several different types of bending and stretching motions can be observed including: stretching, scissoring, wagging, twisting, and rocking. As a result, each sample will have an individual spectrum resulting from interactions of specific functional groups contained in the molecule.[60]

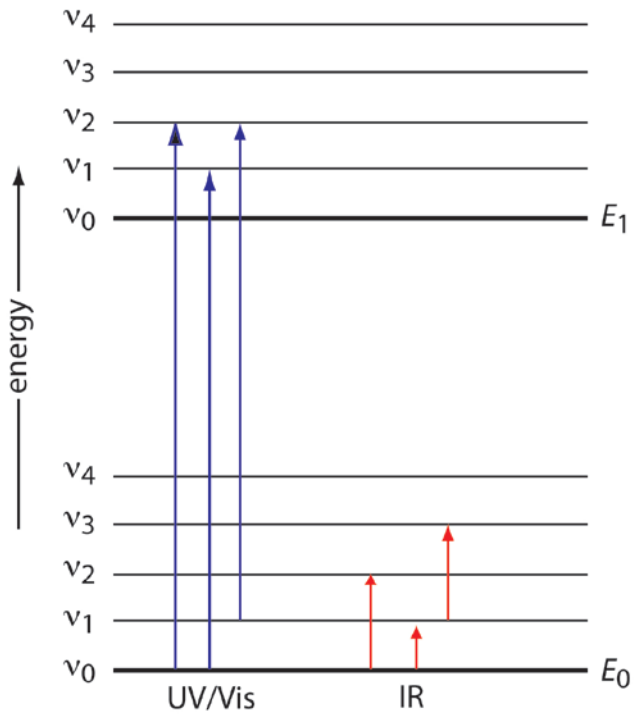


**Figure 10.** Diagram comparing excitation energy of a molecule by UV-Vis or IR light sources for spectroscopy

Commonly, Fourier transform infrared (FT-IR) instruments are utilized. In this method, the IR light passes through the sample and is channeled through an interferometer. This method enables the total beam intensity to be measured for many wavelengths which are simultaneously passed though the detector. A background spectrum must also be collected to provide a reference ($I_o$) to compare against the sample (I). After repeating this cycle many times, the computer analyzes this data using complex mathematical operations that process the signal using time and frequency as the domain.

Characterization of solid materials and IL solution samples was performed using a Varian 3100 FT-IR Excalibur series with a Smiths detection DurasamplIR was used with a diamond attenuated total reflectance (ATR) attachment along with Varian Resolutions Pro, version 5.04.009 software.

### 2.3.4 Ultraviolet -Visible Spectroscopy (UV-Vis)

Ultraviolet-visible (UV-Vis) spectroscopy uses a light source which interacts with a sample through properties of transmittance and absorption. A molecule absorbs the light and in turn excites electrons to various discrete higher energy levels resulting in a characteristic spectrum. The spectrum provides valuable information about speciation through the band structure including oxidation state. Changes in oxidation states of species have noticeable effects of the absorption spectra.

A UV-Vis spectrophotometer (**Figure 11**) measures the intensity of light passing through a sample, I, and compares it to the intensity of light before it passes through the sample, $I_o$. The ratio $I/I_o$ is called the transmittance and is usually expressed as a percentage (%T). The instrument provides the transmittance value which can be expressed as absorbance given the stated relationship in **Equation 11**.[60]

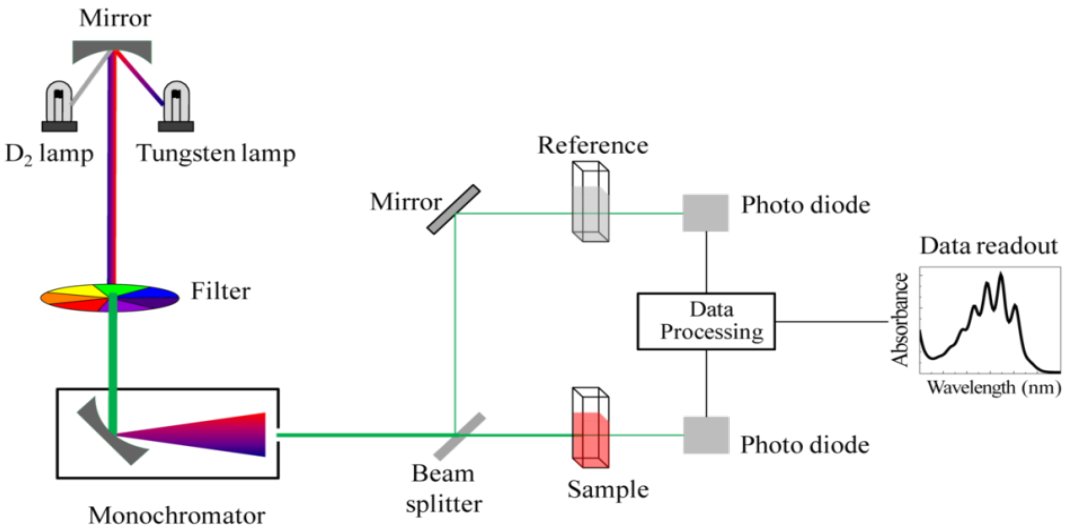


**Figure 11.** Schematic of a UV-Vis spectrophotometer with a dual beam system.

$$A = -\log(T) \text{ or } A = -\log\left(\frac{\%T}{100}\right) \qquad \textbf{(Eq. 11)}$$

A linear region exists which relates the concentration of the species to the amount of energy absorbed which is defined by the Beer-Lambert Law (**A=** $-\log(T) = \varepsilon bc$ (Eq. 12). The specific linear range will vary for each species in solution.

$$A = -\log(T) = \varepsilon bc \qquad \textbf{(Eq. 12)}$$

Where:

A = absorbance

T = transmittance

ε = molar absorptivity, $mol^{-1}$ L $cm^{-1}$

b = path length, cm

c = concentration, mol/L

Using the relationship described the absorbance can then be determined. The path length is known based on the cuvette that was utilized in the experiment. The two potential unknowns remaining are the molar absorptivity and the concentration. When one of these factors is known, then the remaining unknown can be determined from the spectrum. The molar absorptivity is a value which is species and matrix dependent.

UV-Vis spectra were collected using a dual beam Cary 6000 UV-Vis-Near IR spectrophotometer using quartz cuvettes under ambient conditions. Absorbance spectra were collected for representative sample solutions not containing the analyte and this absorbance is presented in figures for a background reference or subtracted from the analyte sample absorbance.

### 2.3.5 Liquid Scintillation Counting (LSC)

Liquid scintillation counting is a commonly used radioanalytical technique for determining the activity in a sample. This technique can be used to determine the gross activity within a sample and possibly alpha/beta differentiation based upon energy curves, but not specific radionuclide identification.

Detection by scintillation depends on the radioactive material being located close to a molecule which can scintillate. Therefore, the radioactive material is typically dissolved in LSC cocktail which is composed of three components: a solvent, a wavelength shifter and an aromatic hydrocarbon. The scintillating component is the aromatic hydrocarbon molecule containing π-bonds in which an electron is excited upon interaction with radiation of sufficient energy. As these scintillators de-excite, photons are emitted. However, these photons are at energies which are not efficiently detected by the photomultiplier tubes (PMTs). Therefore another organic molecule, the wavelength shifter, is used to absorb the initial photons emitted by the scintillator

and re-emits another photon at more efficiently detected wavelength. Due to the fact that the sample is dissolved or in direct contact with the LSC cocktail, it provides 4π geometry which creates a sensitive technique for low energy beta (β) emitters as well as 100% detection efficiency for alpha particles. As the photons are emitted from the sample vial, they reach the two PMTs on opposite sides of the vial where the PMTs multiply the current produced by the light. In order to better accurately differentiate true radiation events from background sources, there are two PMTs arranged in such a way that only photons detected by both simultaneously will be counted, referred to as coincidence counting. The more photons detected and thus number of pulses recorded by the PMTs is therefore proportional to the energy of the radiation. The energy spectrum recorded however is not defined enough to use for radionuclide identification.[61]

The Perkin Elmer Tri-Carb 3100TR was used for LSC measurements. The QuantaSmart software was used for data acquisition and analysis.[62] In this thesis, dissolution samples containing radioactive material were monitored using this technique to determine gross activity.

For analysis of samples, a portion of the sample undergoing dissolution was pipetted into a 15 mL centrifuge vial and centrifuged at 5000 rpm for 16 minutes to separate the undissolved solid from the IL solution. Then a 0.1 to 0.25 mL aliquot was taken from the solution and mixed with 10 mL of Ultima Gold AB cocktail (Perkin Elmer) in a 20 mL high-density polyethylene (HDPE) vial. These HDPE vials provide lower background and high counting efficiency than glass vials and reduce the possibility of breaking. Since IL is rather viscous and traditional micropipettes do not dispense a reliable and accurate amount of material, the aliquots were typically gravimetrically measured for the amount added to the LSC cocktail. This extra step was not necessary when taking aliquots from aqueous solution. Ultima Gold AB was selected due to its durability with various acids.[63] Although this cocktail is more durable than most, chemical

and color quenching effects may still occur. These effects were taken into account during data analysis. Blanks were prepared by adding in equal volume of the reprensentative matrix, such as IL containing acid or exposed under similar conditions to an oxidizing gas, as the samples but without any radioactive material. Each sample was counted for an hour or until 10,000 total counts resulting in 1% error was reached. The samples were normalized to the mass of the aliquot added to the cocktail. The representative blank count rates were subtracted from the standards and dissolution samples. These mass normalized and background corrected count rates were used to determine the percent of the radioactive material which had dissolved into the solution up to complete dissolution.

2.3.6 Karl Fischer Titration

Karl Fischer coulometric titration is an effective analytical tool for determining the water content of a sample. The sensitivity of the method for water can easily approach 50 ppm and under strict methodology even down to 10 ppm. This method does however require consuming a portion of the sample in order to obtain the results. The Karl Fischer reaction is as follows in **Equations 13** and **14**.[64]

$$ROH+SO_2+RN \leftrightarrow (RNH)\cdot SO_3R \qquad \textbf{(Eq. 13)}$$

$$(RNH)\cdot SO_3R+2\ RN+I_2+H_2O \leftrightarrow (RNH)\cdot SO_4R+2\ (RNH)I \qquad \textbf{(Eq. 14)}$$

The coulometric cell for Karl Fischer titration is shown in **Figure 12**. The anolyte contains sulfur dioxide, imidazole and iodide in a methanol solvent. Iodine is generated electrochemically by anodic oxidation. The electrons released by the iodide to produce iodine are then able to pass through the diaphragm into the cathode compartment where positive hydrogen ions are reduced to hydrogen. An ammonium salt is used in the catholyte solution in order to

promote hydrogen production. Two iodine ions are converted to iodide and that then reacts with water. Therefore, based on Coulomb's law (2 x 96485 C) is needed to react with 1 mole of water. This interaction is used to calculate the water content from the measured current and time needed to reach the end point.[64]

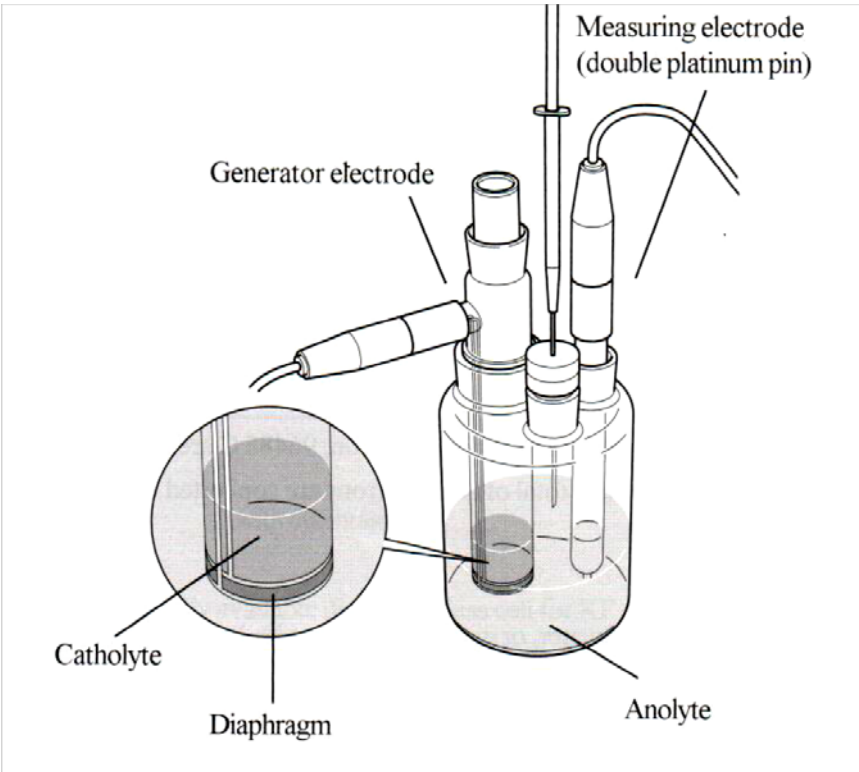


**Figure 12.** Representation of the Mettler Toledo D-32 Karl Fischer coulometric titrator

Karl Fischer titrations of IL samples were performed using a Mettler Toledo DL-32 titrator to determine the water content. A standard was used to calibrate the instrument and check proper detection performance using a HYDRANAL water standard 1.0 ($H_2O$ 1.011 ± 0.003 mg/g) prior to analyzing IL samples in triplicate. The instrument was operated with approximately 100 ml of the HYDRANAL analyte Coulomat A and 5 ml HYDRANAL catholyte Coloumat CG (Fluka).

### 2.3.7 Electrochemical Methods

#### 2.3.7.1 $Ag/Ag^+$ Non-Aqueous Reference Electrode

The reference electrode plays an important role in a three electrode electrochemical set-up. In effect, the reference electrode measures and controls the working electrode potential and the current is passed from the working electrode to the auxiliary, also known as the counter electrode. An $Ag/Ag^+$ (0.1M $AgNO_3$ in IL) non-aqueous reference electrode was utilized and prepared as described by Saheb et. al.[65] This process involves preparing a 1.0 M $Ag^+$ in acetonitrile solution by dissolving an appropriate amount of $AgNO_3$ and then using this solution to dilute a portion into the IL of choice, $[Me_3N^nBu][TFSI]$ , to a final $Ag^+$ concentration of 0.1 M. A glass electrode contained an Ag wire in contact with this $Ag^+$ solution and the electrode tip was either Vycor™ or Teflon (BASi Inc.). The reference electrodes were always stored when not in use in a container with the tip submerged in IL.

Electrochemistry in aqueous solutions often is performed with or reported in relation to the predominantly used normal hydrogen electrode (also known as the "standard hydrogen electrode" or SHE) or a saturated Ag/AgCl reference electrode. Literature provides references for redox potentials of species within aqueous solution in relation to the SHE which has had its standard electrode potential $E_o$ declared as zero. A species with a well-documented redox potential, such as that of ferrocene/ferrocenium ($Fc/Fc^+$), within the IL can be used to provide a relation between where the redox occurs within this IL system and reference electrode and the standard reference electrodes and potentials within literature.[24,26] The documented redox potential of the $Fc/Fc^+$ couple is +0.400 V vs SHE[24] or +0.203 V vs saturated Ag/AgCl. The $Ag/Ag^+$ $[Me_3N^nBu][TFSI]$ reference electrode was therefore periodically standardized with respect to a solution containing 4 - 5 mM ferrocene dissolved into $[Me_3N^nBu][TFSI]$. A typical

resulting offset potential based upon the response of ferrocene in this IL was + 0.416 V vs. Ag/AgCl, reflecting that the redox of ferrocene in this IL system and reference electrode is more negative than the documented $Fc/Fc^+$ redox potential reported in relation to Ag/AgCl. Effectively, the offset conveys that the potential should be adjusted by adding 0.416 V to reflect this difference and is used in reporting the data within this work in relation to a saturated Ag/AgCl reference electrode.

#### 2.3.7.2 Cyclic Voltammetry

Cyclic voltammetry (CV) is an electrochemical technique to evaluate the redox nature and reversibility of a species at the working electrode. During cyclic voltammetry the initial potential is changed towards a selected end potential and then returned (**Figure 13(a)**). When the potential applied is towards more negative potential, this is referred to as the cathodic scan and the species in solution is being reduced. When the applied potential is switched to more positive potential, this is the anodic scan and the species is being oxidized. A typical voltammogram is presented with potential, E, as the x-axis and resulting current, I, as the y-axis (**Figure 13(b)**).

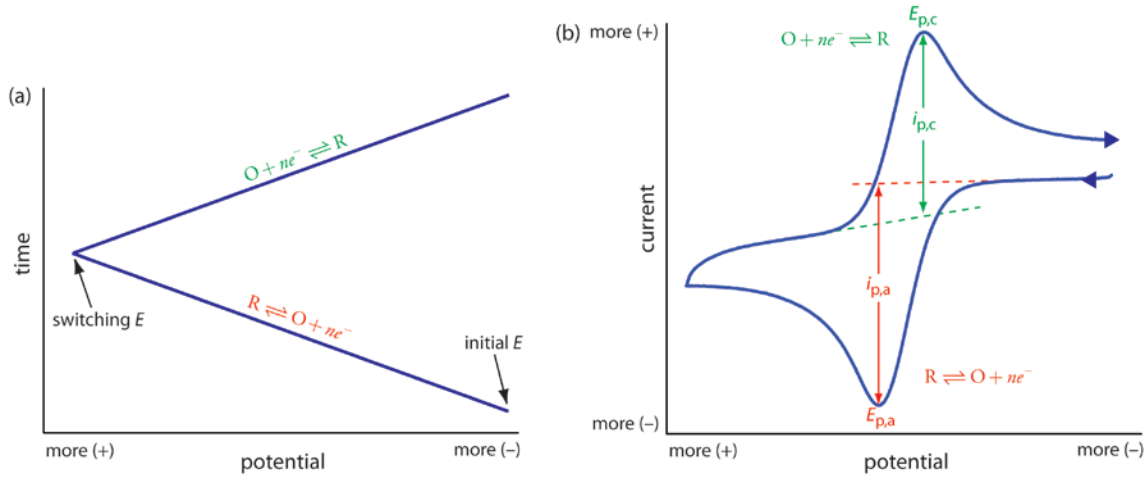


**Figure 13. (a)** graphical representation of cyclic voltammetry and the related electrochemical reactions as a result of applied potential, **(b)** typical cyclic voltammogram with assignment of cathodic and anodic peak potentials and currents.[66]

There are a number of contributing components to the peak current ($I_p$). In a reversible system the resulting peak current is directly proportional to the effective area of the working electrode (A) and the concentration of the species ($C_O$). In addition, there are influences from the scan rate ($\nu$) and the diffusion coefficient of the species within the electrochemical system ($D_O$). The relationship is represented as follows:[67]

$$I_p \propto n^{3/2} A D_O^{1/2} C_O \nu^{1/2} \quad \textbf{(Eq. 15)}$$

Where:

$I_p$= peak current, A

$n$ = number of electrons exchanged

A = effective area of the working electrode, $cm^2$

$D_O$ = diffusion coefficient of oxidized species, $cm^2/s$

$C_O$ = concentration of oxidized species, $mol/cm^3$

$\nu$ = scan rate, V/s

In an ideal system of reversible behavior and sufficiently fast kinetics, the Nernst equation (Eq. 16) applies to describe the potential as a relation of the number of electrons exchanged and the concentration of the oxidized and reduced species.[67]

$$E = E^{0'} + \frac{RT}{nF} \ln \frac{C_O}{C_R} \quad \textbf{(Eq. 16)}$$

Where:

$E^{0'}$ = formal potential (standard potential and activity coefficients)

R = Molar gas constant, 8.31447 J $mol^{-1}$ $K^{-1}$

T = temperature, K

*n* = number of electrons transported

$C_O/C_R$ = concentration of the oxidized and reduced forms of the species

All electrochemical measurements were conducted using a CH Instruments potentiostat (660C) or bipotentiostat (760B). A three electrode setup was utilized in all the measurements. The working electrodes were either a glassy carbon disc (3mm diameter), an Au disc (1.6 mm diameter), a Pt disc (1.6 mm diameter), or an Au mica or foil (effective size determined for each). An $Ag/Ag^+$ (0.1 M $Ag^+$ in IL) non-aqueous reference electrode was utilized.[65] A platinum sheet counter electrode (1.25 cm x 1.25 cm) was immersed in solution to ensure a surface area of 150 % relative to the working electrode area. Cyclic voltammetry was obtained for solutions that were at atmospheric temperature, pressure, and relative humidity unless stated otherwise such as being inside of an inert glovebox.

#### 2.3.7.3 Amperometric Deposition

The application of a constant potential for a period of time is referred to as chronoamperometry. After observing the electrochemical window for a given working electrode with the IL sample, a negative potential could be selected to attempt electrodeposition. The same three electrode electrochemical cell was setup as described previously. The amperometric i-t curve method is used within the CH instruments electrochemistry software when performing constant potential deposition attempts. Successful deposits often required potentials near -2 V or greater (more negative) and were allowed to deposit for 12 – 24 hours. Working electrodes that were a flat surface such as Au mica, Au foil, or grafoil were used so that collected deposits could

be more easily mounted for scanning electron microscopy (SEM) and energy dispersive X-ray spectroscopy (EDS) analysis after sufficient cleaning with ethanol. The Au mica was prepared by vacuum deposition chamber (Denton DV-502A) using Au ingot (99.99+%, Alfa Aesar) to an Au thickness of ~ 3000 Å. The Au foil was 0.025 mm thick 99.95% metal basis from Alfa Aesar. Grafoil was supplied by BASi Inc.

### 2.3.8 Scanning Electron Microscopy (SEM) and Energy Dispersive X-ray Spectroscopy (EDS)

Scanning electron microscopy is a versatile and commonly utilized form of microscopy that is well suited for the observation of topological and morphological sample features on a nanometer to micrometer scale. The SEM works by rastering electrons into a focused beam using electromagnetic lenses and scan across an area of the sample. As represented in **Figure 14**, the electrons interact with the sample and produce useful signals including secondary electrons, backscattered electrons, and characteristic X-rays, which are detected and transformed into an image.[60]

Secondary electron images provide excellent depth of field to aid in the study of morphological features. Backscattered electron images provide contrast as a function of the mean atomic number of the constituent atoms in the sample. Similarly, characteristic X-rays are emitted through the excitation of individual atoms and can be used for the semi-quantitative analysis of sample composition on the micrometer scale.

For SEM analysis, samples must be non-volatile to survive the vacuum environment and must be conductive to prevent charging by the electron beam. Non-conductive samples may be coated with a thin layer of a conductive substance such as carbon or gold.

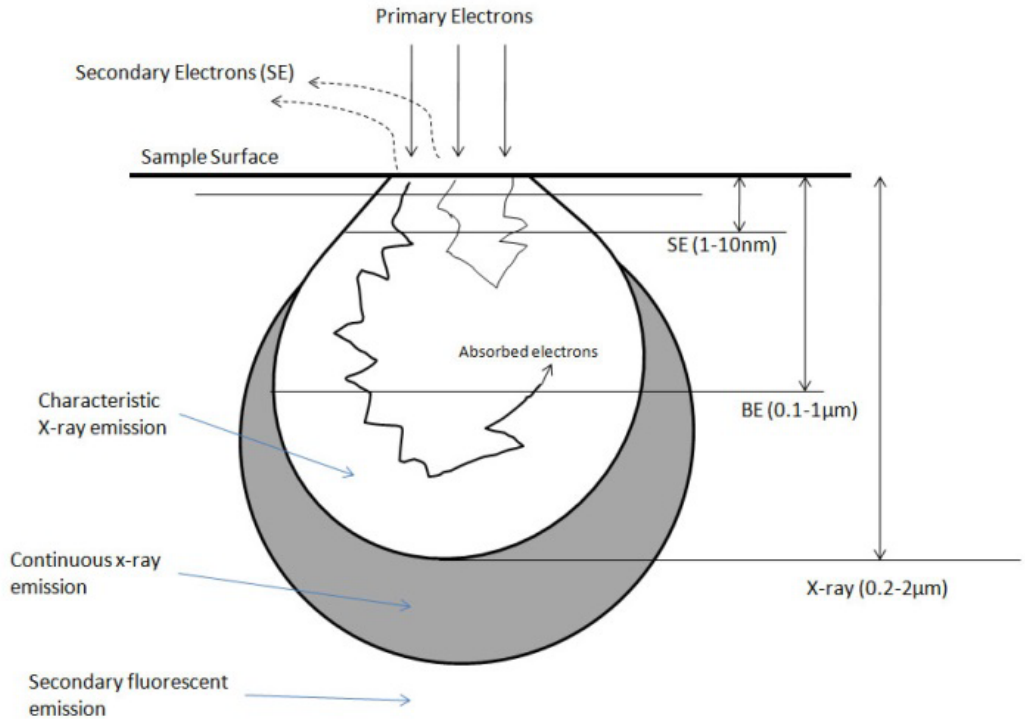


**Figure 14.** Interaction of the electron beam within a sample producing secondary and backscatter electrons for SEM imaging and X-ray emissions for EDS spectroscopy.

A JEOL-5610 scanning electron microscope equipped with a secondary electron and backscatter electron detectors was used to take images of the surface features of deposits on the electrode. Energy dispersive X-ray emission spectroscopy was performed to assist in identifying the elements present in deposits. The EDS was collected and identified using INCA mapping software. The accelerating voltage used was 20 kV with a working distance of 15-20 mm. Surface images were collected in secondary electron imaging mode.

### 2.3.9 Inductively Coupled Plasma – Atomic Emission Spectroscopy (ICP-AES)

Inductively coupled plasma atomic emission spectroscopy (ICP-AES), sometimes also referred to as inductively coupled plasma optical emission spectroscopy, is a commonly used technique for quantitative trace metal analysis. Samples are often prepared in dilute aqueous acid such as nitric or hydrochloric and the concentration of the metal analytes should be diluted if

necessary to concentrations in the 1 to 100 ppm range. The aqueous sample is pumped to a sample introductory system, a nebulizer in this case, and aerosolized by a carrier gas such as Argon. The aerosol then travels into the plasma and becomes atomized and ionized. The electrons of the atoms and ions are excited and upon de-excitation photons of wavelengths characteristic of that element are emitted. The photons are detected by an array of solid state detectors and the intensity of the light at that wavelength is typically indicative of the concentration of the corresponding element.[60]

ICP-AES was used to determine the concentration of uranium and neodymium in IL samples prior to electrodepositions and for resulting electrodeposits which were dissolved in 1 M $HClO_4$, work which was done at Los Alamos National Laboratory. Since the samples were in 1 M $HClO_4$, 2 % HCl was used for dilution in preparation of ICP-AES analysis and for the calibration standards. Diluted samples were analyzed on a Thermo Scientific iCAP 6500. Results were corrected by the appropriate dilution factor.

# Chapter 3. Electrochemical Study of Ferrocene, Acid, and Water in Ionic Liquid

This chapter provides an introduction to the electrochemistry of the IL $[Me_3N^nBu][TFSI]$ in the absence of dissolved metal species. The validation of the $Ag/Ag^+$ non-aqueous reference electrode and the potential scale for electrochemical measurements conducted in IL is established using the well-documented reduction potential of the ferrocene/ferrocenium redox couple. The effects of other components such as water and acid (HTFSI) in the IL are investigated for this reference electrode as well. The results demonstrate that the $Ag/Ag^+$ non-aqueous reference electrode is stable under these conditions providing a stable IL solvent system for electrochemical measurements.

Furthermore, an electrochemical method that utilizes the formation of gold oxide at an Au electrode surface and cathodic stripping voltammetry is investigated as a non-destructive method for the determination and monitoring of water content in the IL. The method was calibrated using increasing amounts of water added to the $[Me_3N^nBu][TFSI]$. The water concentration of "wet IL" was then evaluated and calculated from the voltammetry using both the charge and peak current from the reduction of gold oxide. This data was then compared directly with Karl Fischer data from the same samples. The quantitative determination of water in the IL was demonstrated for concentrations between 0.09 and 0.74 by weight (wt %). The treatment of wet IL by purging with dry nitrogen or molecular sieves reduced the water content to below background levels. Finally, an IL sample was electrochemically studied while taken through the process of added acid, neutralization, and the reduction of water with molecular sieves.

## 3.1 Introduction

Ionic liquids (ILs) are novel solvents due to their low volatility, chemical and thermal stability, and inherent conductivity. Water-stable second-generation ILs that include imidazolium, pyridinium, ammonium, phosphonium, and sulfonium cations paired with halides, $BF_4^-$, $CF_3CF_2CF_2CO_2^-$, $N(CN)_2^-$, and $N(SO_2CF_3)_2^-$ [TFSI] anions have been increasingly utilized in electrochemical applications. In comparison to first generation chloroaluminate ILs, they remain stable in the presence of water and do not require a controlled atmosphere to be utilized in electrochemical experiments.[68] The combination of bulky asymmetrical organic cations and organic with inorganic anions also produces solutions with high conductivity and large potential windows for electrochemical measurements.[69] Moreover, the properties of ILs are unique to the specific cation/anion pair and largely influence the physical and chemical characteristics of the systems.[32] Thus, combinations of different cation/anion pairs provide high flexibility in producing "designer solvents" with unique and/or synergistic properties.

The utility of ILs in electrochemical experiments is largely based on the ionic conductivity and the large potential window that can range from 4.5 to 6 V in the absence of appreciable water or oxygen. The potential range is based on the reduction potential of the cation, the oxidation potential of the anion, and the working electrode composition.[33,34] In contrast, the potential window for aqueous systems is constrained by water oxidation or metal oxide formation and hydrogen evolution.[23,24,25] The potential window for aqueous systems can range from 1.3 V to 2.5 V depending upon the electrode and electrolyte composition. The expanded potential limits of IL solutions allow the electrochemical properties of soluble species to be explored that are precluded in aqueous environments. However, water in the IL can produce aqueous side reactions such as the formation of metal oxide and hydrogen evolution at

the electrode surface that convolute the electrochemistry of other species.[70,71] Therefore, water in the IL may be an unwanted impurity during electrochemical measurements.

The chemical preparation, atmospheric humidity, and incorporation of "wet" chemical species can all contribute to the water concentration in ILs. Furthermore, the cation/anion pair directly influences the amount of water that can be incorporated into the IL. For example, previous studies have demonstrated that the hydrophobicity of the TFSI anion directly influences the water concentration in ILs.[72] A number of studies have also shown that an inhomogeneous dispersion of water can occur as the concentration increases producing aqueous microenvironments in ILs.[72,73] Water also increases the ionic conductivity while simultaneously decreasing the viscosity of the IL. Although the changes in the viscosity and ionic conductivity seem advantageous, the simultaneous narrowing of the electrochemical window is not favorable.[70,74]

Karl Fischer titration is currently the most common analytical method for determining the water concentration in ILs. While the method provides high analytical precision and accuracy with detection limits for water of 10 ppm, it requires consumable reagents and destroys the IL sample. In addition, the alcohol-based reagent used in the titration can react with ILs that contain carboxylic groups, producing water and positive error in the measurement.[75] In contrast, infrared (IR) spectroscopy is a non-destructive method that can be used to measured water concentrations in IL. However, the technique requires specialized instrumentation and is relatively expensive when compared to Karl Fischer titration.[76] More recently, the analysis of water in IL using cathodic stripping voltammetry of gold oxide has been utilized as an in-situ method.[75] The analysis provided a quantitative measure of the water for multiple IL systems and concentrations ranging between 0.005 and 0.345 wt % by weight. However, only the peak current for reduction

of gold oxide (**Equation 4**) was utilized to construct the calibration plots. The concentrations were also below water saturation for the group of ILs studied. Finally, two different regions of linearity were reported for the gold oxide reduction. The results suggest that the electrochemical reduction of gold oxide might be related to two different processes as the concentration of water increases in the IL. Specifically, changes in the electrode surface properties (passivation) or kinetic limitations may contribute to the two different regions of linearity for the calibration plots.[77]

The combined use of water and acid to increase the solubility of metal oxide and carbonate species in IL solutions has been examined.[78,79] The chemical species, bis(trifluoromethanesulfonyl)imide [HTFSI], was utilized to provide a common acid species in ILs that contain the bis(trifluoromethanesulfonyl)imide anion [$TFSI^-$]. Although the evolution of hydrogen at gold and platinum in the IL n-trimethyl-n-butylammonium bis(trifluoromethanesulfonyl)imide [$Me_3N^nBu$][TFSI] containing HTFSI has been achieved, the results indicate that the acid is only partially dissociated.[22,80] However, increasing the water concentration enhanced the proton dissociation and the acid strength, increasing the solubility of the metal species in the IL. The combined roles of water and acid on the electrochemical properties of soluble species in IL solutions have not been extensively studied. However, the deposition of gold at graphite was shown to be an electroless process with acid and kinetically hindered when water is present in the IL.[81] Therefore, acid neutralization and water reduction may be equally important in the electrochemical measurement of other soluble species in ILs.

In the present studies, the in-situ qualitative and quantitative determination of water in the IL, [$Me_3N^nBu$][TFSI], was achieved using cathodic stripping voltammetry of gold oxide. Karl Fischer titration data was obtained for the same samples and utilized for the direct comparison of

water concentrations derived from the electrochemical measurements. The peak current ($I_{pc}$) and charge (Q) associated with the reduction of gold oxide were used to construct calibration plots for the concentration range that encompasses the water saturated IL. In contrast to the previous study, both sets of data were plotted to ensure that the calibration plots are consistent over the entire concentration range for both electrochemical parameter.[75] In addition, the oxidation/reduction of ferrocene was examined to determine if water and acid species influence the electrochemical properties of soluble species in the IL. Two different methods are examined and compared that utilize either dried nitrogen degassing or the addition of molecular sieves to reduce water in the IL. Finally, the addition of HTFSI, neutralization, and reduction of water is demonstrated for the IL. Cyclic voltammetry was utilized to monitoring water and acid through each step. The methods derived in these studies provide analytical tools for identifying and methods for reducing acid and water in ILs prior to electrochemical characterization of soluble species.

## 3.2 Methods and Materials

### 3.2.1 Chemicals and Solutions

The IL, n-trimethyl-n-butylammonium bis(trifluoromethanesulfonyl)imide, ($[Me_3N^nBu][TFSI]$), (Solvionic, 99.5 %, AM0408B), HYDRANAL water standard 1.0 (Fluka, 34828), HYDRANAL Coulomat CG (Fluka, 34840), HYDRANAL Coulomat A (Fluka, 34807), Ferrocene (Sigma Aldrich, 98 %, F408), bis(trifluoromethanesulfonyl)imide , HTFSI (Synquest Labratories, 99 %, 8169-3-06) Concentrated $NH_4OH$ (EM Science), were all used as received. Molecular sieves (UOP Type 3A, Fluka, 02573) were dried in an oven at 200°C prior to use. The water utilized in the studies was obtained using a Barnstead D4641 Epure system (> 18 Ω cm).

### 3.2.2 Preparation of the Reference Electrode and Ionic Liquid Samples

The non-aqueous $Ag/Ag^+$ was prepared as described previously in Chapter 2 (section 2.3.7.1). IL samples included the neat $[Me_3N^nBu][TFSI]$, a water saturated sample, and another containing 0.5 M HTFSI. After background scans were collected under the same electrochemical parameters, ferrocene was added to a portion of the sample to result in a 10 mM concentration.

The $[Me_3N^nBu][TFSI]$ was obtained from an unopened bottle. Increasing amounts of ultrapure water were added to 10 mL aliquots of IL by micropipette. In addition, a 10 mL aliquot of IL solution was placed in contact with 10 mL of water. All samples were sonicated for 20 minutes to produce even mixing and allowed to sit for 24 hours prior to use. A water saturated IL sample was also utilized in the studies for reducing the water concentration in IL. For future reference, all concentrations will be reported as wt % to indicate “by weight”. All samples were stoppered and stored inside a desiccator while not in use to ensure no additional uptake of water.

### 3.2.3 Karl Fischer Titration

Karl Fischer measurements with the IL were performed using a Mettler Toledo DL-32 titrator to determine the water concentration. The instrument was set-up and operated as outlined in Chapter 2 (section 2.3.6). All samples were measured in triplicate.

### 3.2.4 Electrochemical Apparatus and Conditions

All electrochemical measurements were performed using a CH Instruments 660C potentiostat/galvanostat in a three electrode configuration as outlined previously in Chapter 2 (section 2.3.7.2). The reference electrode was standardized with respect to a $[Me_3N^nBu][TFSI]$ solution containing 4 mM ferrocene, providing an offset potential of 0.452 V vs. Ag/AgCl. All cyclic voltammograms have been corrected such that the potential scale is referenced versus Ag/AgCl (3 M KCl). All electrochemical experiments were conducted at room temperature using

a scan rate of 100 mV/s. The gold electrode was held at a constant potential of 0.252 V for 600 seconds to reduce any surface species prior to the electrochemical measurements. The electrode was then held at a potential of 0.252 V for 300 seconds prior to cycling between 0.252 and 2.102 and V vs. Ag/AgCl. The same parameters and procedures were used to ensure reproducibility of all the gold oxide electrochemical measurements. Electrochemical glassware was dried at 180 °C and allowed to cool to room temperature in a desiccator prior to use.

3.2.5 Water Reduction Using Dry Inert Gas and Molecular Sieves

Nitrogen gas was passed through a gas drying tube containing 8-mesh drierite to remove residual water prior to the degassing. All samples were examined with cyclic voltammetry to estimate water concentration prior to purging and then again after 2, 4, 6, and 12 hour intervals of purging with the dried nitrogen gas. The water concentration was determined using Karl Fischer titration after each purge.

The molecular sieves were placed in an oven at 200 °C to activate for at least 24 hours before use. The water saturated IL sample was analyzed electrochemically before adding any molecular sieves. Molecular sieves were added to the water saturated IL (~2 g per addition) and stirred for two hours and then filtered. Electrochemical measurements were obtained after each addition and Karl Fischer titration was used to evaluate the water concentration.

3.2.6 Addition of HTFSI, Neutralizing, and Drying of Ionic Liquid

A sample of $[Me_3N^nBu][TFSI]$ was initially dried by molecular sieves. A portion of the dried IL was acidified by addition of HTFSI (0.5 M). Next, a 10 mL portion of the IL containing 0.5 M HTFSI was neutralized by addition of 0.345 mL concentrated $NH_4OH$ and left to stir overnight. Finally, 10 g of the neutralized IL was put into a new vial and 5.0005 g of molecular

sieves were added to remove water. The electrochemical method for water determination and Karl Fischer titration were used to examine each sample after each treatment.

3.3 Effects on the Reference Electrode: Ferrocene, Acid, and Water in Ionic Liquid

The voltammetric responses of a gold electrode immersed in IL solution containing 10 mM ferrocene with 0.09 wt % or 1.38 wt % water were examined to ensure that shifts in the gold oxide reduction potentials were not a function of changes in the junction potential of the reference electrode, **Figure 15(a)** and **(b)**. Ferrocene was chosen due to its notable reversibility and use as a standard for normalizing IL reference electrodes.[65] For comparison, the voltammetry of the IL containing 1.38 wt % water is also provided in **Figure 15(c)**. Despite a significant difference in water concentration between the two IL samples, the peak splitting remained constant ($\Delta E_p$ = 107 mV) and the peak oxidation/reduction potentials only varied by ~ 9 mV.

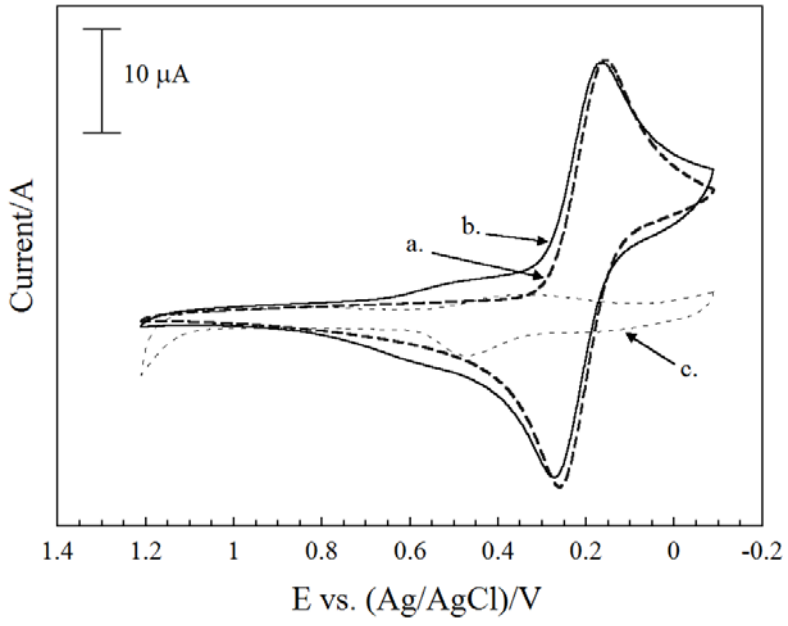


**Figure 15.** Cyclic voltammogram of 10 mM Ferrocene in [$Me_3N^nBu$][TFSI] containing **(a)** 0.09 %, **(b)** and 1.38 % water. **(c)** A background of [$Me_3N^nBu$][TFSI] containing 1.38 % water before the addition of ferrocene is provided for comparison. Scan rate 100 mV/s.

The cyclic voltammetry of 10 mM ferrocene in IL before and after addition of 0.5 M HTFSI was also examined in **Figure 16(a)** and **(b)**. For comparison the cyclic voltammetry of the IL containing 0.5 M HTFSI is also provided **Figure 16(c)**. The peak splitting remains constant ($\Delta E_p$ = 103 mV) and the peak oxidation/reduction potentials were shifted by ~ 15 mV. The value is slightly larger than the shift observed for water only. However, the data again indicates that the acid and water do not cause large shifts in the junction potential.

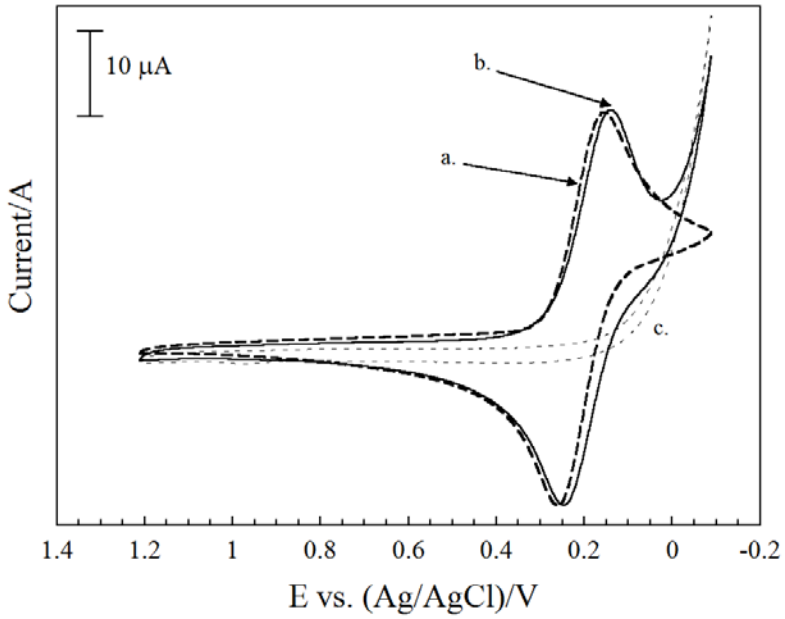


**Figure 16. (a)** Cyclic voltammogram of 10 mM Ferrocene in $[Me_3N^nBu][TFSI]$ with 0.5 M HTFSI (**b**) and after adding sieves, 0.3778 % and 0.0583 % $H_2O$, respectively.**(c)** A background of $[Me_3N^nBu][TFSI]$ containing 0.5 M HTFSI before the addition of ferrocene is provided for comparison. Scan rate 100 mV/s.

3.4 Electrochemical Determination of Water at an Au Electrode in an Ionic Liquid

Cyclic voltammetry was used to examine the IL, $[Me_3N^nBu][TFSI]$, containing increasing amounts of water. IL samples containing between 0.09 wt % (residual) and 1.38 wt % (saturated) water were equilibrated in closed containers for a minimum of twenty-four hours prior to the electrochemical measurements. Select cyclic voltammetry for these samples are

provided in **Figure 17** for clarity. Two voltammetric processes are observed during the oxidative scan for all samples, labeled (I) and (II). In contrast, a single cathodic "stripping" wave (I′/II′) from the reduction of the gold oxide is observed on the reverse scan for all samples. The mechanism for the formation of gold oxide can be attributed to the two distinct oxidative processes. The first involves the adsorption of water on the gold electrode surface and the formation of AuO, **Equation 17**,[82] wave I. Then the oxidation of AuO to $Au_2O_3$ occurs in the presence of water at more positive potential, **Equation 18**,[82] wave II. The formation of $Au_2O_3$ is consistent with the reduction processes in **Equation 4**, I′/II′. The potential for the initial formation of AuO (I) shifts to more negative potential and the charge remains constant as the water concentration increases. Formation of $Au_2O_3$ (II) increases and shifts to more negative potential as water concentration in the IL increases from 0.09 wt % to 1.38 wt %. Similar behavior is observed for the single reduction wave (I′/II′) and the peak potential ($E_p$) shifts from 1.174 V to 0.903 V (- 271 mV) as the water concentration is increased.

$$Au\ (s) + H_2O \longrightarrow AuO\ (s) + 2\ H^+ + 2\ e^- \qquad \textbf{(Eq. 17)}$$

$$2AuO\ (s) + H_2O \longrightarrow Au_2O_3\ (s) + 2\ H^+ + 2\ e^- \qquad \textbf{(Eq. 18)}$$

The data indicates that the shifts in potential observed for the reduction of gold oxide are not a function of changes in the junction potential as the water concentration increases. Therefore, the potential shifts for voltammetric waves I and I′/II′ are likely influenced by the increasing water concentration.[73,74,83]

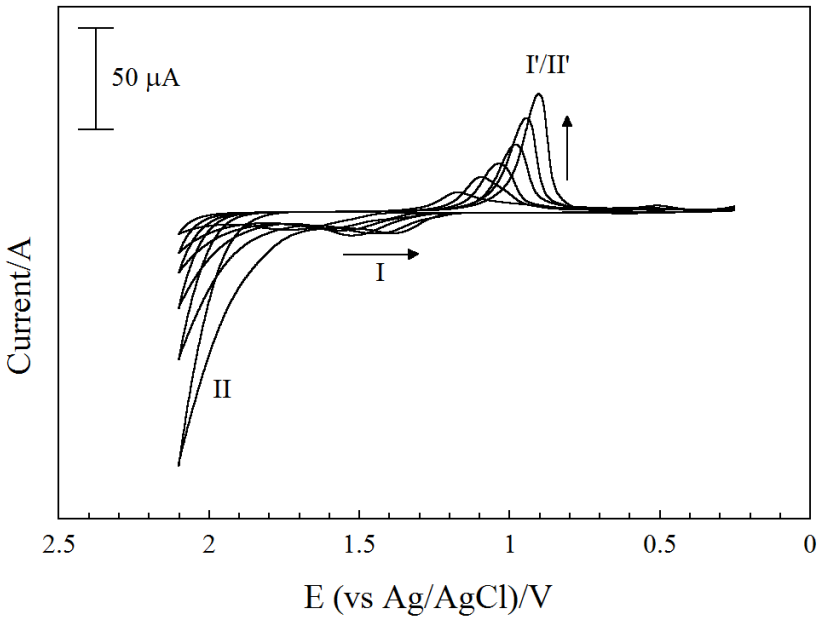


**Figure 17.** Cyclic voltammetry of gold electrode in $[Me_3N^nBu][TFSI]$ containing increasing water. Scan rate 100 mV/s.

The peak current ($I_{pc}$) and charge (Q) for the voltammetric wave associated with the reduction process (I′/II′) are utilized in constructing the calibration plots. The previous studies of gold oxidation/reduction for ILs containing water focused on the peak current when constructing calibration plots.[75] In our studies, the average peak current and charge are calculated from four steady state voltammetric responses. A plot of the charge associated with the reduction wave (I'/II') and oxidation wave (I) as a function of the percent water in the IL is presented in **Figure 18**. Similarly, a plot of the peak current as a function of the percent water in the IL is provided in **Figure 19**.

The shape of the plots for the charge and peak current are very similar. The charge and peak current associated with initial oxidation of the gold surface (I) to form AuO remains constant over the concentration range studied. The data is consistent with the initial formation of AuO and subsequent oxidation at more positive potential to form $Au_2O_3$.[82] In addition, both the charge and peak current have linear regions between 0.09 wt % and 0.74 wt % water in the IL.

The charge and peak current also reach constant values when the water concentrations exceed 0.74 wt %. The data suggests that the formation of $Au_2O_3$ is constant after the water concentration reaches 0.74 wt % for the electrochemical parameters used in the present studies. In contrast, the previous studies identified two linear regions with useful portion at concentrations between 0.005 – 0.345 wt % for ILs 1-*n*-butyl-3-methylimidazolium tetrafluoroborate, [BMIM][$BF_4$], 1-*n*-butyl-3-methylimidazolium hexafluorophosphate, [BMIM][$PF_6$], bis(2-hydroxyethyl)ammonium acetate, [DEA][Ac], and triethylammonium acetate, [TetA][Ac].[75] It is possible that the gold oxide formed during the oxidation processes remains constant at higher water concentrations for the series of ILs reported in the literature. However, the lower sensitivity linear regions for higher water concentrations were not shown.

Analysis of the linear region provides regression coefficients of $R^2 = 0.9716$ and 0.9914 for the charge and peak current data, respectively. From the data in the linear range for charge under the reduction peak the limit of detection for this electrochemical method of water determination was determined to be 0.1375 ± 0.0061 wt %. This is higher than the onset of the linear range in the data and may be due to a limited number of data points within the linear range. Although quantitative determination is limited, the electrochemical method can still be utilized for qualitative assessment outside of the region of linear response. The limited quantitative range of the electrochemical method at an Au electrode necessitated Karl Fisher measurements of water in the IL outside the linear range. A summary of the water concentrations in IL obtained from Karl Fischer titration and the comparable values calculated from the peak current plot are provided in **Table 3**. The water concentrations derived from the electrochemical data are consistent with the values obtained from the Karl Fischer titration.

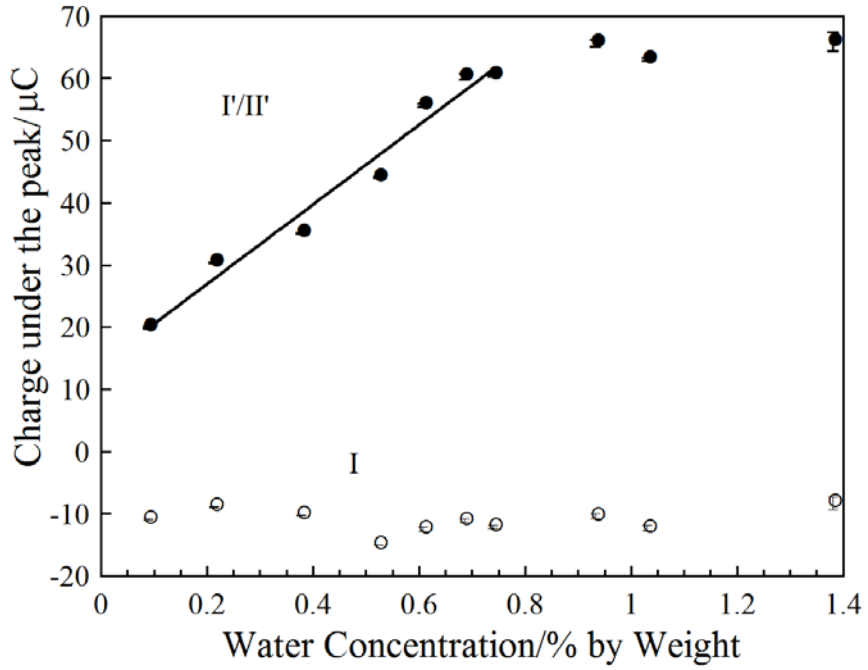


**Figure 18.** Linear fit of percent water in IL vs. charge under the peak. Reduction peak (solid circles), oxidation peak (open circles).

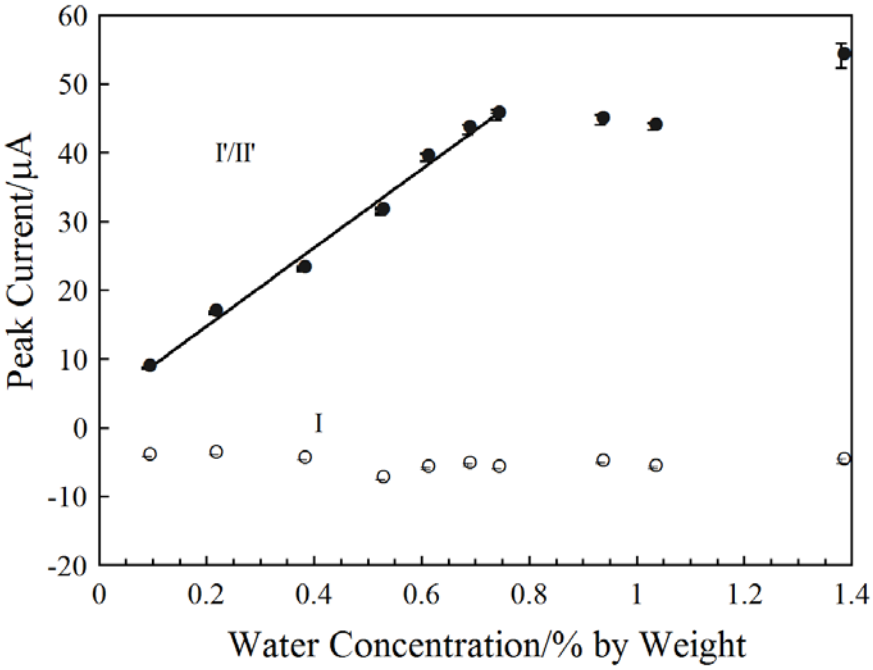


**Figure 19.** Linear fit of percent water in IL vs. peak current. Reduction peak (solid circles), oxidation peak (open circles).

**Table 3.** Summary of the concentration of water in IL determined using Karl Fischer titration and the water concentration in each sample derived from the linear fit of plots for the water concentration as a function of the charge (Q) and peak current ($I_{pc}$) for the reduction of gold oxide (I′/II′).

| % water added | % water (KF) | water, molarity (KF) | % water from Q (CV) | molarity water from Q (CV) | % water from Ipc (CV) | molarity water from Ipc (CV) |
|---|---|---|---|---|---|---|
| 0.08 | 0.09 | 0.07 | 0.09 | 0.07 | 0.09 | 0.07 |
| 0.21 | 0.21 | 0.17 | 0.25 | 0.20 | 0.23 | 0.18 |
| 0.38 | 0.38 | 0.30 | 0.33 | 0.26 | 0.35 | 0.27 |
| 0.56 | 0.52 | 0.41 | 0.47 | 0.37 | 0.49 | 0.39 |
| 0.66 | 0.61 | 0.48 | 0.65 | 0.51 | 0.63 | 0.49 |
| 0.75 | 0.69 | 0.54 | 0.72 | 0.56 | 0.70 | 0.55 |
| 0.84 | 0.74 | 0.58 | 0.72 | 0.57 | 0.74 | 0.58 |
| 0.94 | 0.93 | 0.73 | | | | |
| 1.03 | 1.03 | 0.81 | | | | |
| saturated | 1.38 | 1.08 | | | | |

Our previous studies have shown that the dissolution of chemical species such as metal oxides or carbonates results in an increase in the water concentration in the IL. For instance, the water concentration of a sample of IL increased from 0.0298 ± 0.0005 wt % to 0.5405 ± 0.0057 wt % following the direct dissolution of $Ce_2CO_3$ into the $[Me_3N^nBu][TFSI]$ containing HTFSI.[79] Therefore, the dissolution of carbonate and oxide species significantly increases the water concentration in the IL. However, the wet IL can be purged with dry nitrogen after dissolution processes and prior to electrochemical measurements. In addition, positive pressures of dry inert gas delivered over the top of the IL after purging minimize further uptake of water from the atmosphere. The process is detailed in the cyclic votlammteric responses of water saturated and nitrogen purged IL that are provided in **Figure 20(a)** and **(b)**, respectively. A significant reduction in the initial water concentration (1.38 wt %) occurs within 2 hours of purging the IL with dry nitrogen. Purging for an additional 4, 6, and 12 hours results in a slight reduction of the water concentration when compared to the sample treated for two hours, **Figure 20(c)**. The low

volatility of the IL also ensures that the total volume remains constant after purging. The concentration based on Karl Fischer titration was 0.064 ± 0.002 wt % after 12 hours of purging. This measurement is lower than IL taken from the bottle without treatment (0.09 wt %) and far below the saturated sample prior to treatment (1.38 wt %).

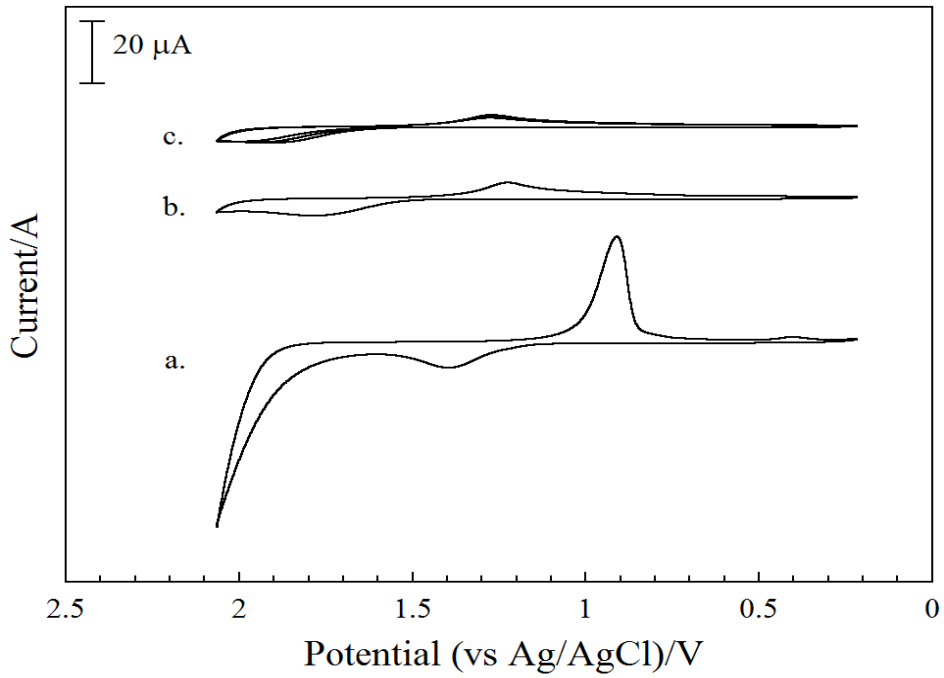


**Figure 20. (a)** Cyclic voltammogram of water-saturated [$Me_3N^nBu$][TFSI], **(b)** after purging with dried nitrogen gas for 2 hours, **(c)** after purging with dried nitrogen gas for 4, 6, and 12 hours. Scan rate 100 mV/s.

Alternatively, molecular sieves were utilized without purging to reduce the water concentration in the IL. The cyclic voltammetric responses of the water saturated IL (1.38 wt %) and the sample after two gram additions of molecular sieves are provided in **Figure 21**. A significant reduction in the water concentration between the saturated sample in **Figure 21(a)** and after the first addition of the molecular sieves is observed in **Figure 21(b)**. The second and third additions of molecular sieves further reduced the water concentration, **Figure 21(c)**.

However, the most significant reduction of water in the IL occurs after the first addition of molecular sieves. Karl Fischer titration of the IL after the third addition of sieves provided a water concentration of 0.027 ± 0.003 wt %. This value is again below the linear range for quantitative measurement using the gold oxide calibration plot. The use of molecular sieves provides water concentrations that are lower than those achieved using a dry gas purge for two hours. Both methods can be used independently or together to reduce the water in IL solutions and minimize the impact of atmospheric water uptake during electrochemical measurements.

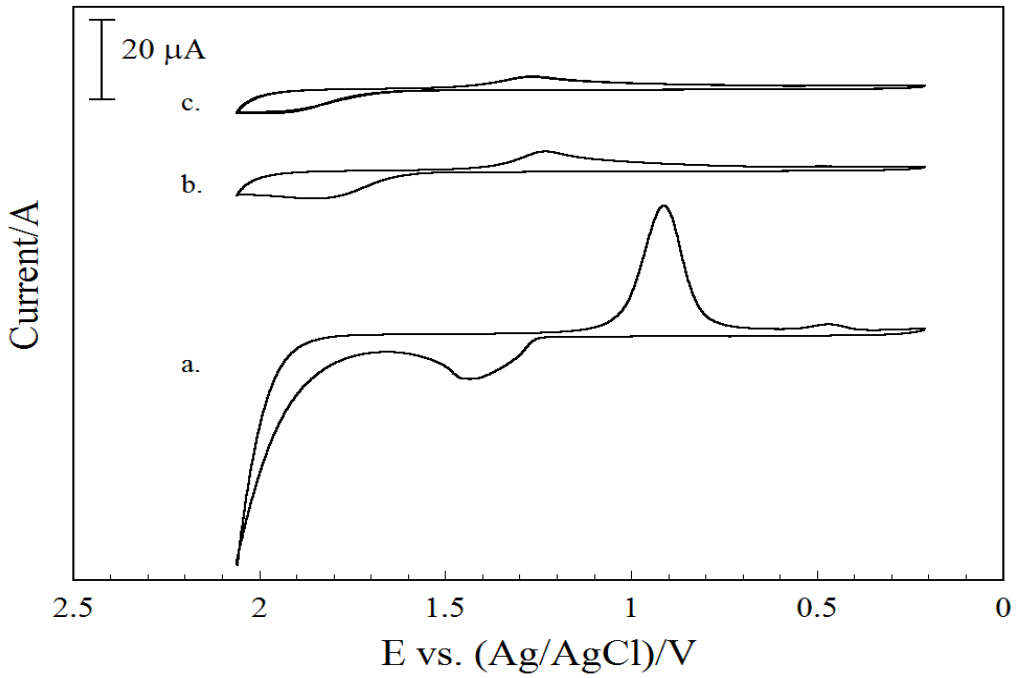


**Figure 21. (a)** Cyclic voltammogram of water-saturated [$Me_3N^nBu$][TFSI], **(b)** after the first addition of molecular sieves, 2 hours, **(c)** after second and third additions of molecular sieves, 2 hours each. Scan rate 100 mV/s.

The inclusion of water and acid in IL influences the potential window and ultimate reduction potential that is achievable in electrochemical experiments.[70,74] The dissolution of metal oxides and carbonates can produce IL solutions that contain added water and leave residual

acid.[22,80] Furthermore, both unreacted and partially dissociated acid are present in both the IL and water. The remaining acid must be neutralization prior to the reduction of water in the IL. The goal is to reduce the concentration of the two species and provide the largest potential window for the electrochemical analysis of soluble species in the IL. The electrochemical response of an Au electrode in untreated IL containing 0.06 wt% water is provided in **Figure 22(a)**.

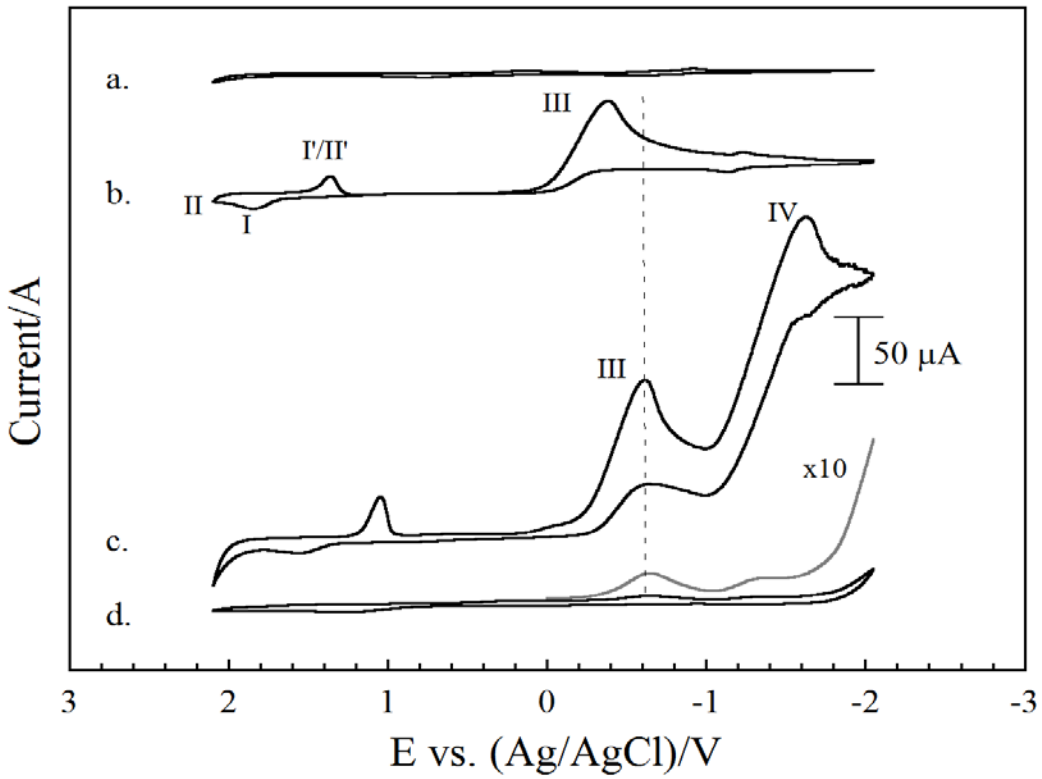


**Figure 22. (a)** Full scans and water determination at Au electrode of: initial dry $[Me_3N^nBu][TFSI]$, **(b)** IL containing 0.5 M HTFSI, **(c)** neutralized, **(d)** final dried IL by molecular sieves. Scan rate 100 mV/s.

For comparison, the electrochemical response of the IL after the addition of 0.5 M HTFSI is provided in **Figure 22(b)**. An increase in the water concentration (0.373 wt %) in the IL occurs after the addition of HTFSI, which is consistent with the contribution from the wet acid. An additional voltammetric wave is observed in the cyclic voltammetry using an extended

potential window, wave III, at -0.380 V vs. Ag/AgCl, which is related to the adsorption of proton to the gold electrode surface.[81,84].

The neutralization of solvated proton and remaining acid in the IL is achieved using stoichometric amounts of $NH_4OH$, which produces additional water in the system. The water concentration was measured using Karl Fischer titration following the neutralization at 1.53 wt %. The value is higher than the concentration obtained from the direct contact of water with the (1.38 wt %) suggesting higher water concentrations are possible in the IL when produced from the in-situ neutralization of acid. The cyclic voltammetric response for the IL treated with $NH_4OH$ is provided in **Figure 22(c)**. In contrast to the single voltammetric wave (III) observed after the addition of HTFSI in **Figure 22(b)**, an additional wave is observed at -1.626 V (IV). Wave III also shifts from -0.380 V to -0.612 V vs. Ag/AgCl as the water concentration increases. Both voltammetric waves are consistent with the sorption of proton at the gold electrode and with visible hydrogen evolution at potentials negative of -1.650 V. The electrochemical response suggests that hydrogen evolution can occur at the gold electrode as the water concentration increases within the IL. Furthermore, the change in water concentration after acid neutralization (1.53 wt %) is sufficient to produce water microenvironments with dissociated acid in the IL that facilitate hydrogen evolution. Finally, the water saturated IL obtained from the neutralization step was dried using molecular sieves (5.0005 g) reducing the water concentration to 0.0354 wt %. The electrochemical processes associated with the acid are still observed in **Figure 22(d)** based on the enhanced current (x10) cyclic. The data indicates that HTFSI is not completely neutralized by the added base. However, it is clear that the IL approaches the background conditions in **Figure 22(a)** with respect to water because the characteristic reduction of $Au_2O_3$

has not been resolved. The data suggests that water and acid can be incorporated in the IL, identified using electrochemical methods, and minimized prior to subsequent measurements.

## 3.5 Conclusions

The inclusion of secondary species such as water and acid in second generation ILs can reduce the potential window and produce side reactions that convolute the electrochemical analysis of other soluble species. The cyclic voltammetry of ferrocene in the IL containing water and acid demonstrates that the junction potential of the reference electrode does not change appreciably. Therefore, as long as the reference electrode used is checked for its response with ferrocene and effective offset potential on a consistent basis, the inclusion of water or the HTFSI acid will not introduce other potential problems associated with the electrochemical system.

The electrochemical measurements demonstrate that the oxidation of gold is consistent with the formation of AuO followed by the conversion of this species to $Au_2O_3$ at more positive potentials when water is present in the IL. Therefore, only a single reduction wave for the cathodic stripping of $Au_2O_3$ is observed on the reverse scan. Cathodic stripping analysis of the reduction of gold oxide provides an in-situ electrochemical method to quantitatively measure the water concentration, with a linear range between 0.09 – 0.74 wt % for the IL, $[Me_3N^nBu][TFSI]$, as a function of either the reduction peak current ($I_{pc}$) or charge under the peak ($Q_c$). The electrochemical formation of bulk gold oxide remains constant and independent of water concentration in excess of 0.74 wt % in the IL. However, cathodic stripping analysis is also a useful qualitative tool for monitoring water in the IL for concentrations that are outside the linear range. In addition, the cathodic stripping analysis of gold oxide after purging with dry nitrogen or treatment with molecular sieves show that these methods are effective in reducing the water concentration to levels below the background.

Electrochemical measurements also clearly demonstrated that hydrogen evolution at the gold electrode occurs when both water and acid (HTFSI) are present in the IL. The data indicates that the dissociation of proton is enhanced in water contained within the IL. Finally, the neutralization of acid species HTFSI and water reduction was achieved using a two-step process. The acid was neutralized with ammonium hydroxide and then treated using molecular sieves to reduce the water concentration below the background level for the IL prior to use. The methods evaluated in this chapter demonstrate that the neutralization of acid and subsequent reduction of water can be achieved to minimize their impact in subsequent electrochemical measurements.

# Chapter 4: Dissolution of Cerium Carbonate in Ionic Liquid and Electrochemical Studies

This chapter evaluates the introduction of lanthanide species into the IL through direct dissolution of cerium carbonate, $Ce_2(CO_3)_3 \cdot xH_2O$. The study utilizes the IL n-trimethyl-n-butylammonium bis(trifluoromethanesulfonyl)imide $[Me_3N^nBu][TFSI]$ with conjugate acid bis(trifluoromethanesulfonyl)imide [HTFSI]. The displacement of carbonate ligand and formation of carbonic acid facilitates the in-situ dissolution. The subsequent coordination of Ce with the TFSI ion in the IL is monitored using UV-Vis spectroscopy and emergent ligand to metal transitions below 300 nm. Further evidence of the coordination of Ce in the IL is based on changes in the IR spectra for absorbance bands related to the sulfonyl functional groups of the TFSI anion. The reduction/oxidation of soluble Ce in IL is examined at Au, Pt, and GC (glassy carbon) electrodes. Multi-wave voltammetry at all three electrodes is consistent with the reductive deposition of Ce species from the IL solution. Scanning electron microscopy (SEM) and energy dispersive x-ray spectroscopy (EDS) confirm the deposition of Ce species at mica/Au electrodes.

## 4.1 Introduction

A great deal of experimental effort has been devoted to elucidating the electrochemistry of the Ce(III)/Ce(IV) redox couple relative to the side reactions in aqueous solutions.[14,85,86,87-91] The studies demonstrate that the solution and electrochemical parameters for common working electrodes including Au, Pt, and GC do not produce fully reversible oxidation/reduction of the Ce(III)/Ce(IV) couple and the deposition of Ce species was not achieved. The research approach highlights the difficulties that exist with respect to defining a universal, optimum working

electrode and the solution conditions required to evaluate the oxidation/reduction processes of lanthanide species in aqueous solutions.

The potential window in aqueous solutions at positive potential is constrained by water oxidation or metal oxide formation. Hydrogen evolution at negative potentials at both Pt and Au metal surfaces influences the negative potential limit achievable for the reduction of electropositive lanthanides in water. The prohibitive potentials associated with these reactions in an aqueous system were previously noted in Chapter 1 (Equations 3-6).[23,24,25]

Cerium has a characteristically negative reduction potential, which is commonly encountered with the lanthanides and actinides. The potentials required for the reduction of Ce in aqueous solution are provided for comparison.[26]

$$Ce^{4+} + e^- \rightleftharpoons Ce^{3+} \qquad E° = 1.523 \text{ V vs. Ag/AgCl} \qquad (\textbf{Eq. 19})$$

$$Ce^{3+} + 3e^- \rightleftharpoons Ce^0 \qquad E° = -2.537 \text{ V vs. Ag/AgCl} \qquad (\textbf{Eq. 20})$$

The reduction of $Ce^{3+}$ to metal in aqueous solution is inhibited by hydrogen evolution at negative potential for Au and Pt electrodes. In contrast, the oxidation/reduction of lanthanides at Hg electrodes in aqueous solution and the formation of stable amalgams have been demonstrated.[28-31,92] The evolution of hydrogen is less thermodynamically favorable at Hg electrodes facilitating the reduction of metals ions and the formation of stable amalgams.[28-31,92] These types of studies have been used to establish the thermodynamic potentials for lanthanide and actinide reduction at the Hg electrode for aqueous solutions.[26] Unfortunately, recovering the lanthanide metal from the Hg amalgam is not trivial. Thus, the use of Hg metal electrodes in electrochemical processes is not ideal and environmental issues associated with the electrode remain a significant drawback.

The disadvantages associated with the previous aqueous systems can be minimized using ILs that provide a wide range of tunable physical and chemical properties.[14,32] For example, the potentials for anion oxidation and cation reduction in IL solutions typically occur at more positive and negative potentials relative to water oxidation and hydrogen evolution, respectively. The potential windows associated with working electrodes for the IL used in this study, n-trimethyl-n-butylammonium bis(trifluoromethanesulfonyl)imide ($[Me_3N^nBu][TFSI]$) are approximately 4.5 V for Pt, 5.0 V for Au, and 6.0 V for glassy carbon, respectively.[33-36] Moreover, the negative potential limits for the IL are sufficiently negative that the reduction of both lanthanides and actinides to metal is thermodynamically feasible.

The electrochemical properties of lanthanides including La,[16] Tm,[37] Eu,[16,37,38] Sm, [16,38,39] Yb,[38,39] and Dy[40] in various IL solutions have been reported. The studies have examined the interfacial oxidation/reduction of the species in IL solution without surface deposition,[16,37,38] and the stepwise reduction and deposition of the metal species.[16,39,40] The studies provide the proof of principal that IL solutions can be utilized to examine both the interfacial oxidation/reduction and deposition of lanthanides. The oxidation/reduction of the ($M^{3+}/M^{2+}$) lanthanide couple have been resolved for Sm,[16] La,[16] Eu,[16,37] and Tm[37] in ILs. The electrochemical deposition of Eu and Sm has also been demonstrated from solutions containing $Sm(TFSI)_3$ and $Eu(TFSI)_3$[16,39] and the electrochemical deposition of Dy has been documented.[40] The studies confirm that sufficiently negative potentials can be achieved which allow the deposition of lanthanide species at electrode surfaces to be examined.

Although the electrochemical properties of lanthanides in a variety of ILs have been documented, low metal ion solubility is problematic. Two different experimental approaches have been utilized to increase the solubility of metal species in ILs. For example, the dissolution

of lanthanide oxides in water containing bis(trifluoromethanesulfonyl)imide [HTFSI] has been achieved, producing species of the general form, $Ln(TFSI)_3(H_2O)_3$ (Ln = La(III), Sm(III), and Eu(III)).[16] In addition, thorium nitrate hexahydrate was used to produce $[Th(TFSI)_4(HTFSI)]\cdot H_2O$ after isolating and reacting the hydroxide derivative with HTFSI in aqueous solution.[15] The lanthanide and actinide TFSI complexes produced using aqueous solutions have been successfully dissolved directly into $[Me_3N^nBu][TFSI]$ with enhanced solubility. The electrochemical deposition of metallic La, Sm, Eu and Th was also achieved using these solutions.[15,16] Alternatively, "task specific" ILs that contain carboxyl-functionalized cations were used to dissolve metal species including actinide and trivalent lanthanides (e.g. $UO_2$, $UO_3$, $Sm_2O_3$, $Eu_2O_3$, and $Nd_2O_3$) directly into ILs without additional acid.[17,18,19] However, the addition of water was required to facilitate the deprotonation of the carboxylic group and increase solubility of the lanthanide oxides in IL.[17,40] Similarly, although the dissolution of $UO_3$ was demonstrated for "task specific" ILs at elevated temperatures (373 K) the experimental conditions did not achieve full dissolution and the deposition of the actinide species was not extensively examined.[18]

The direct dissolution of lanthanide carbonates into IL containing the acid HTFSI can also be envisioned based on the previous studies. Moreover, the inclusion of HTFSI into $[Me_3N^nBu][TFSI]$ provides proton for the dissolution while limiting inclusion of competing ligands that may also complex with the soluble lanthanide species. Finally, the use of lanthanide carbonate species allows the $CO_3^{2-}$ anion to be targeted without the addition of water or elevated temperatures to facilitate the dissolution in the IL. The general dissolution reaction for trivalent lanthanide (Ln) carbonates was provided previously in **Equation 1** (Chapter 1).

The proposed dissolution mechanism assumes that protons from HTFSI dissociated and react with the carbonate ligand to produce carbonic acid. However, the concept of acidic ILs and acid strength has only been recently examined for different ILs and acids. For example, HTFSI was added to a variety of different ILs to produced "protic" ILs.[20] The evolution of hydrogen in the IL solutions was achieved which suggests the proton is at least partially dissociated from the acid. In addition, the acidity of ILs containing HTFSI or carboxylic acids was evaluated using various protic indicators.[22,80] Both studies suggest that proton dissociation from the acid is diminished in IL, reducing the overall acid strength when compared to aqueous solution environments. However, the results demonstrate that the partial dissociation of protons from HTFSI occurs in various ILs.[20,22,80]

The direct dissolution of $Ce_2(CO_3)_3$ in $[Me_3N^nBu][TFSI]$ containing HTFSI was examined. One goal was to influence the solubility of $Ce_2(CO_3)_3$ through the protonation of the carbonate and subsequent formation of carbonic acid. The acid, HTFSI, was specifically chosen to facilitate the dissolution and in-situ formation of stable TFSI complexes in the absence of carbonate. The IL solutions containing soluble Ce are characterized using UV-Vis and IR spectroscopy. Finally, the electrochemical properties of the IL containing soluble Ce were examined using cyclic voltammetry at Au, Pt and Glassy Carbon (GC) electrodes. The preliminary electrochemical studies provide evidence for the surface deposition of Ce species from the IL and SEM/EDS analysis were used to verify the deposition of Ce species on an Au sheet electrode.

## 4.2 Methods and Materials

### 4.2.1 Chemicals and Solutions

The IL, n-trimethyl-n-butylammonium bis(trifluoromethanesulfonyl)imide, $[Me_3N^nBu][TFSI]$ (99.5%, Solvionic), bis(trifluoromethanesulfonyl)imide [HTFSI] (>95%, Fluka), and the cerium (III) carbonate hydrate, $Ce_2(CO_3)_3 \cdot xH_2O$, (99.999%, Alfa Aesar) were used as received.

A stock solution of the $[Me_3N^nBu][TFSI]$ containing 2.811 g HTFSI (99.8 mM, 100 mL) was prepared. For the direct dissolution, 16 mL of the stock solution was diluted with $[Me_3N^nBu][TFSI]$ to 20 mL total volume (80 mM HTFSI) and the $Ce_2(CO_3)_3 \cdot xH_2O$ (0.0461 g) was then added to the solution and stirred while bubbling with argon for 48 hours to produce an IL solution containing ~10 mM Ce. The 100 mM Ce solution was prepared using the same method with 0.463 g $Ce_2(CO_3)_3 \cdot xH_2O$ in 20 mL of IL containing 800 mM HTFSI. All solutions containing soluble Ce in IL were purged with desiccated argon to reduce water content before spectroscopic or electrochemical analysis and the final water content for the solutions was confirmed using Karl Fischer titration.

4.2.2 Karl Fischer Titration

Karl Fischer titrations of the IL were performed using a Mettler Toledo DL-32 titrator to determine the water content. The instrument was calibrated using a HYDRANAL water standard 1.0 ($H_2O$ 1.011 ± 0.003 mg/g) prior to the analysis of IL samples. The instrument was operated with 100 mL of the HYDRANAL analyte Coulomat A and 5 mL HYDRANAL catholyte Coloumat CG (Fluka), respectively.

4.2.3 UV-Visible and IR Spectroscopy

All UV-visible spectra were collected at room temperature in a 1 cm quartz cell on a Cary 6000i double beam spectrometer. The UV-Vis spectrum for the solution of $[Me_3N^nBu][TFSI]$ containing 80 mM HTFSI was referenced versus a $[Me_3N^nBu][TFSI]$ background. Similarly, all

solutions containing soluble Ce in IL were referenced versus a background obtained using $[Me_3N^nBu][TFSI]$ containing 80 mM HTFSI. The dilutions were conducted with the 80 mM HTFSI to ensure a constant background.

All IR spectra were obtained with a Varian 3100 FT-IR Excalibur series spectrometer using a Smiths detection DurasamplIR in a compartment diamond attenuated total reflectance (ATR) attachment using Varian Resolutions Pro, version 5.04.009 software. The IL solutions were analyzed directly on the stage under ambient conditions at 4 $cm^{-1}$ resolution.

4.2.4 Electrochemical Apparatus and Conditions

All electrochemical measurements were performed using a CH Instruments 660C potentiostat/galvanostat with included software. The experiments were performed in a one-compartment, three-electrode cell after Ar degassing. A Pt sheet counter electrode was used with an immersed area exceeding the working electrode by a factor of two. A 2 mm diameter Au disc electrode ($3.14 \times 10^{-2}$ $cm^2$), 2 mm diameter Pt disc electrode ($3.14 \times 10^{-2}$ $cm^2$), and a 3 mm diameter glassy carbon disc (area = $7.07 \times 10^{-2}$ $cm^2$) were utilized as working electrodes for the electrochemical measurements. An Au sheet (3000 Å of Au on mica) electrode was used to obtain Ce deposits to provide a suitable flat substrate for SEM and EDS analysis. The reference electrode was prepared according to literature[65] and consisted of an Ag wire in contact with 0.1 M $Ag^+$ in the IL with a Vycor™ frit acting as the double junction. The reference electrode was standardized with respect to a $[Me_3N^nBu][TFSI]$ solution containing 4 mM ferrocene providing an offset potential of + 0.416 V vs. Ag/AgCl. All cyclic voltammograms are referenced versus Ag/AgCl (3 M KCl) based on the Ag/Ag+ electrode and the $Fc/Fc^+$ redox couple.

4.2.5 Scanning Electron Microscopy and Energy-Dispersive X-ray Spectroscopy (SEM/EDS)

The SEM/EDS measurements were collected using a JEOL-5610 scanning electron microscope equipped with a secondary electron and backscatter electron detectors with elemental analysis capability using EDS. Initially, the Au electrode surface was not extensively washed with ethanol prior to analysis to ensure surface stability of the Ce deposits on the thin (3000 Å) Au surface. However, the electrode surface was more extensively rinsed with ethanol to remove excessive IL prior to a second set of EDS measurements.

4.3 Direct Dissolution of $Ce_2(CO_3)_3 \cdot xH_2O$ into Ionic Liquid

The direct dissolution of $Ce_2(CO_3)_3 \cdot xH_2O$ using HTFSI in the IL $[Me_3N^nBu][TFSI]$ can be considered based on **Equations 7, 8, and 9** (Chapter 2) :

$$Ce_2(CO_3)_3 \cdot xH_2O + 6\ HTFSI \xrightarrow[H_2O]{[Me_3N^nBu][TFSI]} 2\ Ce(TFSI)_3 + 3\ H_2CO_3 + xH_2O \xrightarrow{Ar} 3\ H_2O + 3\ CO_2$$

$$Ce_2(CO_3)_3 \cdot xH_2O + 10\ HTFSI \xrightarrow[H_2O]{[Me_3N^nBu][TFSI]} 2\ Ce(TFSI)_5^{2-} + 4\ H^+ + 3\ H_2CO_3 + xH_2O \xrightarrow{Ar} 3\ H_2O + 3\ CO_2$$

The mechanism assumes that Ce forms a neutral complex $Ce(TFSI)_3$. In addition, homoleptic lanthanide TFSI complexes with the general form $[Ln(TFSI)_5]^{2-}$ where Ln = Nd and Tb, have also been prepared in IL containing pyridinium cations. Thus the formation of a charged Ce complex is also possible.

The dissolution was confirmed visually for each solution after addition of $Ce_2(CO_3)_3 \cdot xH_2O$ to the IL containing HTFSI. The water from the decomposition of carbonic acid

combines with the inherent water from the IL and cerium carbonate. Degassing the IL with argon was conducted to reduce the water from the dissolution reaction. However, water was not completely eliminated from the IL despite degassing for 24 hours. Karl-Fischer analysis of the ionic solution containing 10 mM Ce a provided a measure of the water content after the direct dissolution of $Ce_2(CO_3)_3$ ($H_2O$ = 0.5405 ± 0.0057 wt %) and after purging with Ar (0.0304 ± 0.0017 wt %). The value for the Ar purged solution is consistent with the water content of the IL prior to dissolution (0.0298 ± 0.0005 wt %). The data suggests that water coordination with the soluble Ce may be minimized in IL because the concentration can be reduced to background levels after the dissolution.

4.4 UV-Visible and IR Spectroscopy of Soluble Cerium in Ionic Liquid

The spectroscopic properties of soluble Ce in IL were evaluated, **Figure 23(a)**. The spectrum for 10 mM Ce dissolved in IL is characterized by high absorbance between 270-210 nm and lower absorbance between 300-280 nm. The absorbance was sufficiently high for the 10 mM Ce solution that a series of dilutions were performed using $[Me_3N^nBu][TFSI]$ containing 80 mM HTFSI as the diluent providing final Ce concentrations of 0.1, 0.25, 0.5, 1, and 2 mM,, **Figure 23(a)**. The dilutions allow the fine structure associated with soluble Ce to be elucidated in the spectra. The absorbance spectrum for $[Me_3N^nBu][TFSI]$ containing only 80 mM HTFSI does not show the same fine structure. Rather, the spectrum for 80 mM HTFSI in IL displays a high intensity band at ~210 nm with a second less intense band at ~280 nm. Therefore, the fine structure observed for soluble Ce cannot be attributed to either HTFSI or $TFSI^-$ in IL.

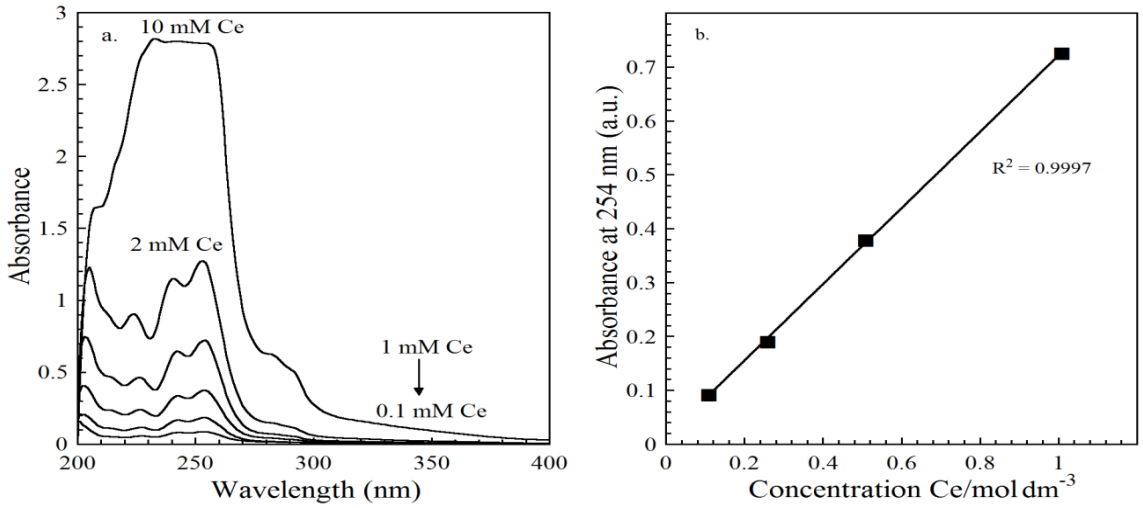


**Figure 23. (a)** The UV-Vis absorbance spectra of 10 mM Ce in $[Me_3N^nBu][TFSI]$ containing 80 mM HTFSI and subsequent dilutions (2, 1, 0.5, 0.25, and 0.1 mM soluble Ce) versus a background of $[Me_3N^nBu][TFSI]$ containing 80 mM HTFSI. The dilutions were achieved using $[Me_3N^nBu][TFSI]$ containing 80 mM HTFSI. **(b)** Linear plot of the absorbance (254 nm) versus concentration of soluble Ce.

The absorbance fine structure is indicative of multiple electronic transitions associated with the soluble Ce which suggest that either $Ce(TFSI)_3$ or $Ce(TFSI)_5^{2-}$ forms during the direct dissolution of $Ce_2(CO_3)_3$ into $[Me_3N^nBu][TFSI]$ containing 80 mM HTFSI. The absorbance can be attributed to ligand to metal charge transfer complexes which have been previously observed with weakly coordinating ligands, including TFSI which are sensitizing agents for high energy electronic transitions.[93] The molar absorptivities can be calculated for the absorbance bands at 254, 242, and 226 nm providing average values of $\varepsilon = 736 \pm 13.3$, $662 \pm 1.6$, and $471 \pm 6.43$ L $M^{-1}$ $cm^{-1}$, respectively. These values are consistent with molar absorptivity values for lanthanide complexes that exhibit metal/ligand charge transfer below 300 nm.[94] Further analysis of the spectral band at 254 nm was conducted and a plot of the absorbance maxima as a function of Ce concentration is provided in **Figure 23(b)**, displaying a linear response ($R^2 = 0.9997$) between 1 mM and 0.1 mM Ce. In fact, the 254 nm has been used previously as the excitation wavelength

for luminescence studies of cerium in ILs.[95] However, a search of the literature yielded no previous examples of UV-Visible absorbance for cerium species dissolved in ILs. Therefore, additional FT-IR measurements were conducted to evaluate the coordination between Ce and TFSI in the IL.

The solubility of Ce was also examined using FT-IR spectroscopy which can provide information regarding changes in vibrational energies associated with given functional groups associated with either the cation or anion in the IL. The spectra for $[Me_3N^nBu][TFSI]$ containing 80 mM HTFSI (dashed line) and 10 mM soluble Ce (solid line) are provide in **Figure 24(a)**. For comparison, the IR spectra for $[Me_3N^nBu][TFSI]$ containing 800 mM HTFSI (dashed line) and a solution containing 100 mM soluble Ce (solid line) are provided in **Figure 24(b)**.

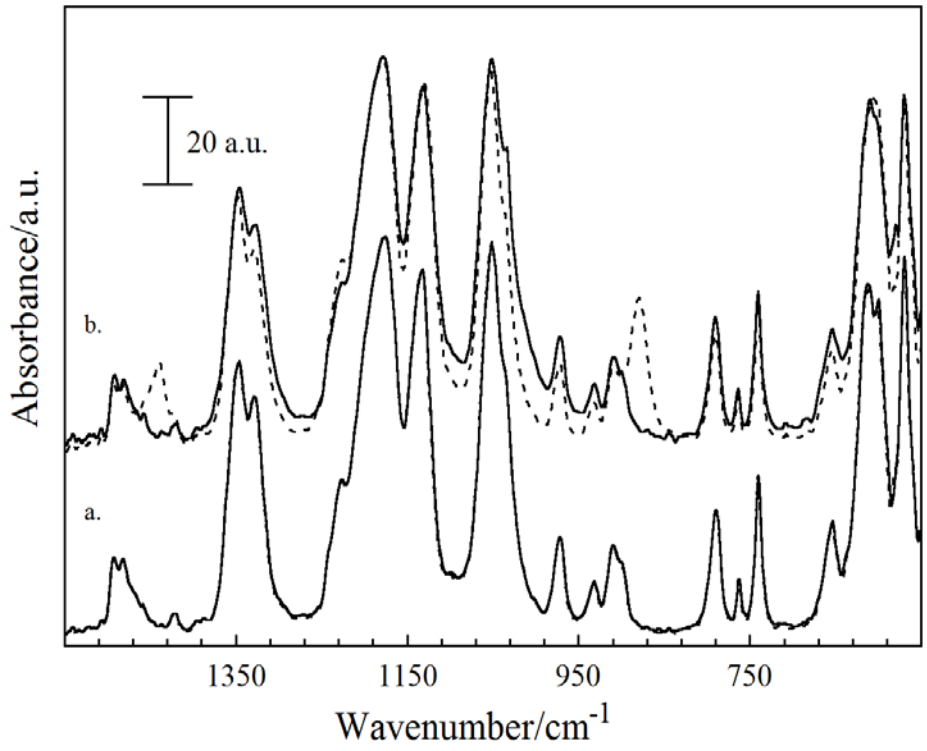


**Figure 24. (a)** IR absorbance spectra of $[Me_3N^nBu][TFSI]$ containing 80 mM HTFSI (dashed line), and with 10 mM soluble Ce (solid line). **(b)** IR absorbance spectra of $[Me_3N^nBu][TFSI]$ containing 800 mM HTFSI (dashed line) and with 100 mM soluble Ce (solid line).

The spectral bands associated with given funcitonal groups have been previously assigned for ILs containing TFSI in the literature.[96-99] For comparison, the assignment of bands for the $[Me_3N^nBu][TFSI]$ containing HTFSI and soluble Ce are provided with corresponding assigments from the literature and data from the IL manufacturer (Solvionic)[100] in **Table 4**. The experimental IR results indicate that the direct dissolution of the cerium carbonate (10 mM and 100 mM soluble Ce) into the IL does not drastically influence the band positions associated with the bulk TFSI ligand.

**Table 4.** Absorbance band assignments for the IR spectra of $[Me_3N^nBu][TFSI]$ containing HTFSI and soluble Ce (10 mM and 100 mM). For comparison, the band assignments for $[Me_3N^nBu][TFSI]$ from Solvionic are provided. ($\delta$ = bending, $\nu$ = stretching, a = asymmetric, s = symmetric, i.p. = in-plane, and o.p. = out-of-plane).

| Band Assignment | IL, 10 mM Ce ($cm^{-1}$) | IL, 100 mM Ce ($cm^{-1}$) | IL, Solvionic ($cm^{-1}$) |
|---|---|---|---|
| $\delta_a CF_3$ | 571 | 571 | 569 |
| $\delta_a^{i.p.} SO_2$ | 602 | 602 | 600 |
| $\delta_a^{o.p.} SO_2$ | 613 | 613 | 612 |
| $\delta SNS$ | 656 | 654 | 654 |
| $\delta_a CF_3$ | 741 | 741 | 740 |
| $\nu CS$ | 791 | 791 | 790 |
| $\nu_a SNS$ | 1053 | 1051 | 1051 |
| $\nu_s SO_2$ | 1134 | 1132 | 1132 |
| $\nu_a CF_3$ | 1177 | 1179 | 1176 |
| $\nu_a^{o.p.} SO_2$ | 1327 | 1327 | 1328 |
| $\nu_a^{i.p.} SO_2$ | 1346 | 1346 | 1346 |
| $\nu CH_3$ | 1481 | 1481 | 1481 |
| $\nu CH_3$ | 1493 | 1493 | 1492 |

The interaction between the soluble Ce and TFSI is not significantly strong to influence the energies relative to the bulk IL. However, previous studies have shown that the TFSI ligand can complex with metal species in the absence of stronger coordinating ligands through the sulfonyl oxygen.[16,57,101,102] Although there are no changes in band position, there are some minor changes in the absorbance intensities of bands associated with the TFSI ligand for the 10 mM Ce sample in **Figure 24(a)**. Minor changes in the absorbance intensity are observed for the $\delta(CF_3)$ (571 $cm^{-1}$) and in-plane $\delta^{i.p.}(SO_2)$ (602 $cm^{-1}$) bending modes of the TFSI ligand. For example, a

small increase in the intensity for the $CF_3$ functional group is observed relative to the background, 80 mM HTFSI in $[Me_3N^nBu][TFSI]$. In addition, the absorbance intensity for the $SO_2$ functional groups decreases relative to the background. Finally, the absorbance intensity associated with the ν(SNS) stretching mode at 1053 $cm^{-1}$ increases. The intensity of each band is likely influenced by the coordination between the soluble Ce and the TFSI ligand.

In spite of the relatively low concentration of soluble Ce for both concentrations (10 mM or 100 mM) versus the TFSI anion (~ 4 – 4.8 M), changes in band intensities for the TFSI functional groups are more pronounced with increasing Ce content. In addition, the $[Me_3N^nBu][TFSI]$ containing only 800 mM HTFSI displays two bands at 880 $cm^{-1}$ and 1439 $cm^{-1}$, which are not present in all other spectra. The bands have been previously assigned to the $\nu_aSNS$ mode at 860 $cm^{-1}$ and $\nu_aSO_2$ mode at 1440 $cm^{-1}$ for the IR spectra of HTFSI gas.[98] The loss of the two bands in the IR response for 100 mM Ce in IL may be indicative of the loss of HTFSI through the proton assisted dissolution of $Ce_2(CO_3)_3$.

Although the band intensities for TFSI were not dramatically influenced by low concentrations of Ce, more substantial changes are observed as the concentration increases. Changes in intensities for every band associated with the sulfonyl moeity are observed in **Figure 24(b)**. The bands associated with the $\delta_a^{i.p.}SO_2$ (602 $cm^{-1}$) and $\delta_a^{o.p.}SO_2$ (613 $cm^{-1}$) decrease and increase in intensity, respectively. The data may be indicative of a small conformational change in the bound TFSI relative to the bulk IL. In addition, the $\nu_a^{o.p.}SO_2$ (1327 $cm^{-1}$) and $\nu_a^{i.p.}SO_2$ (1346 $cm^{-1}$) bands increase in intensity with increasing Ce solubility. Finally, an additional band (shoulder) emerges at lower energy (1034 $cm^{-1}$) when compared to the $\nu_aSNS$ (1051 $cm^{-1}$) band. The emergence of the band at lower energy is consistent with the increased interaction of the TFSI ligand with soluble Ce.

4.5 Electrochemistry

The oxidation/reduction processes associated with the soluble Ce in IL were examined using cyclic voltammetry. The background cyclic voltammetry for an Au electrode in $[Me_3N^nBu][TFSI]$ containing 80 mM HTFSI (dashed line) is provided for reference in **Figure 25(a)**. The assignments for the voltammetric waves for **Figure 25(a)** are based on previous voltammetric studies of Au in IL containing HTFSI.[81]

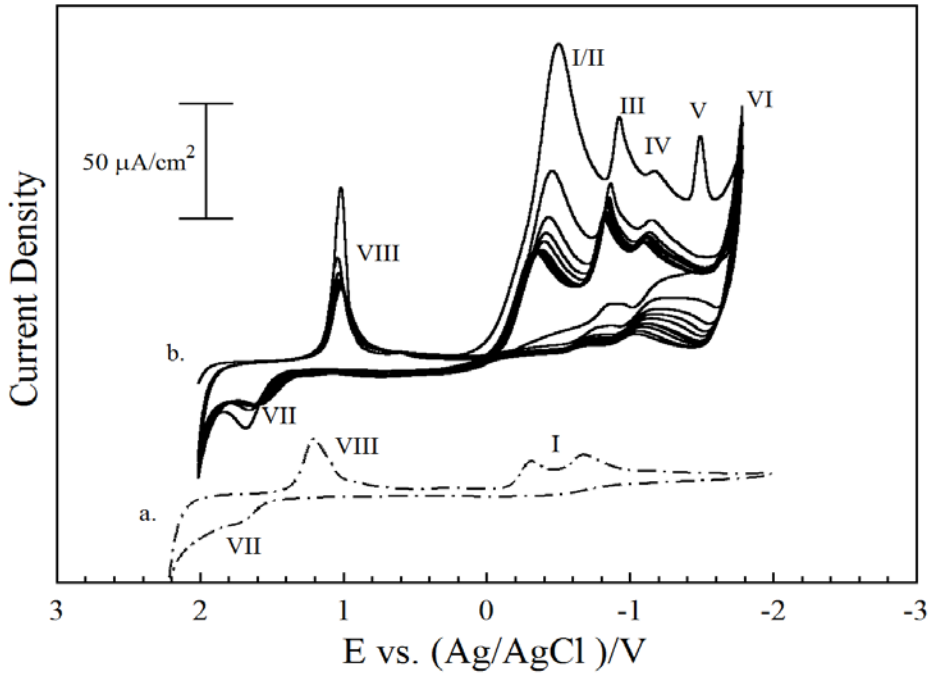


**Figure 25.** Cyclic voltammograms for **(a)** an Au disc electrode in $[Me_3N^nBu][TFSI]$ containing 80 mM HTFSI (dashed line) and **(b)** an Au disc electrode in $[Me_3N^nBu][TFSI]$ containing 80 mM HTFSI with 10 mM soluble Ce (solid line) from the direct dissolution. Scan rate = 50 mV/s.

For example, the two wave voltammetric reduction labeled I can be attributed to the reductive adsorption of $H^+$ which is followed by the surface adsorbed H reaction with $H^+$ and subsequent reduction, producing $H_2$ at the Au electrode surface.[84] In addition, the voltammetric waves labeled VII and VIII were previously assigned to the oxidation of the TFSI anion and the

reductive desorption of degradation species from this process. However, the formation of gold oxide at the electrode surface may also be possible based on the residual water and the HTFSI in the IL. The gold oxide formed during the anodic scan would then be reduced on the cathodic scan (Chapter 1, **Equation 4**).

The cyclic voltammetric response for an Au electrode immersed in IL containing 10 mM soluble Ce in IL $[Me_3N^nBu][TFSI]$ is also provided in **Figure 25(b)**. The voltammetric waves VII and VIII are also resolved in the IL solutions containing soluble Ce. However, the reduction shifts to negative potential relative to the background. The oxidation process initially overlaps with the background and then shifts to negative potential with each voltammetric cycle. The dissolution of $Ce_2(CO_3)_3$ may influence the electrochemical processes associated with waves VII and VIII based on decreasing proton concentration, the formation of carbonic acid, and the inclusion of soluble Ce. However, further studies are required to determine if voltammetric waves VII and VIII are primarily influenced by the electrochemistry of the TFSI anion or the changing concentrations associated with $H^+$ and soluble Ce.[81,84] Finally, the voltammetric response decreases with each sequential scan reaching steady state after ~ 6 cycles suggesting the Au surface is modified due to surface adsorption.

The voltammetric response for the first cathodic scan in **Figure 25(b)** features reduction waves labeled I/II, III, IV, V, and VI between 0 and -1.8 V. Although there is overlap between the voltammetry in **Figure 25(a)** and **Figure 25(b)** the current density is significantly larger for IL containing soluble Ce when compared with the background voltammetry. Initial decreases in current density for the voltammetric waves I/II are larger than either wave III, and IV. In addition, waves I/II and III also shifts gradually to more positive potentials with each sequential scan. The electrochemistry for waves I/II and III likely contain contributions from both $H^+$ and

Ce in the IL.[81,84] The decrease in current density and shift in potentials for the waves suggest that as Ce species are deposited the surface processes associated with $H^+$ are reduced due to loss of active Au electrode surface area. Furthermore, water may also play a role in the voltammetric response for wave IV based on previous studies of HTFSI in "wet" IL.[84] However, the water content for the IL containing soluble Ce and the background were comparable after Ar degassing based on Karl Fischer titration. The lack of reduction processes for the background IL at potentials more negative of -1 V indicates that the contribution of water is minimal and the voltammetric response is likely due to the reduction of Ce species in the IL. The assignment of the possible reaction for wave V at Au was not attempted because it was only observed for the first voltammetric scan and is absent in the steady-state response. The possible reactions and voltammetric wave assignments for the Au electrode are provide in **Table 5,** with additional assignments for the Pt and GC electrodes discussed in the next few paragraphs.

In spite of the possible contributions from $H^+$ and water, the data indicates the reductive adsorption of the Ce species at Au occurs. The overlap of the voltammetric response for waves I/II, III, and IV suggests that that the sequential loss of the TFSI anion occurs as Ce species are reduced at the Au surface. At sufficiently negative potential the one-step, bulk reduction of the Ce and loss of TFSI ligand at the Au surface is possible (VI). For comparison, the anodic scan shows three relatively small oxidation waves with diminished current relative to the reduction processes. The irreversible nature of the voltammetry suggests that the oxidative desorption of Ce species from the Au electrode is kinetically hindered. Furthermore, the lack of anodic resolution suggests oxidation of Ce(III) to Ce(IV) is not appreciable at the Au electrode in IL. Although the electrochemistry provides a preliminary assessment and assignment of the

voltammetric waves, further studies are required to verify both solutions species and surface species associated with the dissolution and electrochemical reduction of Ce species at the Au.

The background cyclic voltammetric response for a Pt electrode immersed in IL containing 80 mM is provided in **Figure 26(a)**. The voltammetry is characterized by the reduction of $H^+$ at negative potentials (wave I) and the oxidation of hydrogen (wave I′), respectively.[84] In addition, waves VII and VIII are also present, consistent with electrochemical results for Au. Previously the reactions assigned to waves VII and VIII included either the oxidative sorption/desorption of TFSI anion degradation products or the formation/reduction of metal oxide. Both assignments are again possible for the Pt electrode. However, the IV/IV' couple is also resolved for Pt which is indicative of water in the background solution.[81]

The current density associated with the Pt electrode immersed in IL containing 10 mM Ce is significantly higher when compared to the background, **Figure 26(b)**. Three distinct reduction processes I/II, III, IV, in the potential range between 0 and -1.25 V in the voltammetry can be identified for the Pt disc electrode in IL containing soluble Ce. The current density decreases reaching steady state after ~8 cycles, which is also consistent with the voltammetry observed for the Au electrode. Moreover, the magnitude change in current density associated with wave I/II is also greater than the decrease in current for waves III or IV at the Pt electrode, which agrees favorably with the results for Au. It is proposed that the voltammetric waves I/II, III, and IV are consistent with the sequential reduction of surface adsorbed Ce/TFSI complex and the sequential loss of the ligand from the reduction of the Ce species on the electrode surface. The process is more reversible and waves I′/II′, III′, and IV′ are more resolved at the Pt electrode when compared to Au. For example, the steady state voltammetry for reduction (cathode peak, pc) and oxidation (anodic peak, pa) waves I/II and I′/II′ provide values of $E_{pc}$ = -0.127 V and $E_{pa}$

= -0.093 V with peak splitting of $\Delta E_p$ = 0.034 V and current densities such that $I_{pc}/I_{pa'}$ = 1.26 for the Pt electrode. The voltammetric wave assignments are provided in **Table 5**.

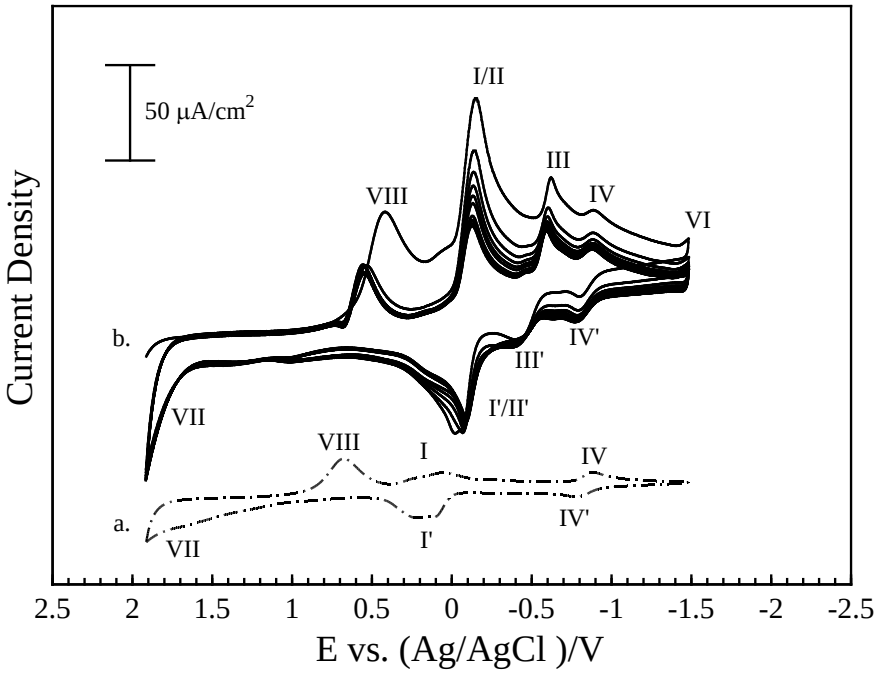


**Figure 26.** Cyclic voltammograms for **(a)** Pt disc electrode in $[Me_3N^nBu][TFSI]$ containing 80 mM HTFSI (dashed line), and **(b)** Pt disc electrode in $[Me_3N^nBu][TFSI]$ containing 80 mM HTFSI with 10 mM soluble Ce (solid line) from the direct dissolution. Scan rate = 50 mV/s.

A glassy carbon (GC) electrode was used to provide a comparison between the voltammetry at a non-metal electrode and metal electrodes (Au, Pt). The background voltammetry of a GC electrode immersed in IL containing 80 mM HTFSI is provided in **Figure 27(a)**. The voltammetry for GC shows one reduction wave (I) at -0.4 V that can be attributed to the reduction of proton and evolution of hydrogen.[81,84] Oxidation of TFSI at GC based on previous studies is unresolved suggesting that oxidation of TFSI is not appreciable.[81] The lack of anodic current associated with oxidation of the TFSI anion at GC is the primary reason the formation of metal oxides are suggested for the Au and Pt electrodes. However, the lack of

oxidation at GC electrodes does not preclude the possibility that the oxidation of TFSI and formation of the metal oxide occur simultaneously at Au and Pt.

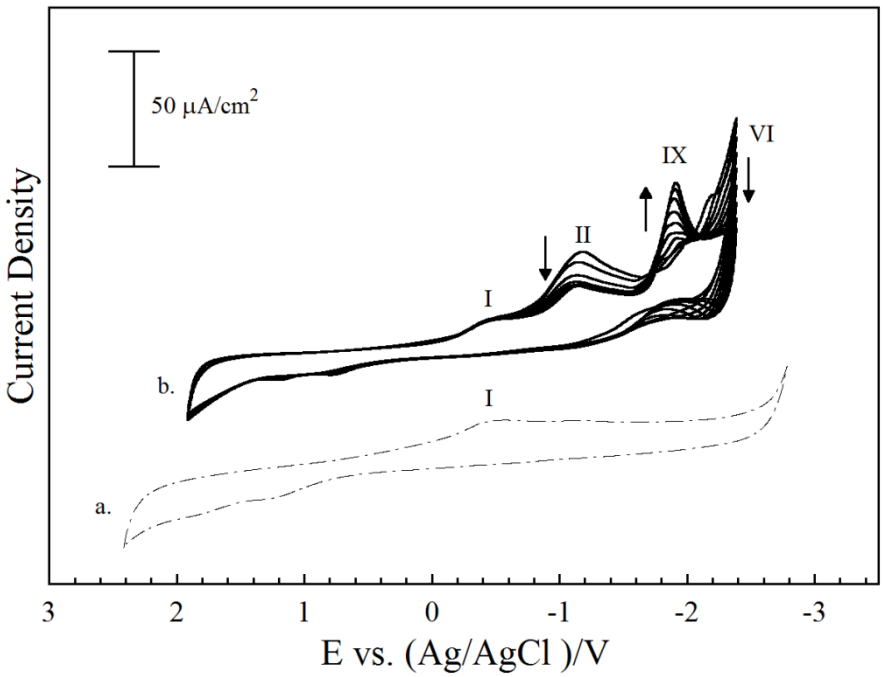


**Figure 27.** Cyclic voltammograms for **(a)** glassy carbon (GC) disc electrode in $[Me_3N^nBu][TFSI]$ containing 80 mM HTFSI (dashed line), and **(b)** GC disc in $[Me_3N^nBu][TFSI]$ containing 80 mM HTFSI with 10 mM soluble Ce (solid line). Scan rate = 50 mV/s.

The cyclic voltammetric response for a GC electrode immersed in IL containing 10 mM Ce is presented in **Figure 27(b)**. The reduction of proton at the GC electrode can be observed in both the background solution and IL containing soluble Ce (wave I). The reduction of Ce species (wave II) is clearly resolved from wave I in the voltammetry for the GC electrode. The voltammetry associated with wave II initially decreases reaching steady state after ~4 voltammetric scans. In contrast, a second reduction process emerges at -1.95 V (wave IX) for the GC electrode. The current associated with wave IX increases with each voltammetric cycle suggesting the surface deposition of Ce species occurs. Simultaneously, isosbestic points at -

1.78 V and -2.19 V emerge based on the reduced current density associated with waves II and VI. The voltammetry at the GC disc electrode is significantly different when compared to the voltammetry at either Au or Pt electrodes. The emergence of wave IX suggests that the deposition of Ce species occurs preferentially at existing nucleation sites rather than at the free GC surface. Finally, oxidative waves for the anodic scan are completely absent suggesting that the Ce deposits are resistant to subsequent oxidation and dissolution from the GC surface.

**Table 5.** Summary of the proposed reactions and peak assignments for Au, Pt, and glassy carbon (GC) electrodes in IL containing HTFSI and soluble Ce.

| Peak | Proposed Reactions |
|---|---|
| I | $H^+_{IL} + e^- \longrightarrow H_{ads}$ and,<br>$H_{ads} + H^+_{IL} + e^- \longrightarrow H_2$ |
| II | $H^+_{IL} + e^- \longrightarrow H_{ads}$ and,<br>$H_{ads} + H^+_{IL} + e^- \longrightarrow H_2$<br>$Ce(TFSI)_3 + e^- \longrightarrow Ce(TFSI)_{2,ads} + TFSI^-$ |
| III | $H^+_{IL} + e^- \longrightarrow H_{ads}$ and,<br>$H_{ads} + H^+_{IL} + e^- \longrightarrow H_2$<br>$Ce(TFSI)_{2,ads} + e^- \longrightarrow Ce(TFSI)_{ads} + TFSI^-$ |
| IV | $H_2O + e^- \longrightarrow \frac{1}{2} H_2 + OH^-$<br>$Ce(TFSI)_{ads} + e^- \longrightarrow Ce_{ads} + TFSI^-$ |
| VI | $Ce(TFSI)_3 + 3\,e^- \longrightarrow Ce_{ads} + 3\,TFSI^-$ |
| VII | Oxidation of the TFSI anion<br>$2\,Au + 3\,H_2O \longrightarrow Au_2O_3 + 6\,H^+ + 6\,e^-$<br>$Pt + 2\,H_2O \longrightarrow PtO_2 + 4\,H^+ + 4\,e^-$ |
| VIII | Reduction/desorption of TFSI products from VII<br>$Au_2O_3 + 6\,H^+ + 6\,e^- \longrightarrow 2\,Au + 3\,H_2O$<br>$PtO_2 + 4\,H^+ + 4\,e^- \longrightarrow Pt + 2\,H_2O$ |
| IX | $Ce(TFSI)_3 + 3\,e^- \longrightarrow Ce_{ads} + 3\,TFSI^-$ for GC |

4.6 Scanning Electron Microscopy and Energy Dispersive X-ray Spectroscopy (SEM/EDS) Analysis of Electrodeposits

The voltammetry alone does not allow the deposition of Ce species at Au, Pt, or GC to be verified. Therefore, the electrochemical deposition of Ce species at mica/Au electrodes was performed with the same electrochemical parameters utilized in **Figure 26**. The substrate was then rinsed with ethanol and SEM/EDS analysis was conducted, **Figure 28**. Surface deposits consistent with electrochemical deposition of Ce species on the Au surface are observed in the SEM image with variable thickness, **Figure 28(a)**. The variable thickness of deposits in the image suggests that the deposition can occur at either existing Ce nucleation sites or free Au surface. The bright areas in the SEM represent free Au surface without any observable Ce.

The EDS spectra provided in **Figure 28(b)** corresponds to the light Ce deposit. The corresponding bands for Ce are observed at 0.88, 4.84, 5.26, 5.62, 6.06 keV in the EDS spectra which confirm the deposition of Ce species on the Au electrode.[103] While the electrochemical deposition of cerium metal and oxide has been reported in molten salts[104] the electrochemical deposition of Ce species from IL at room temperature has not been previously reported. The EDS response shows characteristic energy bands for the Au surface. In addition, bands for sulfur, carbon, fluorine, and oxygen which can be attributed to the functional groups of the TFSI ligand are observed. The data suggests that the single wash with the ethanol did not eliminate all of the IL from the electrode surface.

The same chemical species associated with the deposition of Ce species and residual TFSI can be identified in the EDS response for thicker deposits in **Figure 28(c)**,**i**. However, the substrate was more thoroughly washed in an attempt to remove the residual IL from the electrode surface. There were no obvious changes in the SEM for the sample after more extensive

washing (not shown). The corresponding EDS response is provide in **Figure 28(c)**,**ii** for thick Ce deposits (no observable Au). The Ce bands in the spectrum are unchanged indicating that the deposits remain on the surface after extensive washing with ethanol. However, a significant decrease in the intensities of C, F, and S are observed, which is consistent with the loss of IL from the electrode surface. Finally, the band associated with the oxygen content increases after washing suggesting the IL may protect the Ce deposits from air oxidation. The data suggests that the deposition of Ce metal is achieved electrochemically and the formation of cerium oxide occurs through ex-situ chemical processes when exposed to air. These results are consistent with the previous studies for the deposition of Th metal, which formed thorium oxide through chemical processes.[15] The SEM/EDS results confirm that the surface deposition of Ce species is achieved electrochemically from IL solutions prepared from the direct dissolution of $Ce_2(CO_3)_3$.

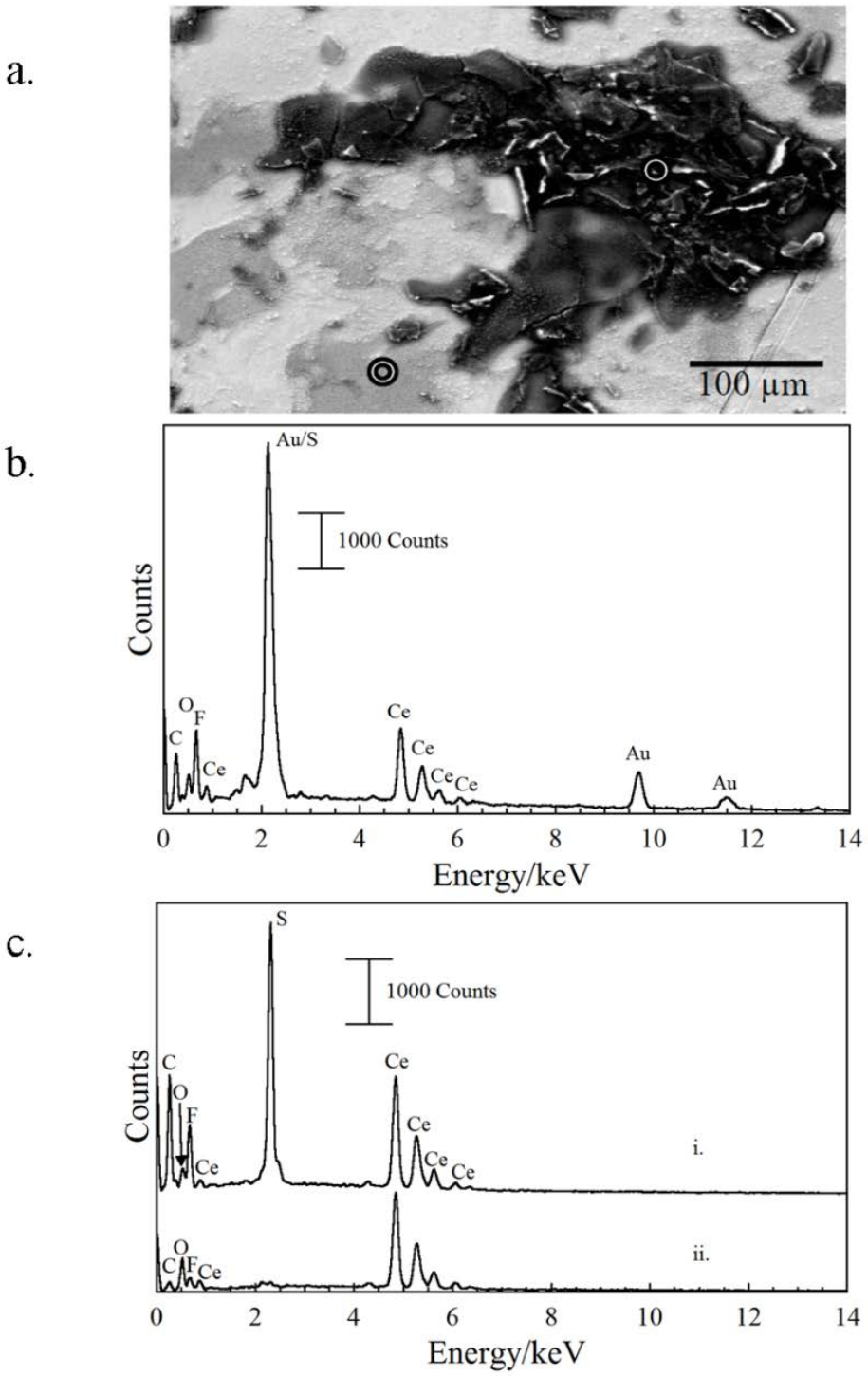


**Figure 28. (a)** The SEM image of a Ce species deposited on Au/mica electrode obtained from the cyclic voltammetry in $[Me_3N^nBu][TFSI]$ containing 80 mM HTFSI and 10 mM soluble Ce. **(b)** EDS spectra of the thin Ce deposits. **(c)i**. EDS of thicker Ce deposits lightly after a single washing with ethanol and **(c)ii.** after four additional washings with ethanol.

## 4.7 Conclusions

The direct dissolution of ($Ce_2(CO_3)_3 \cdot xH_2O$) into protic IL [$Me_3N^nBu$][TFSI] containing the conjugate acid, HTFSI, was demonstrated. The direct dissolution is achieved through the formation and decomposition of carbonic acid with subsequent degassing to remove $CO_2$ and water from the IL. This approach minimizes the inclusion of additional chemical species in the IL to promote coordination between soluble Ce and the TFSI ligand. Electronic transitions in the UV range are consistent with the formation of Ce/TFSI complexes and indicative of ligand-to-metal charge transfer complexes. Finally, changes in the absorbance intensities of IR vibrational bands associated with the sulfonyl oxygen are also indicative of the coordination between TFSI and soluble Ce.

Electrochemical analysis of soluble Ce in [$Me_3N^nBu$][TFSI] was performed at electrodes including Au, Pt, and GC. The multi-wave voltammetry observed for all three electrodes suggests that the deposition of Ce species proceeds through and reductive loss of TFSI at the electrode surface. The deposition of Ce species at all three electrodes occurs at potentials more positive than the reduction potential in aqueous solutions. The data presented suggests that the IL environment contributes to more favorable electrochemical deposition of Ce species when compared to aqueous solutions. The deposition of Ce species at Au was visualized using SEM and confirmed with EDS analysis. The results for $Ce_2(CO_3)_3$ suggests that the protic IL can be used to increase solubility of other trivalent lanthanide carbonate species through direct dissolution. Additional studies are needed to confirm the soluble Ce species produced from the direct dissolution of $Ce_2(CO_3)_3$ in IL using HTFSI. Finally, bulk electrolysis of Ce from IL should be performed to provide bulk deposits for more thorough examination to determine if the initial deposit is Ce metal or oxide.

# Chapter 5: Dissolution of Uranyl Carbonate and Uranium Oxide in Ionic Liquid and Electrochemical Studies

This chapter evaluates the introduction of actinide species into the IL through direct dissolution of uranyl carbonate, $UO_2CO_3$, and uranium oxide, $U_3O_8$. Direct dissolution of uranyl carbonate was performed both in water and in IL for comparison, as well as with and without the addition of the conjugate acid HTFSI. The dissolution of uranium oxide, $U_3O_8$, does not effectively dissolve into IL even in the presence of the HTFSI acid. A method for direct dissolution of the oxide, however, was developed using oxidizing gas provided by an ozone generator. The soluble species in the IL was analyzed using UV-Vis spectroscopy and corresponds to uranyl ($UO_2^{2+}$). The reduction/oxidation of soluble uranyl in IL is examined at Au electrodes. Scanning electron microscopy (SEM) and energy dispersive x-ray spectroscopy (EDS) confirm the recovery of uranium as an oxide species.

## 5.1 Introduction

The solubility, coordination and speciation of f-elements in ILs has been the focus of numerous studies because purely ionic systems have unique physical properties that can be exploited in comparison to aqueous, organic, or molten salt systems.[105] For example, ILs can be used to evaluate the electrochemical properties of f-elements, while minimizing the impact of side reactions typically encountered in aqueous environments.[105] Moreover, the physical properties of the cation/anion pair of the IL provide a significantly larger potential window when compared to water, encompassing the thermodynamic potentials required for the reduction of f-elements to metal.[34,106] The choice of the cation is critical because reduction of the species can

occur at potentials that preclude the electrochemical reduction of actinides to metal.[107,108] The n-trimethyl-n-butylammonium cation provides relatively low viscosity and melting point when combined with the TFSI anion and it is electrochemically stable at negative potentials that encompass the reduction of actinide species.[105- 107] ILs also have negligible vapor pressure and high thermal stability in contrast to common organic solvents. Finally, ILs do not require the elevated temperatures thereby reducing the energy requirements in comparison to the associated molten salt systems.[109,110]

The electrochemical study of f-elements in IL can be complicated by the inherent low solubility of f-elements in purely ionic solvents. Solvent extraction from aqueous solutions[7,41] has been utilized to introduce f-element species into ILs. Extraction is typically achieved by first dissolving the f-elements in aqueous acid solutions followed by two-phase extraction of the soluble species into the IL using complexing agents.[8,9] The extraction can be complicated by the crossover of neutral water and ionic species at the phase boundary increasing possible contaminants in the IL.[41] Crossover effects can be minimized provided the aqueous solution composition is precisely controlled. More recently, species such as Pu(IV), Th(IV), and trivalent lanthanides have been extracted into IL without the need of additional complexing agent.[46,47] The results suggest that extraction may be an effective way of pre-concentrating some f-elements in IL.

The direct dissolution of actinide and lanthanide species has also been achieved using preformed complexes with ligands common to the IL. For example, complexes of $[Th(TFSI)_4(HTFSI)]\cdot 2H_2O$ where the TFSI is the bis(trifluoroethanesulfonyl)amide ion ($N(SO_2CF_3)_2$)[15] and $Ln(TFSI)_3(H_2O)_3$ (Ln = La(III), Sm(III), and Eu(III))[16] have been successfully prepared and dissolved directly into the IL n-trimethyl-n-butylammonium

bis(trifluoromethansulfonyl)amide, $[Me_3N^nBu][TFSI]$. In addition, the dissolution of $UO_2(TFSI)_2$ and $UO_2(TFSI)_2 \cdot xH_2O$ has been achieved in a variety of IL solutions containing the TFSI anion.[111,112] However, synthesis in aqueous solution can be influenced by water coordination minimizing possible interactions with weakly coordinating ligands such as TFSI prior to dissolution in IL.[113,114] For example, the absorbance of $UO_2(TFSI)_2 \cdot xH_2O$ when dissolved into various ILs is consistent with hydrated uranyl ion $[UO_2(H_2O)_5]^{2+}$ suggesting that the TFSI ion is not the primary coordinated species when the complex is prepared from aqueous solution.[111-114] The question remains if water coordination with uranyl cation is inhibited during the direct dissolution of $UO_2CO_3$ or $U_3O_8$ in IL containing water when compared to the $UO_2(TFSI)_2 \cdot xH_2O$ complex produced in aqueous synthesis.

Alternatively, "task specific" ILs that contain acid functionalized cations have been used to dissolve metal species into ILs.[17,18] The betaine cation is the zwitterion 1-carboxy-N,N,N-trimethylmethaneaminium hydroxide where the carboxylate moiety acts as the coordinating group for metal solubilization.[17,18] Similar carboxylic functionalized cations have been produced to dissolve metal oxides where they can be reacted stoichiometrically with the protonated cations.[19] However, the presence of water also plays a role with increased solubility in "wet" IL which may be due to the ability of the hydrophobic IL to interact with the metal oxide surface.[19] Using these methods many trivalent lanthanides (e.g. $Sm_2O_3$, $Eu_2O_3$, and $Nd_2O_3$) and $UO_3$ were dissolved directly into the IL without addition of secondary acid species. Although the carboxylic functional group plays an important role in the formation of the uranyl complex during the dissolution process, the role of water is equally important in providing solvated protons for the reaction.[19,58]

The previous studies suggest that the use of acid functional groups and water may be beneficial in the dissolution and solubility of lanthanide and actinide species in ILs. However, the direct dissolution of f-element species in the ILs using secondary acid species common to the IL has not been extensively studied. The dissolution of $UO_2CO_3$ using HTFSI can be explored through the formation of carbonic acid intermediate and the production of water and $CO_2$ as byproducts:

$$UO_2(CO_3) + 2\,HTFSI \rightleftharpoons UO_2^{2+} + 2\,TFSI^- + H_2CO_3 \longrightarrow H_2O\uparrow + CO_2\uparrow \quad (\textbf{Eq. 21})$$

Previously, bis(trifluoromethanesulfonyl)amide (HTFSI) has been utilized to produce protic ILs with a variety of different cations.[20] The evolution of hydrogen in IL solutions has been demonstrated suggesting that the protons within the IL are partially dissociated from HTFSI.[20] In addition, the acidity of ILs containing HTFSI or carboxylic acids was evaluated using various protic indicators.[22,80] Both studies suggest that proton dissociation from the acid is diminished in IL when compared to aqueous solution environments, reducing the overall acid strength. Therefore the role of water within the IL may be important in increasing the dissociation of protons from HTFSI which will likely influence the direct dissolution of f-elements in ILs.[20,22,80] In addition, the role of water has been examined in the formation and reduction of gold oxide in IL solutions containing water without additional acid. The data suggests that the addition of water provides sufficient proton to the IL such that the oxidation/reduction of Au can be resolved electrochemically, **Equation 4** (Chapter 1).[75]

The direct dissolution of $UO_2CO_3$(s) into IL using either carboxyl functionalized cations or through the addition of HTFSI has not been extensively studied. Moreover, interfacing

common aqueous species such as $UO_2CO_3$ through the direct dissolution into IL may be useful in evaluating species that normally interact in natural environments. A more detailed understanding of the dissolution of $UO_2CO_3$ and the speciation and electrochemical behavior of soluble species in IL, $[Me_3N^nBu][TFSI]$, may also be useful in evaluating the use of ILs for more common uranium fission products. For example, recent studies have evaluated the electrolytic dissolution of simulated fuels in carbonate solutions through the formation of $UO_2CO_3$.[115,116] The uranyl carbonate could be an important component of some recycling schemes, where $UO_2CO_3$ is precipitated to achieve separation of the uranyl ion. The subsequent dissolution of $UO_2CO_3$ into IL solutions may therefore be relevant in the recovery of the uranyl species. Finally, $UO_2^{2+}$ is a common species encountered in typical separation schemes and an understanding of the chemical and electrochemical properties of the species in ILs is important regardless of the initial species used in the dissolution.

This work evaluates the direct dissolution of $UO_2CO_3$ in pristine IL containing residual water and "wet" $[Me_3N^nBu][TFSI]$ containing HTFSI with added water at room temperature. The soluble species from the dissolution process are characterized using liquid scintillation counting and UV-Vis spectroscopy. The properties of the carbonate ligand are specifically exploited to increase the solubility of the f-element species and provide a pathway for incorporating the actinide species into the IL. The soluble uranium species provide insight into the dissolution mechanism of $UO_2CO_3$ and electrochemical measurements are used to probe the oxidation/reduction properties of the soluble species. Electrochemical methods are also utilized in the potential dependent deposition of uranium species from the IL and SEM/EDS analyses are used to examine and confirm the deposition of the uranium species at an Au electrode surface.

Investigation of the dissolution of uranium oxide and electrochemical nature of soluble uranium species in IL is also of interest from a used fuel recycling standpoint. Therefore, the direct dissolution of $U_3O_8$ into the IL, $[Me_3N^nBu][TFSI]$, is presented and a method was developed to achieve successful dissolution without using an aqueous anion complexation route. Unlike the more soluble $UO_2CO_3$, the oxide required an oxidizing gas to achieve direct dissolution into the IL. The soluble species was characterized using UV-Vis spectroscopy. Cyclic voltammetry and electrodeposition were performed on samples of the soluble uranyl following dissolution, with and without the addition of HTFSI. Deposits obtained on Au foil were analyzed by SEM/EDS to confirm deposition of uranium oxide.

## 5.2 Methods and Materials

### 5.2.1 Chemicals and Solutions

The IL, n-trimethyl-n-butylammonium bis(trifluoromethanesulfonyl)imide, $[Me_3N^nBu][TFSI]$ (99.5%, Solvionic), and bis(trifluoromethanesulfonyl)imide [HTFSI] (>95%, Fluka) were used as receive. Uranyl carbonate ($UO_2CO_3$) and uranium oxide ($U_3O_8$) were synthesized, as described in Chapter 2.

### 5.2.2 Dissolution into Ionic Liquid

#### 5.2.2.1 Uranyl Carbonate

The dissolution of $UO_2CO_3$ without the addition of HTFSI or water was initialized after placing 0.3 g of finely ground uranyl carbonate containing $^{233}U$ along with 39.3 mL of $[Me_3N^nBu][TFSI]$ in a 50 mL centrifuge tube. The water content of the pristine IL was determined using Karl Fischer titration, 0.285 % by weight. Constant stirring of the reaction vessel contents was executed using a spin vane with a continuous argon gas purge. The

centrifuge tube was disconnected from the gas and centrifuged for 10 minutes at given time intervals prior to measurement. An aliquot was removed and saved for analysis using both liquid scintillation counting and UV-Vis spectroscopy over the course of 80 days.

The direct dissolution was also examined by placing 0.0251 g of $UO_2CO_3$ in 15 mL of $[Me_3N^nBu][TFSI]$ containing 0.1 M HTFSI, producing 5 mM soluble $UO_2^{2+}$ in IL. The dissolution of $UO_2CO_3$ sample was completed within a few hours without the addition of water. Finally, a set of 50 mM $UO_2CO_3$ samples containing 0.2475 g $UO_2CO_3$ in 15 mL of deionized water or IL with 0.5 M HTFSI were prepared. The uranyl carbonate completely dissolved in the aqueous solution within 10 minutes of mixing. In contrast, the dissolution of $UO_2CO_3$ in the IL did not occur after 24 hours. To facilitate the dissolution, 2 mL of 0.5 M HTFSI in $H_2O$ was added to the sample to enhance the deprotonation of the acid in the IL and increase solubility.[19,58] The sample was sonicated resulting in the complete dissolution of the solid and then centrifuged to assist the separation of the aqueous and IL phases. The sample was purged with argon to eliminate the water phase until only the IL was visible. The resulting solution was measured using Karl Fischer titration which provided a measure of the water content after purging the IL, 1.28 wt %. For comparison, the IL containing 0.5 M HTFSI prior to dissolution was 0.298 wt % $H_2O$. Finally, the water content for the 5 mM soluble $UO_2^{2+}$ in IL solution obtained following the direct dissolution of $UO_2CO_3$ without the addition of water to facilitate dissolution was 0.524 wt %.

#### 5.2.2.2 Uranium Oxide ($U_3O_8$)

Initially the dissolution of $U_3O_8$ into IL was attempted with HTFSI, similarly to the $UO_2CO_3$ dissolution, unsuccessfully. The original dissolution sample was 45 mg $U_3O_8$ (nat) into $[Me_3N^nBu][TFSI]$ containing 3.27 M HTFSI. However, stirring and purging with argon for

weeks resulted in no apparent change. Eventually, oxidizing gas was tried using an ozone generator supplied with air. The oxide then dissolved into the IL within 72 hours. Subsequent dissolutions have followed a similar procedure using the oxidizing gas. All studies were performed at room temperature (~24°C).

Dissolution using air feed gas to the ozone generator was also tested comparing dry IL and water-saturated IL. The dried IL was prepared by adding 10 g of molecular sieves (type 3 Å) to ~30 mL $[Me_3N^nBu][TFSI]$. Water-saturated IL was prepared by contacting ~ 30 mL $[Me_3N^nBu][TFSI]$ with 15 mL of ultrapure water. The phases separate overnight and the water-saturated IL was kept in contact with the aqueous layer until use in experiments. The use of $U_3O_8$ which was prepared with trace $^{233}U$ allowed for monitoring of the dissolution by monitoring the activity in solution using LSC. The samples consisted of: 0.1414 g $U_3O_8$ in 28.21 g dried $[Me_3N^nBu][TFSI]$, and 0.1414 g $U_3O_8$ in 28.20 g "wet" $[Me_3N^nBu][TFSI]$. The dissolution was attempted using other gases as well. That dissolution sample consisted of 0.1457 g $U_3O_8$ in 28.25 g of dried $[Me_3N^nBu][TFSI]$.

Gases were passed through an Ozone Solutions OZV-8 generator at a flow rate ~1 L/min and at generator level 5. Solutions were stirred continuously. Various gases were used including: breathing grade air, $O_2$, $N_2$, and $N_2O$ supplied from Praxair. All gases flowed through a drierite column to help ensure dry gas passed through the ozone generator and into the sample. However, in some cases the ozone generator (plasma) was not turned on. This was done intentionally to study and compare whether dissolution occurred from the neat gas versus a product of the gas after passing through the plasma. Based upon previous dissolution results under similar conditions, the dissolution was monitored for a period of 72 hours.

5.2.3 Liquid Scintillation Counting

Portions of the samples were centrifuged at various times to collect an aliquot of the IL for determination of the progress of dissolution of $U_3O_8$ into the IL. Aliquots (~ 100 μL) of the dissolution samples were massed gravimetrically into prepared liquid scintillation vial containing 10 mL Ultima Gold scintillation cocktail. The viscosity of the IL does not allow for accurate and precise micropipetting necessitated determining the aliquot gravimetrically. The vials were counted on a Tricarb 3100 liquid scintillation counter. Each sample was counted in triplicate and the average counts per minute (cpm). The calibration set previously made from the same synthesized $U_3O_8$ with trace $^{233}U$ and was counted along with the samples. LSC counts for the "C" region were used to represent the dissolution progress of $U_3O_8$ into the IL and the LSC counts were background corrected to an IL in LSC blank and normalized to the mass of the sample aliquot added to the 10 mL scintillation cocktail.

5.2.4 Karl Fischer Titration

Karl Fischer titrations of the IL were performed using a Mettler Toledo DL-32 titrator to determine the water content. The instrument was calibrated using a HYDRANAL water standard 1.0 ($H_2O$ 1.011 ± 0.003 mg/g) prior to the analysis of IL samples. The instrument was operated with 100 mL of the HYDRANAL analyte Coulomat A and 5 mL HYDRANAL catholyte Coloumat CG (Fluka), respectively.

5.2.5 UV-Visible Spectroscopy

UV-Vis Spectra were collected using a dual beam Cary 6000 UV-Vis-Near IR spectrophotometer using quartz cuvettes under ambient conditions in the spectral range between 200 – 800 nm. All UV-Vis spectra were collected versus a suitable baseline containing IL with or without the addition of HTFSI, as appropriate. All solutions containing soluble $UO_2CO_3$ were

purged with Ar to facilitate decomposition of any carbonic acid and reduction of residual $CO_2$ and water prior to measurement.

5.2.6 Electrochemical Apparatus and Conditions

All electrochemical measurements were performed using a CH Instruments 760 biopotentiostat with included software. The experiments were performed in a one-compartment, three-electrode cell after Ar degassing. A Pt sheet counter electrode was used with an immersed area exceeding the working electrode by a factor of two. A 2 mm diameter Au disc electrode ($3.14 \times 10^{-2}$ $cm^2$), 2 mm diameter Pt disc electrode ($3.14 \times 10^{-2}$ $cm^2$), and a 3 mm diameter glassy carbon disc (area = $7.07 \times 10^{-2}$ $cm^2$) were utilized as working electrodes for the electrochemical measurements. An Au foil (99.95% 0.25 mm thick) was used to obtain deposits and to provide a suitable flat substrate for SEM and EDS analysis. The reference electrode was prepared according to literature[65] and consisted of an Ag wire in contact with 0.1 M $Ag^+$ in the IL with a Vycor™ frit acting as the double junction. The reference electrode was standardized with respect to a $[Me_3N^nBu][TFSI]$ solution containing 4 mM ferrocene providing an offset potential of + 0.416 V vs. Ag/AgCl. All cyclic voltammograms are referenced versus Ag/AgCl (3 M KCl) based on the Ag/Ag+ electrode and the $Fc/Fc^+$ redox couple.

5.2.7 Scanning Electron Microscopy and Energy Dispersive X-ray Emission Spectroscopy Analysis (SEM/EDS)

The SEM/EDS measurements were collected using a JEOL-5610 scanning electron microscope equipped with a secondary electron and backscatter electron detectors with elemental analysis capability using EDS. The electrode surface was rinsed with ethanol and dried under vacuum prior to analysis.

5.3 Direct Dissolution into Ionic Liquid

5.3.1 Uranyl Carbonate

The possible dissolution mechanism for $UO_2CO_3$ and the complexation of soluble $UO_2^{2+}$ with TFSI is provided in **Figure 29**. The solubility in the IL should be directly influenced by the formation and decomposition of carbonic acid in the IL. In addition, TFSI complexation with soluble uranyl ion would be directly linked to dissociative loss of the carbonate species. The mechanism suggests that the availability of protons in solvent systems including IL and water will directly influence the dissolution of $UO_2CO_3$ and the ultimate solubility of $UO_2^{2+}$.

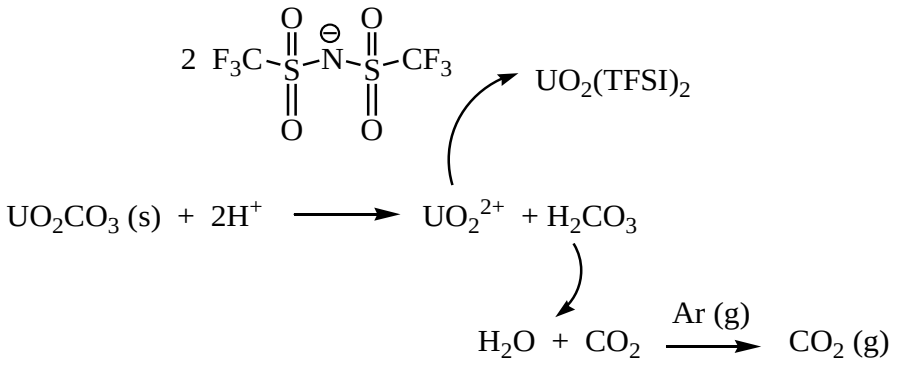


**Figure 29.** Possible dissolution mechanism for $UO_2CO_3$ in $[Me_3N^nBu][TFSI]$

The dissolution of $UO_2CO_3$ in the IL, $[Me_3N^nBu][TFSI]$, without added water or acid was initiated and evaluated daily for one week with no measurable change in the activity in solution according to the LSC. The measurement was the repeated after initiating degassing with dry argon and the liquid scintillation measurements for the dissolution of $UO_2CO_3$ in IL as a function of time is provided in **Figure 30**. The data indicates that the dissolution of $UO_2CO_3$ occurs within two days (2.5 μM) after the Ar degassing is initiated. It is clear from the plot that the dissolution of $UO_2CO_3$ in IL is relatively slow with the maximum concentration of ~160 μM

soluble $UO_2^{2+}$ reached after approximately 40 days. The mechanism for dissolution suggests that the purging can be used to facilitate the decomposition of $H_2CO_3$ and removal of water and carbon dioxide produced in the process. The dissolution process is likely inhibited by the lack of proton available in the pristine IL which minimizes the solubility of $UO_2CO_3$. The data also suggests that the residual water in the IL (0.285 wt %) may play a role in the dissolution of $UO_2CO_3$ providing sufficient proton concentration to initiate the process. Therefore, the proposed mechanism was evaluated for the dissolution of $UO_2CO_3$ containing the conjugate acid HTFSI dissolved in the IL $[Me_3N^nBu][TFSI]$. The goal was to increase the proton concentration and the ultimate solubility of $UO_2CO_3$ without introducing species other than TFSI that may coordinate with the soluble uranyl ion.

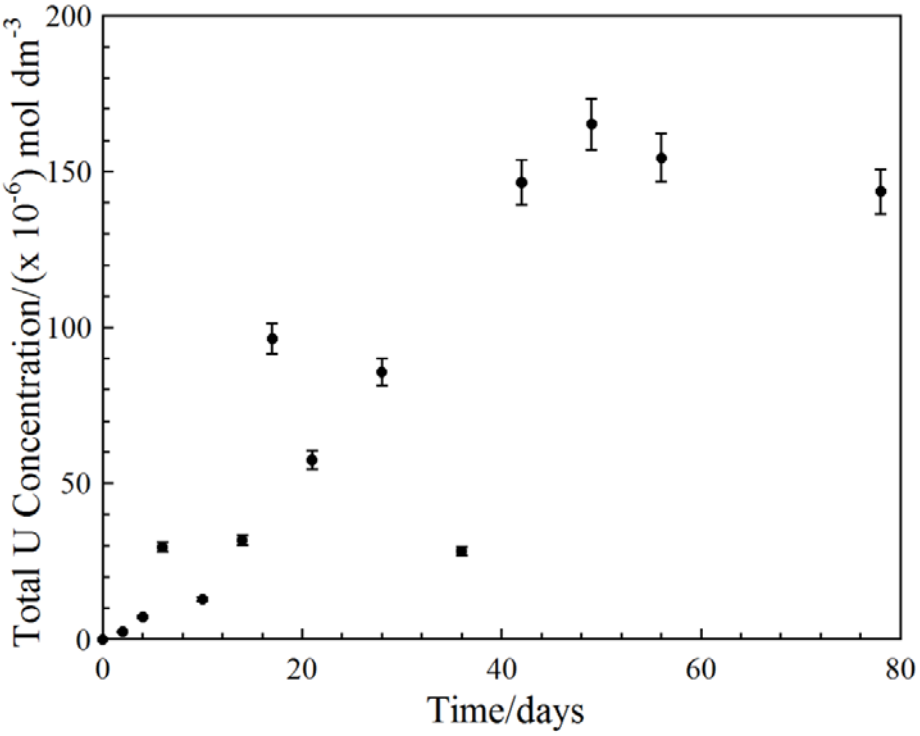


**Figure 30.** Total soluble U content from dissolution of 0.3 g $UO_2CO_3$ in 39.3 mL $[Me_3N^nBu][TFSI]$ as a function of Ar degassing time. Concentration was determined based on liquid scintillation counting of $^{233}U$ in the solid.[117]

5.3.2 Uranium Oxide ($U_3O_8$)

The dissolution of uranium oxide, $U_3O_8$, into IL under conditions used previously for $UO_2CO_3$ (i.e. water and acid, 3.27 M HTFSI) was not successful. $U_3O_8$ is comprised of a mixture of $U^{4+}$ and $U^{6+}$ and the axial oxygens in the oxide are bound more strongly than the carbonate group to the uranium. Traditional reprocessing such as PUREX involves dissolution using highly concentrated nitric acid and results in an aqueous uranyl ($UO_2^{2+}$) species. In an effort to avoid a two phase system, adding an aqueous acid to the IL was not ideal. Instead, utilizing an oxidizing gas such as ozone was tested using an ozone generator with air feed gas. Within 24 hours of bubbling the $U_3O_8$ sample in IL, which also contained 3.27 M HTFSI, the solid was nearly completely dissolved. The solution appeared a characteristic bright yellow consistent with uranyl. Pictures characterizing the dissolution process of $U_3O_8$ into the IL are presented below in **Figure 31**.

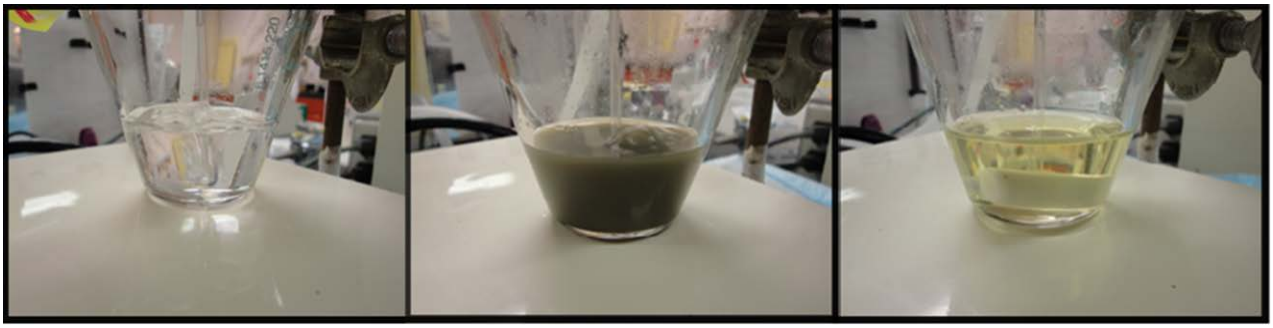

**Figure 31.** The IL before (left), during (middle), and after (right) dissolution of $U_3O_8$

Further studies indicated that dissolution of $U_3O_8$ can occur in dry $[Me_3N^nBu][TFSI]$ once exposed to an oxidizing gas without the conjugate HTFSI acid. However, to determine whether there could be an influence in the kinetics of dissolutions provided by the inclusion of water a study was performed to observe the rate of dissolution under the same conditions (air

feed gas to ozone generator, flow rate of ~ 1 L/min, ozone generator level 5) into a dry IL and water-saturated IL. **Figure 32** compares the rates of the dissolution of $U_3O_8$, synthesized with trace $^{233}U$, under the same sample conditions and experimental parameters by monitoring the activity by LSC. The dissolution in the water-saturated IL is initially somewhat faster, but after 60 hours as the dissolution is approaching the completion there is not much of an overall difference in the time required. The dissolution into dry $[Me_3N^nBu][TFSI]$ was completed in 120 hours of gas bubbling, while the dissolution into the water-saturated $[Me_3N^nBu][TFSI]$ was completed in 140 hours. Dissolution was determined to be completed by not observing any undissolved particles and the IL did not appear cloudy.

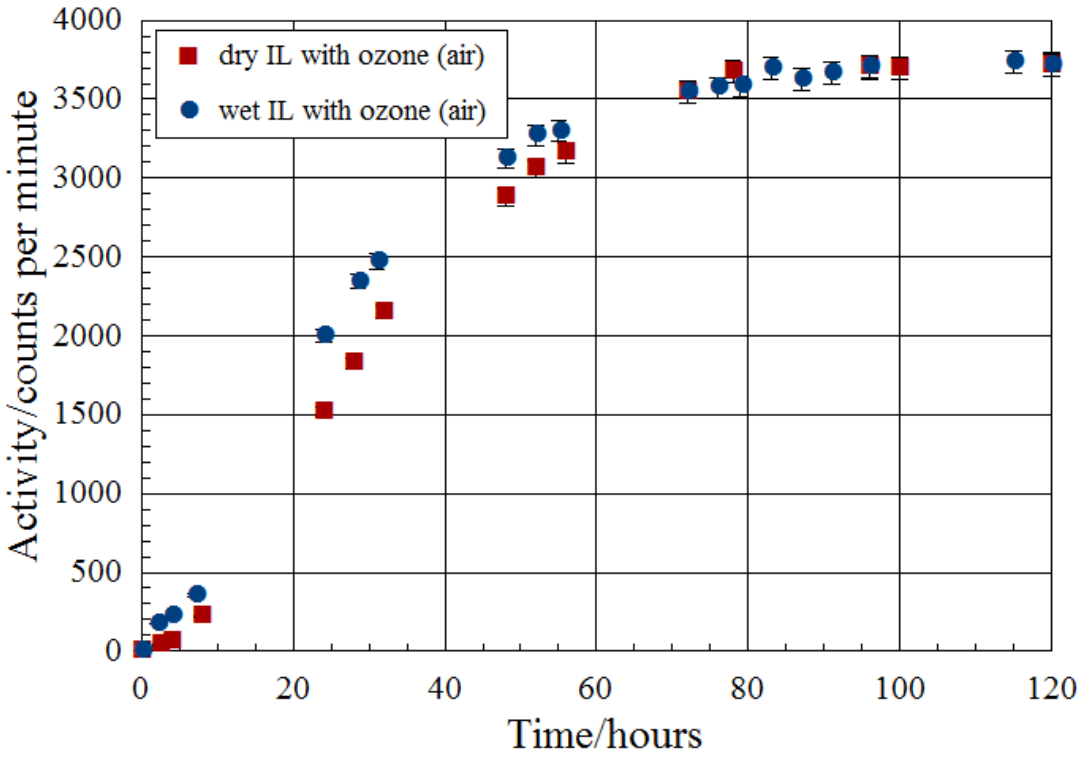


**Figure 32**. Rate of $U_3O_8$ dissolution into initially dry and water-saturated $[Me_3N^nBu][TFSI]$ with the assistance of oxidizing gas (air feed gas, flow rate 1 L/min, ozone generator level 5).

Karl Fischer titration was performed on portions of the starting dry and water-saturated $[Me_3N^nBu][TFSI]$ and completed dissolution samples, **Table 6**. The molecular sieves used to dry the IL significantly reduce the water content (6.2 ± 2.7 ppm) and the water-saturated sample was similar to previously observed values for this IL (1.362 ± 0.012 wt %, or 13,620 ± 120 ppm). After dissolution both samples had similar water content of around 2000 ppm $H_2O$. This isn't surprising since water is expected to be a possible side product of the dissolution, but the continuous bubbling with the gas will keep the water content much lower than saturation. The water content of the initially water-saturated IL dissolution sample is a bit lower and this is likely due to the slightly longer bubbling time of 140 hrs.

**Table 6.** Karl Fischer analysis of the water content of the dry and water-saturated $[Me_3N^nBu][TFSI]$ before and after dissolution of $U_3O_8$ into the IL with oxidizing gas.

| **$[Me_3N^nBu][TFSI]$ dried with sieves** | | | |
|---|---|---|---|
| Sample added for analysis (g) | 0.7557 | 0.6700 | 0.9797 |
| $H_2O$ Result (ppm) | 5.84 | 9.11 | 3.72 |
| Average and St. Dev. | **6.2 ± 2.7 ppm $H_2O$** | | |
| **$[Me_3N^nBu][TFSI]$ water-saturated** | | | |
| Sample added for analysis (g) | 1.0166 | 0.8061 | 1.0320 |
| $H_2O$ Result (wt %) | 1.3549 | 1.3544 | 1.376 |
| Average and St. Dev. | **1.362 ± 0.012 % $H_2O$** | | |
| **$U_3O_8$ dissolution into dry $[Me_3N^nBu][TFSI]$** | | | |
| Sample added for analysis (g) | 1.0197 | 0.4949 | 0.7444 |
| $H_2O$ Result (wt %) | 0.2305 | 0.2417 | 0.2225 |
| Average and St. Dev. | **0.232 ± 0.010 % $H_2O$** | | |
| **$U_3O_8$ dissolution into water-saturated $[Me_3N^nBu][TFSI]$** | | | |
| Sample added for analysis (g) | 1.0070 | 0.5248 | 0.7606 |
| $H_2O$ Result (wt %) | 0.1844 | 0.1712 | 0.1728 |
| Average and St. Dev. | **0.176 ± 0.007 % $H_2O$** | | |

Further dissolutions studies of the $U_3O_8$ into dry IL were conducted to investigate what gas species may be responsible for the dissolution. Initially, ozone was thought to be the oxidizing gas species responsible for the dissolution. However, it was discovered that changing the feed gas of the ozone generator from air to $O_2$ (which would increase the percentage of produced ozone by about double) did not result in dissolution of the $U_3O_8$ into the IL.

The air gas is comprised of nitrogen (80.5 – 76.5%), oxygen (19.5 – 23.5 %), and a small amount of $CO_2$ (<1000 ppm), and as it travels through the plasma within the ozone generator there may be a number of chemical species formed including radicals and recombinations. These reactions produce other species such as nitrous oxide ($N_2O_)$, nitric oxide ($NO_2$), NO, and their respective radicals. The efficiencies of producing these species from the ozone generator and these conditions are not known.

To evaluate possible dissolution mechanisms, dissolution studies continued by bubbling with each of the main components of air gas (oxygen, nitrogen) and the possible product of nitrous oxide through a sample of IL containing $U_3O_8$ and monitored for a period up to 72 hours. Initially, the gases were used as is, however, none of these gases resulted in dissolution of $U_3O_8$ into IL Additionally, when the gases were used as feed gas with the ozone generator turned on there still was no evidence of dissolution within 72 hours. A comparison of the gasses attempted for dissolution of $U_3O_8$ into dry $[Me_3N^nBu][TFSI]$ in conjunction with an ozone generator is featured in **Figure 33**. The only successful dissolution occurred using air as the ozone generator feed gas. Significant dissolution occurred within 72 hours and for the sample conditions studied completed within about 120 hours.

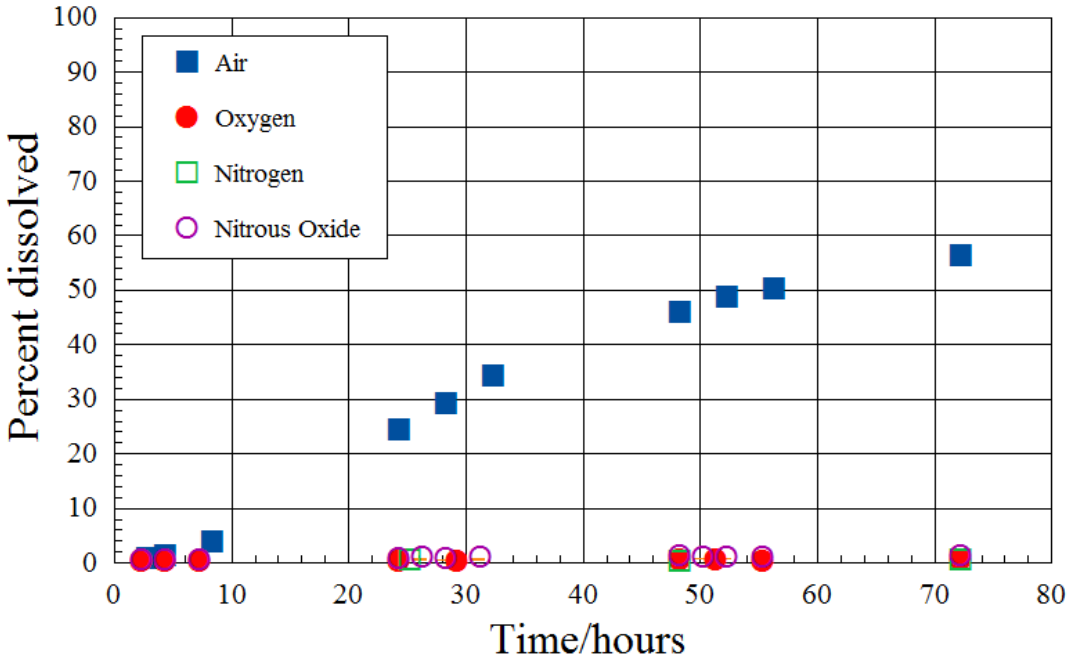


**Figure 33.** Comparison of the dissolution of $U_3O_8$ into dry $Me_3N^nBuTFSI$ attempted with different feed gases for 72 hrs: Air, $O_2$, $N_2$, $N_2O$. (flow rate 1 L/min, ozone generator level 5)

It is worth noting that nitrous oxide as the feed gas to the ozone generator did not seem to produce any ozone from the plasma inside since the discharged gas did not yield a dark blue color when exposed to the KI-starch indicator solution. Considering the results thus far, ozone alone may not be the active gas or only active oxidizing gas which results in the successful dissolution. One final dissolution attempt was performed using the simultaneous bubbling of ozone (produced by the ozone generator with oxygen feed gas) and nitrous oxide. However, once again there was no apparent dissolution within the 72 hours monitoring period.

The dissolution data thus far has not resulted in a known mechanism for the dissolution of the uranium oxide into IL using the oxidizing gas produced from air through an ozone generator. However, the data does suggest that ozone may be working in coordination with another oxidizing gas or radical produced by the plasma. Gelis et. al. report an interesting

reaction mechanism for the dissolution of cerium oxide in $HNO_3$ using ozone.[118] The authors suggest ozone reacts with the cerium to form a cerium oxyradical which goes on to interact with proton and forms the oxidized cerium and a hydroxyl radical. The hydroxyl radical can also interact with the soluble Ce(III) and oxidize to Ce(IV) and produce a hydroxyl anion. Finally, the hydroxyl anion can combine with proton to form water. The reactions are presented below.[118]

$$Ce^{3+} + O_3 \rightarrow CeO^{\cdot 3+} + O_2 \quad \textbf{(Eq. 22)}$$

$$CeO^{\cdot 3+} + H^+ \rightarrow Ce^{4+} + {}^{\cdot}OH \quad \textbf{(Eq. 23)}$$

$$Ce^{3+} + {}^{\cdot}OH \rightarrow Ce^{4+} + OH^- \quad \textbf{(Eq. 24)}$$

$$OH^- + H^+ \rightarrow H_2O \quad \textbf{(Eq. 25)}$$

Utilizing the same theory, a similar set of reactions can be proposed for the dissolution of the $U_3O_8$ into the IL using ozone. The proposed possible reactions are presented below.

$$U_3O_8 + O_3 \rightarrow U_3O_9^{\cdot} + O_2 \quad \textbf{(Eq. 26)}$$

$$U_3O_9^{\cdot} + 6\ H^+ \rightarrow 3\ UO_2^{2+} + 3\ H_2O \quad \textbf{(Eq. 27)}$$

Alternatively, the active dissolution gas may not be ozone but could be a product from the air in the plasma, such as NO. A set of similar reactions are presented below.

$$2\ U_3O_8 + 2\ NO \rightarrow 2\ U_3O_9^{\cdot} + N_2 \quad \textbf{(Eq. 28)}$$

$$U_3O_9^{\cdot} + 6\ H^+ \rightarrow 3\ UO_2^{2+} + 3\ H_2O \quad \textbf{(Eq. 29)}$$

## 5.4 UV-Visible spectroscopy Results

### 5.4.1 Uranyl Carbonate Dissolved in Ionic Liquid

For comparison, the dissolution of $UO_2CO_3$ (50 mM) in both IL and water containing 0.5 M HTFSI was evaluated using UV-Vis spectroscopy, **Figure 34**. The background UV-Vis spectra of 0.5 M HTFSI in water and IL are also provided for reference to the absorbance bands associated with the dissolution of $UO_2CO_3$ in both solvent systems. The UV-Vis absorbance associated with HTFSI dissolved in water is characterized by a single band at ~255 nm with relatively low absorbance when compared to the absorbance band centered at 280 nm for the acid species in IL. The wavelengths for the absorbance maximum for each solvent system highlight the difference in dissociation of protons from HTFSI for water and the higher concentration of the TFSI anion in the IL. Moreover, strong absorbance is observed for the IL solution containing HTFSI between 200 – 240 nm when compared to the acid dissolved in water.

The absorbance spectra for the direct dissolution of the solid $UO_2CO_3$ (~50 mM) in water and the IL are also provided in **Figure 34**. The complete dissolution of $UO_2CO_3$ in water containing HTFSI was rapid with simple mixing. In contrast, the complete dissolution of the $UO_2CO_3$ did not initially occur in the IL containing HTFSI. The addition of 2 mL of water resulted in the complete dissolution of $UO_2CO_3$ in the IL containing 0.5 M HTFSI. The addition of water solvates the proton in the IL which facilitates the dissolution of $UO_2CO_3$. The method is consistent with the improved dissolution of lanthanide oxides in “wet” IL solutions.[19,58]

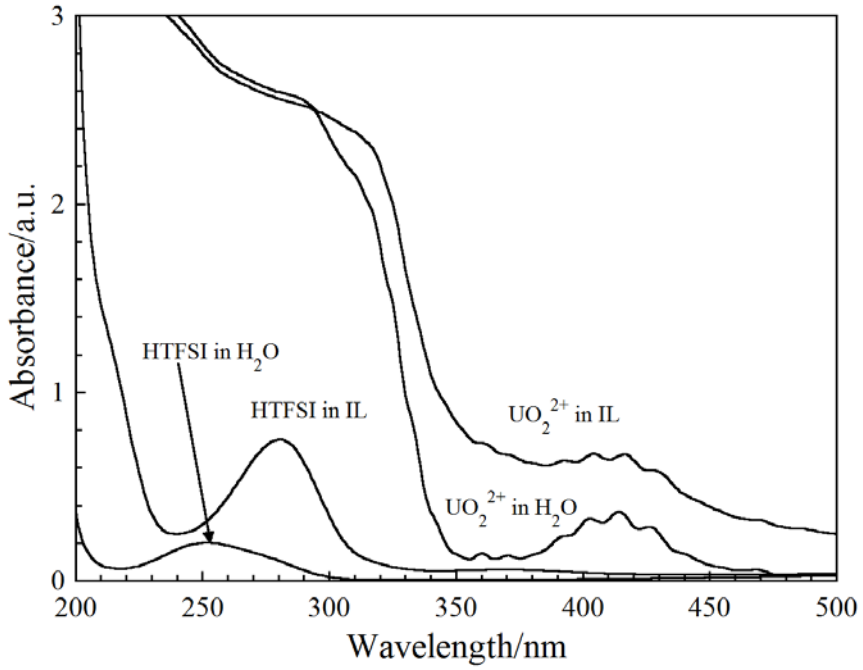


**Figure 34.** UV-Vis absorbance spectra of 0.5 M HTFSI in water and in IL $[Me_3N^nBu][TFSI]$. Absorbance spectra after the direct dissolution of 50 mM $UO_2CO_3$ into deionized water and IL $[Me_3N^nBu][TFSI]$ containing 0.5 M HTFSI.

It is unlikely that there is a change for the soluble species during the dissolution process for either solvent system given the preferential hexavalent oxidation state of uranium.[119] Therefore, it is assumed that the soluble species in solution is the uranyl ion, $UO_2^{2+}$, in both solutions. Furthermore, the absorbance spectra provided in **Figure 34** for the dissolution of $UO_2CO_3$ in water and IL are very similar indicative of similar soluble species. The characteristic absorbance bands between 350 – 450 nm are consistent with f-electron transitions associated with U(VI) complexes including uranyl nitrate, trifluoromethanesulfonate $[SO_3CF_3^-]$, bis(trifluoromethanesulfonyl)amide [TFSI, $N(SO_2CF_3)_2^-$)] and chloride in both solvents.[111-114,120,121] In addition, there is a dramatic change in the absorbance at higher energy (lower wavelength) with high absorbance intensities relative to the baseline of HTFSI in either water or IL. Similar absorbance at lower wavelength for lanthanide species has been previously attributed

to ligand to metal charge transfer complexes which have been observed for weakly coordinating ligands, including TFSI which act as sensitizing agents for high energy electronic transitions.[93] The combination of absorbance bands at low energy associated with water solvated $UO_2^{2+}$ and higher energy bands indicative of TFSI suggests that the anion interacts with the soluble uranium species in the presence of water for both solvent systems.

Although the absorbance for both samples is sufficiently high that no quantitative information can be derived, the data indicates that dissolution of $UO_2CO_3$ in IL and water results in the formation of $UO_2(TFSI)_2$ complexes and cannot be simply attributed to free TFSI ligand. Direct comparison of the data provided in **Figure 34** with other uranyl complexes dissolved in IL is complicated because the spectral region between 200 – 350 nm is not typically examined or shown.[111-114,122] However, a large absorbance shoulder at lower wavelengths is often observed in the spectra suggesting that the $UO_2^{2+}$ may have higher energy electronic transitions in IL environments. For example, previous work for the direct dissolution of $[Bmim]_2[UO_2Br_4]$ into IL shows an intense absorbance band at lower wavelengths consistent with the absorbance shown in **Figure 34**.[123] The high absorbance observed for the dissolution of $UO_2CO_3$ in both solvent systems may be indicative of coordination of the soluble $UO_2^{2+}$ species with $TFSI^-$ in both water and IL.

5.4.2 Uranium Oxide ($U_3O_8$) Dissolved in Ionic Liquid

The dissolution of $U_3O_8$ into dry IL was evaluated using UV-Vis spectroscopy, **Figure 35**. For comparison, absorbance spectra of dry $[Me_3N^nBu][TFSI]$ before and after being exposed to the oxidizing gas from the ozone generator for 120 hours are provided. The IL has little absorbance from 240 nm and throughout the rest of the UV-Vis range. However, after being exposed to the oxidizing gas the IL is slightly discolored a very light yellow of the IL and a

broad absorbance band centered at 404 nm. The characteristic absorbance spectra demonstrate that the soluble species following dissolution of the $U_3O_8$ into IL is uranyl (25.2 mM $UO_2^{2+}$ in **Figure 35**). Additionally, the dissolution of $U_3O_8$ required use of oxidizing gas and the hexavalent uranyl ion is the commonly encountered soluble uranium species. However, the distinct difference in the sharp intensity of the 424, 438, 452, and 468 nm absorbance bands compared to the remainder of the uranyl absorbance bands may indicate differences in the coordinating ions in this sample compared to the soluble uranyl in the $UO_2CO_3$ dissolution sample.

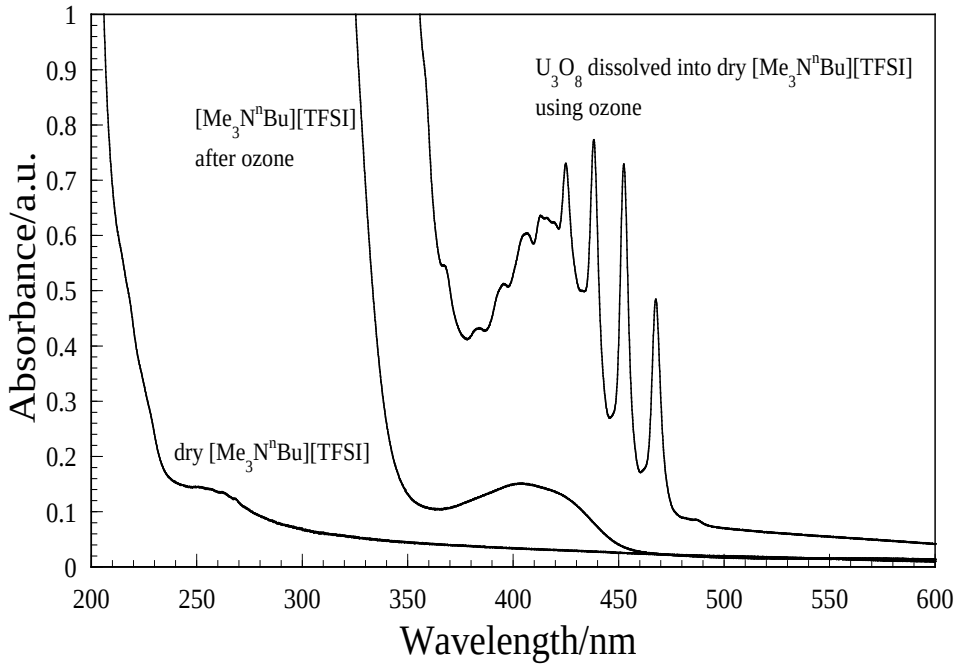


**Figure 35.** UV-Vis absorbance of soluble uranyl following the dissolution of $U_3O_8$ into dry $[Me_3N^nBu][TFSI]$, 25.2 mM $UO_2^{2+}$. For comparison, there also are absorbance spectra of dry $[Me_3N^nBu][TFSI]$ before and after being exposed to the oxidizing gas from the ozone generator for 120 hrs to simulate conditions of dissolution.

## 5.5 Electrochemistry

### 5.5.1 Voltammetry of Soluble Uranyl from Uranyl Carbonate Dissolved in Ionic Liquid

The voltammetric response of an Au electrode in IL containing 50 mM soluble $UO_2CO_3$ is provided as a function of increasing potential window in **Figure 36**. The background cyclic voltammetry for an Au electrode in $[Me_3N^nBu][TFSI]$ containing 0.5 M HTFSI (dashed line) is also provided for reference in **Figure 36(c)**. The assignment of the voltammetric waves and corresponding reactions are provided in **Table 7**.

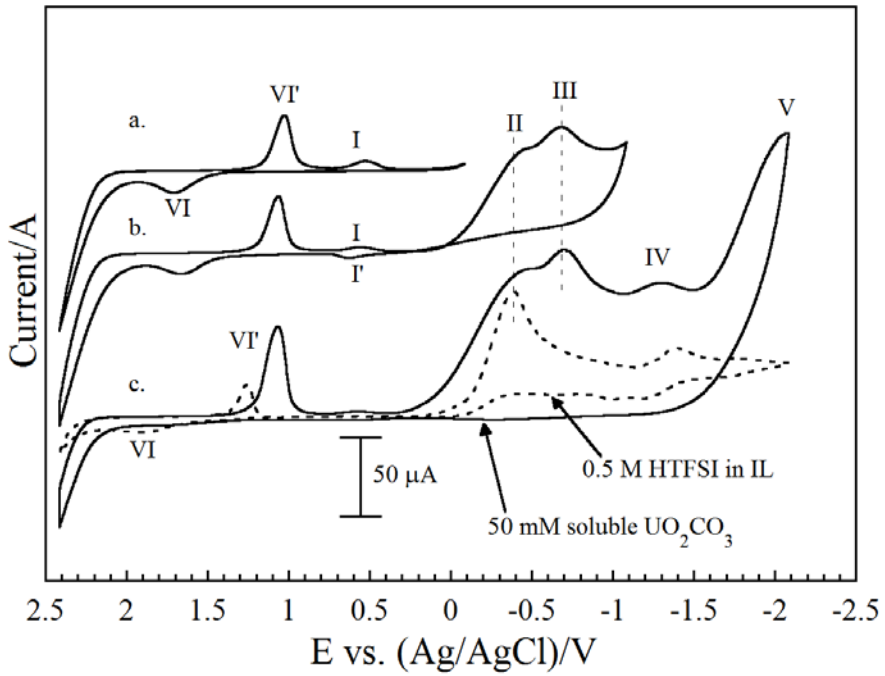


**Figure 36.** Cyclic voltammetry of an Au electrode in soluble $UO_2CO_3$ (50 mM) in IL $[Me_3N^nBu][TFSI]$ containing 0.5 M HTFSI in the potential range between **(a)** 2.4 to -0.2 V, **(b)** 2.4 to -1.1 V and, **(c)** 2.4 to -2.1 V. Cyclic voltammetry of an Au electrode in IL $[Me_3N^nBu][TFSI]$ containing 0.5 M HTFSI in the potential range between 2.4 to -2.1 V is provided for comparison (dashed line). Electrode area = 7.07 x $10^{-2}$ $cm^2$, scan rate = 50 mV/s.

The voltammetric waves observed for the IL containing 0.5 M HTFSI in IL are based on previous voltammetric studies for Au electrodes in IL containing HTFSI.[81] For example, the voltammetric wave labeled II has been attributed to the reductive adsorption of $H^+$ which is followed the subsequent reduction and reaction of $H^+$ with surface adsorbed species to produce

$H_2$ gas at the Au electrode.[84] In addition, the voltammetric waves labeled VI and VI′ were previously assigned to the oxidation of the gold electrode and reduction of the oxide, respectively, based on **Equation 4**.[75] The voltammetric responses provided in **Figure 36** indicate that there is a sufficient amount of water and dissociated proton such that the oxidation/reduction of Au can be resolved in the IL solution. Finally, wave IV has been previously attributed to the reduction of water in IL solution which produced $OH^-$ and $H_2$.[84]

**Table 7.** Summary of the proposed reactions and peak assignments of an An electrode in IL containing soluble $UO_2^{2+}$ and HTFSI.

| Peak | Proposed Reactions |
|---|---|
| I/I′ | $UO_2^{2+} + e^- \leftrightarrow UO_2^+$ |
| II | $H_{IL}^+ + e^- \longrightarrow H_{ads}$ and, $H_{ads} + H_{IL}^+ + e^- \longrightarrow H_2$ |
| III | $UO_2^{2+} + 2\ e^- \longrightarrow UO_{2\ ads}$ |
| IV | $H_2O + e^- \longrightarrow \frac{1}{2}H_2 + OH^-$ |
| V | $UO_2^{2+} + 2\ e^- \longrightarrow UO_{2\ ads}$ (bulk) |
| VI/VI′ | $Au_2O_3 + 6\ H^+ + 6\ e^- \leftrightarrow 2\ Au + 3\ H_2O$ |

The potential window utilized in **Figure 36(a)** encompasses the oxidation/reduction of the Au surface and the reduction of soluble $UO_2^{2+}$ to the pentavalent $UO_2^+$ species, wave I. The reverse process for the oxidation of the pentavalent $UO_2^+$ species is initially absent in the cyclic voltammetry suggesting that the reduction of $UO_2^{2+}$ is irreversible. However, an oxidative processes, wave I′, is resolved after extending the negative potential limit which can be attributed to the oxidation of $UO_2^+$ to $UO_2^{2+}$. In addition, when the potential is expanded to more negative

potential an additional reduction waves emerges, wave III, which is assigned to the initial deposition of $UO_2$ (ads) through a two electron reduction process. It is likely that the resolution of wave I′ is tied to the surface oxidation of $UO_2$(s) deposited on the Au surface, followed by the oxidation of pentavalent uranium species back to the hexavalent state. Previous studies support the two electron reduction of $UO_2^{2+}$ and formation of either solvated U(IV) in IL or surface deposited $UO_2$(s) on the electrode surface.[124,125] However, the lack of additional oxidative processes on the reverse scan suggests that the reductive deposition of the majority of the uranium species at the gold electrode is largely irreversible.

The sequential cyclic voltammetry associated with the reductive deposition of $UO_2$(s) is provided in **Figure 37** encompassing the potential window for the reduction process associated with wave III. The voltammetric response associated with wave III decreases with increasing voltammetric cycles. In addition, the voltammetry associated with the reduction/oxidation of $UO_2^{2+}$ decreases in intensity (wave I/wave I′), while the peak splitting increases.

The data suggests that the surface deposition of uranium species at the gold electrode occurs as the negative potential is extended past -1 V vs. Ag/AgCl. Furthermore, surface modification of the gold electrode with uranium species changes the electrode properties relative to the bulk gold which reduces the current with each sequential scan. However, the oxidation/reduction of the gold surface is still visible suggesting the $UO_2$(s) deposits do not completely cover the electrode.

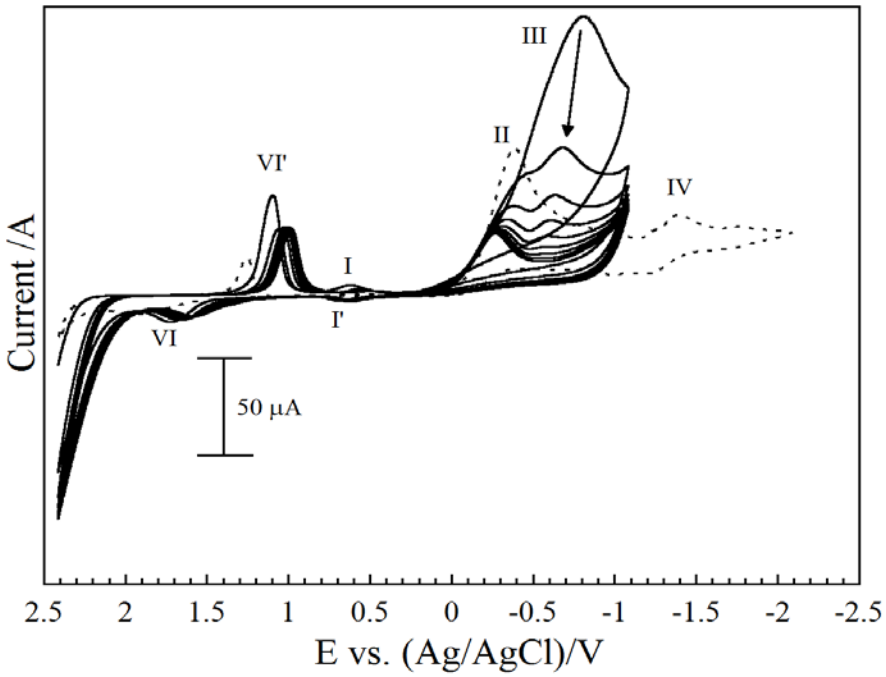


**Figure 37.** Sequential cyclic voltammetry of an Au electrode in soluble $UO_2CO_3$ (50 mM) in IL $[Me_3N^nBu][TFSI]$ containing 0.5 M HTFSI in the potential range between 2.4 to -1.1 V for the first ~10 cycles. Cyclic voltammetry of an Au electrode in IL $[Me_3N^nBu][TFSI]$ containing 0.5 M HTFSI in the potential range between 2.4 to -2.1 V is provided for comparison (dashed line). Electrode area = 7.07 x $10^{-2}$ $cm^2$, scan rate = 50 mV/s.

Similarly, when the reduction potential is extended to more negative potentials, -2 V vs. Ag/AgCl, the voltammetric response decreases dramatically with each sequential scan, **Figure 38**. The formation and reduction of gold oxide is lost after four voltammetric cycles (**Inset**) indicating that the gold surface is modified with $UO_2$ surface deposits. The voltammetric waves I and I′ are not resolved in any of the voltammetric cycles after the negative potential is extended. The voltammetric waves associated with proton adsorption and hydrogen evolution at the gold electrode are also completely absent after four voltammetric cycles, wave II. Finally, waves III and V diminish rapidly with each successive cycle. The loss of surface activity and diminished voltammetry with respect to soluble $UO_2^{2+}$ suggests that the electrodes surface has been

sufficiently modified that the bulk properties are more consistent with deposited uranium species rather than gold electrode.

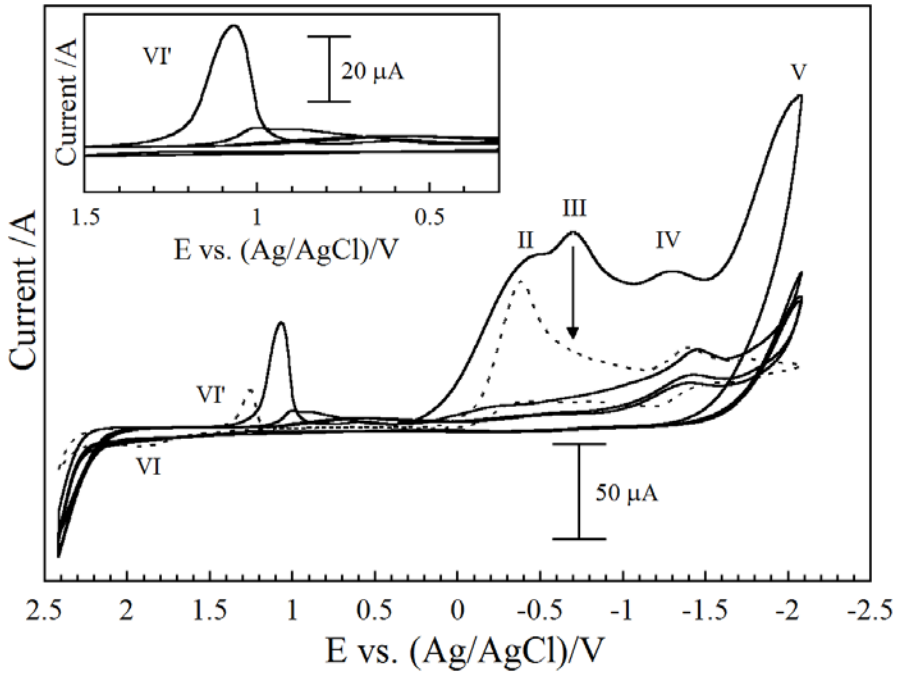


**Figure 38.** Sequential cyclic voltammetry of an Au electrode in soluble $UO_2CO_3$ (50 mM) in IL $[Me_3N^nBu][TFSI]$ containing 0.5 M HTFSI in the potential range between 2.4 to -2.1 V for the first ~4 cycles. Cyclic voltammetry of an Au electrode in IL $[Me_3N^nBu][TFSI]$ containing 0.5 M HTFSI in the potential range between 2.4 to -2.1 V is provided for comparison (dashed line). Electrode area = 7.07 x $10^{-2}$ $cm^2$, scan rate = 50 mV/s. **Inset:** Expansion of the reduction of gold oxide region for successive cycles during the deposition processes.

The voltammetry of IL solutions containing 5 mM soluble $UO_2^{2+}$ in IL containing 0.1 M HTFSI from the direct dissolution of $UO_2CO_3$ was also examined, **Figure 39**. The voltammetric response for the IL containing soluble $UO_2CO_3$ (5 mM) in IL is similar in the potential range between 0 V and -2V which was utilized in **Figure 37** and **Figure 38**. However, the voltammetric range encompassing the oxidation/reduction of the soluble $UO_2^{2+}$ in IL is significantly different at lower concentration. The oxidation/reduction of the gold electrode can

be observed at +0.9 V and +1.65 V for waves VI/ VI′, respectively. In addition, the reduction of the gold oxide at the working electrode is followed by a reduction of $UO_2^{2+}$ from the hexavalent state to the pentavalent species (0.4 V vs. Ag/AgCl). The reduction of $UO_2^{2+}$ was previously observed in **Figure 36(a)** and assigned as wave I. In contrast, the oxidation of U(V) to U(VI) is resolved in the reverse scan, wave I′, without extending the reduction potential window.

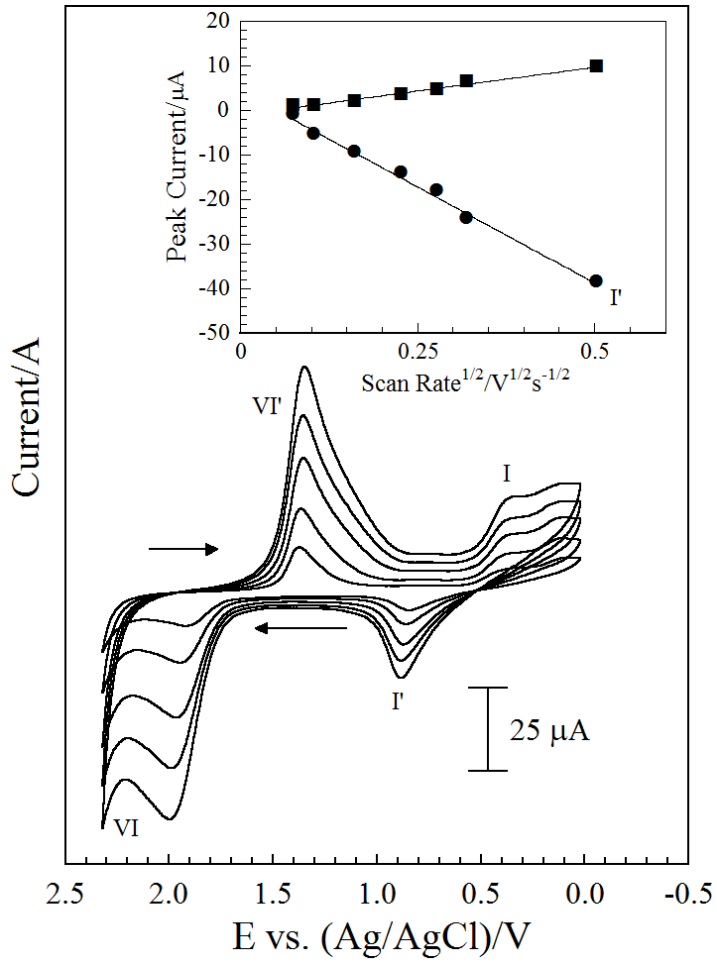


**Figure 39.** Cyclic voltammetry of an Au electrode in soluble $UO_2CO_3$ (~5 mM) in IL $[Me_3N^nBu][TFSI]$ containing 0.1 M HTFSI, as a function of scan rate (10, 25, 50, 75, 100 mV/s are shown for clarity) from +2.3 V to 0 V vs. Ag/AgCl. **Inset:** Plot of peak current versus the square root of the scan rate for scan rates of 5, 10, 25, 50, 75, 100, and 250 mV/s. Electrode area = 7.07 x $10^{-2}$ $cm^2$.

The results suggest that the disproportionation of pentavalent uranium species to U(VI) and U(IV) occurs as uranium concentration increases and the stability of the pentavalent uranium species is higher in the IL solution at lower concentration. In addition, the IL solution with 50 mM $UO_2^{2+}$ contains a higher concentration of proton and water which may influence the stability of the pentavalent species. These observations are consistent with experimental studies and modeling of U(V) stability which indicate that both the U(VI) concentration and proton availability largely dictate disproportionation.[126,127]

The voltammetry in **Figure 36(a)** and **Figure 39** is consistent with previous studies that show the reduction of $UO_2^{2+}$ produces a stable pentavalent uranium species in 1-butyl-3-methyl-imidazolium IL solutions.[44,128] The electrochemical response of uranyl chloride in 1-butyl-3-methylimidazolium nonafluorobutane-sulfonate (bmiNfO) also shows similar behavior at negative potentials consistent with sequential reduction of the uranyl ion.[129] The reduction has been previously assigned to the multi-step reduction of $UO_2^{2+}$ through a stable pentavalent intermediate to U(IV). Finally, the scan rate dependence was examined to ensure the oxidation/reduction processes for wave I and I′ are consistent with solution rather than surface processes. The linear dependences for the plots of peak currents for waves I and I′ versus the square root of the scan rate ($\nu^{1/2}$) are indicative of diffusion limited solution processes rather than surface adsorption of uranium species (**Inset**).

### 5.5.2 Voltammetry of Soluble Uranyl from Uranium Oxide ($U_3O_8$) Dissolved in Ionic Liquid

Spectroscopy has demonstrated that the soluble species of uranium in the IL following dissolution, whether of $UO_2CO_3$ or $U_3O_8$, is uranyl. The voltammetry of the soluble uranyl (25.2 mM) dissolved into dry [$Me_3N^nBu$][TFSI] was investigated at an Au foil, **Figure 40**. The

potential window for cyclic voltammetry was expanded incrementally towards the negative potential. The voltammetry observed indicates a multi-step reduction process with voltammetric waves located at potentials similar to those in **Figure 36**. Voltammetry of dry $[Me_3N^nBu][TFSI]$ which was exposed to the same dissolution by oxidizing gas for 120 hours is presented for comparison (dashed line). However, the relative magnitude of these voltammetric waves differ in **Figure 40** compared to **Figure 36**. This may be influenced by a few factors including less relative concentration of soluble uranyl in this sample and additional chemistry which may occur within the IL due to the mixture of oxidizing gas used for dissolution of the oxide.

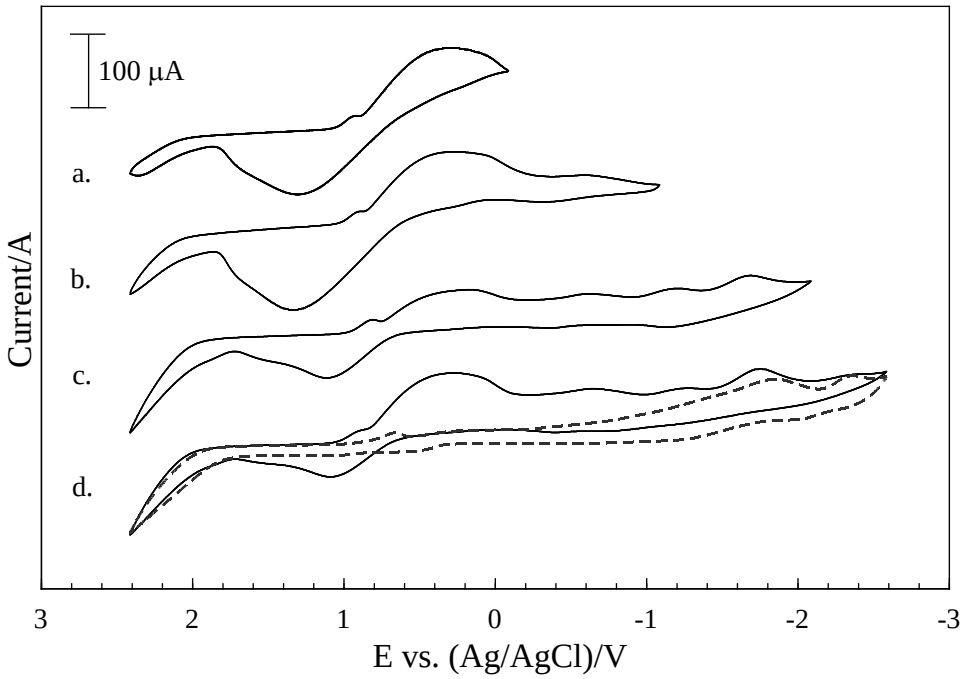


**Figure 40.** Cyclic voltammetry of an Au electrode in soluble $UO_2^{2+}$ (25.2 mM) in IL $[Me_3N^nBu][TFSI]$ from the dissolution of $U_3O_8$ in the potential range between (a.) 2.4 to -0.1 V, (b.) 2.4 to -1.1 V, (c.) 2.4 to -2.1 V, and (d.) 2.4 to -2.6 V. Cyclic voltammetry of an Au electrode in IL $[Me_3N^nBu][TFSI]$ exposed to the ozone generator with air feed gas for 120 hrs in the potential range between 2.4 to -2.6 V is provided for comparison as a background (dashed line). Electrode area = 7.07 x $10^{-2}$ $cm^2$, scan rate = 100 mV/s.

The oxidation/reduction processes are consistent with the previously identified wave I and I′, **Figure 36**, and were examined by various scan rates and presented in **Figure 41**. The represents the first redox of the soluble $UO_2^{2+}$ in the IL through a pentavalent intermediate to U(IV) prior to more reducing potential. The linear response of the peak current in relation to the square root of the scan rate ($\nu^{1/2}$) is consistent with a solution rather than surface process (**Inset**).

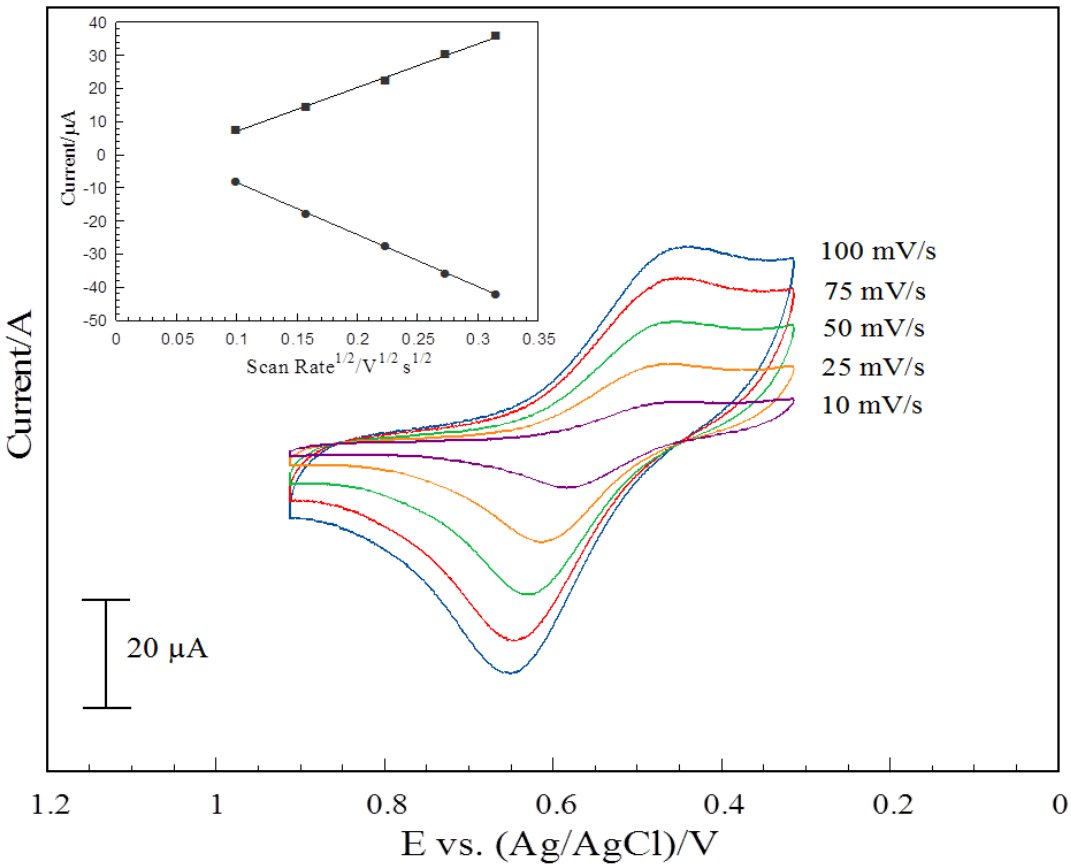


**Figure 41.** Cyclic voltammetry of an Au electrode in soluble $U_3O_8$ (~50 mM) in IL $[Me_3N^nBu][TFSI]$ containing 0.1 M HTFSI, as a function of scan rate (10, 25, 50, 75, 100 mV/s are shown for clarity) from + 0.9 V to 0.3 V vs. Ag/AgCl. **Inset:** Plot of peak current versus the square root of the scan rate. Electrode area = 7.07 x $10^{-2}$ $cm^2$. Initial scan direction is from positive to negative potential.

5.6 Scanning Electron Microscopy and Energy Dispersive X-ray Spectroscopy (SEM/EDS) Analysis of Electrodeposits

Although the voltammetry presented suggests that the deposition of uranium species at gold electrodes occurs, it does not provide any direct evidence. SEM was conducted to confirm that the surface deposition of uranium species was achieved, **Figure 42**. The potentials utilized for deposition were at sufficiently negative potentials, -2 V, to ensure that any deposits remain on the gold electrode surface.

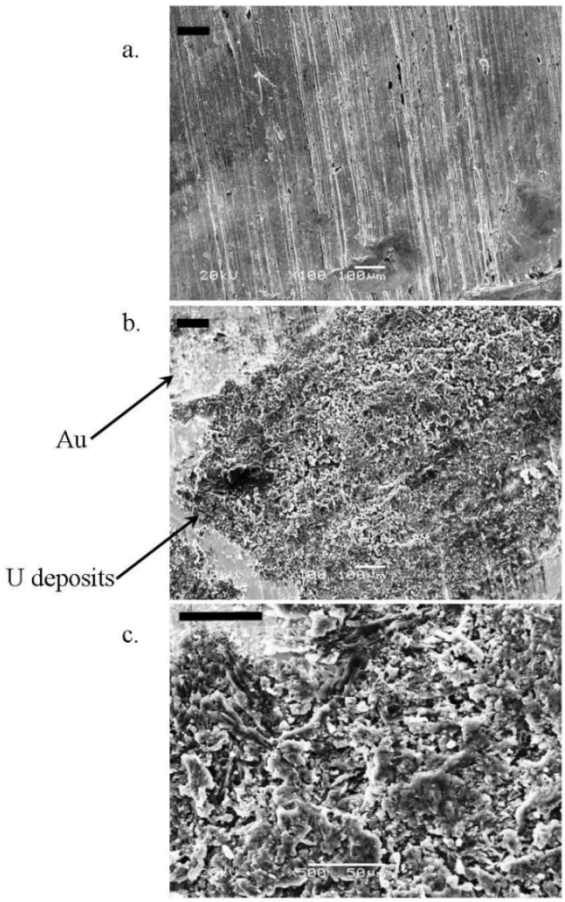


**Figure 42.** SEM of **(a)** an Au electrode prior to electrochemical deposition, and after electrodeposition of uranium species from $UO_2CO_3$ dissolved into $[Me_3N^nBu][TFSI]$ containing 0.5 M HTFSI, **(b)** at x100 magnification, and **(c)** at x 500 magnification.

The clean Au electrode surface is provided in **Figure 42(a)** with the scale bar provided in the top left corner (100 μM) for comparison to Au surfaces with uranium deposits. The SEM image of uranium deposits at the same magnification (x100) is provided in **Figure 42(b)**. The gold surface and uranium deposits are labeled for clarity. In addition, the SEM of uranium deposits at higher magnification (x500) is provided in **Figure 42(c)**. The uranium surface deposits are visible on the Au surface in **Figure 42(b)** and **(c)**. EDS analysis of the surface deposits is provided in **Figure 43** for the Au surface prior to deposition (dashed line) and after deposition of uranium species on the electrode surface (solid line). The EDS spectra for the uranium deposits show characteristic bands associated with the deposition of uranium species which are labeled for clarity.[103] Bands for the gold surface are not prominent in the EDS for the surface deposits indicating they are sufficiently thick to mask the gold surface. The data is consistent with the electrochemical data in **Figure 38** (**Inset**) which showed a diminished current response for the Au electrode as the surface deposition of uranium species occurs.

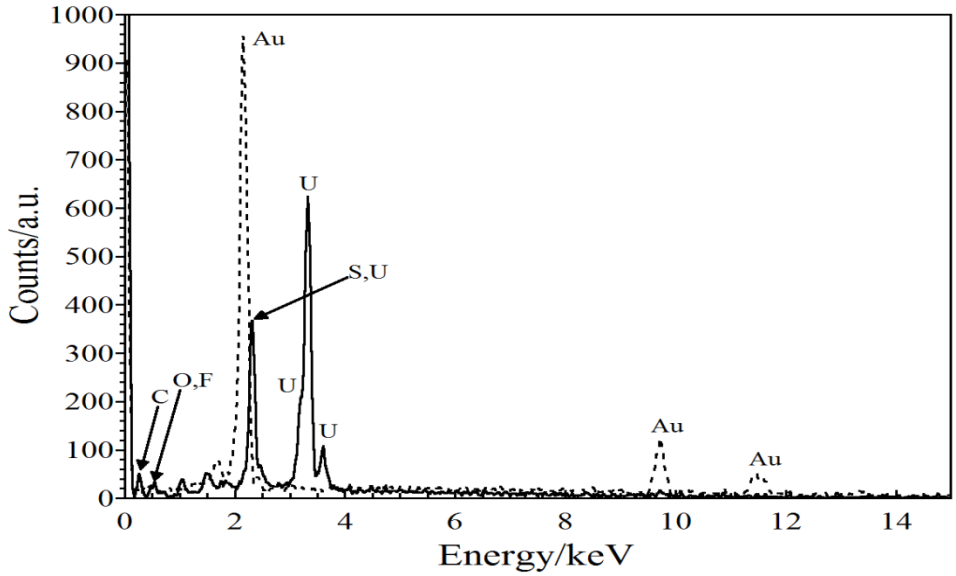


**Figure 43.** EDS analysis of the U surface deposits on Au from Figure 42, with species labeled. The dashed line represents the EDS spectrum of the clean Au surface.

A number of electrodepositions from various $U_3O_8$ dissolution sample solutions were attempted. An example of successful deposition from the direct dissolution IL solutions was the deposition on Au foil from the original $U_3O_8$ dissolution into $[Me_3N^nBu][TFSI]$ containing 3.27 M HTFSI. Electrodeposition was conducted at constant potential of -1.78 V (vs. Ag/AgCl) for 48 hours on Au foil. A visible dark grey deposit covered the surface exposed to deposition. The deposit density was calculated to be 0.0148 g/ $cm^2$. The SEM images below in **Figure 44** show the magnification and morphology of the deposit at x35 and x1000. EDS, **Figure 45**, confirmed uranium and oxygen to be present, suggesting the deposits to be a form of uranium oxide. The carbon and fluorine could be in the spectra from residual IL on the surface. The small amounts of aluminum, silicon, and sodium contaminants origins could be from the molecular sieves which were used to reduce water in the IL samples.

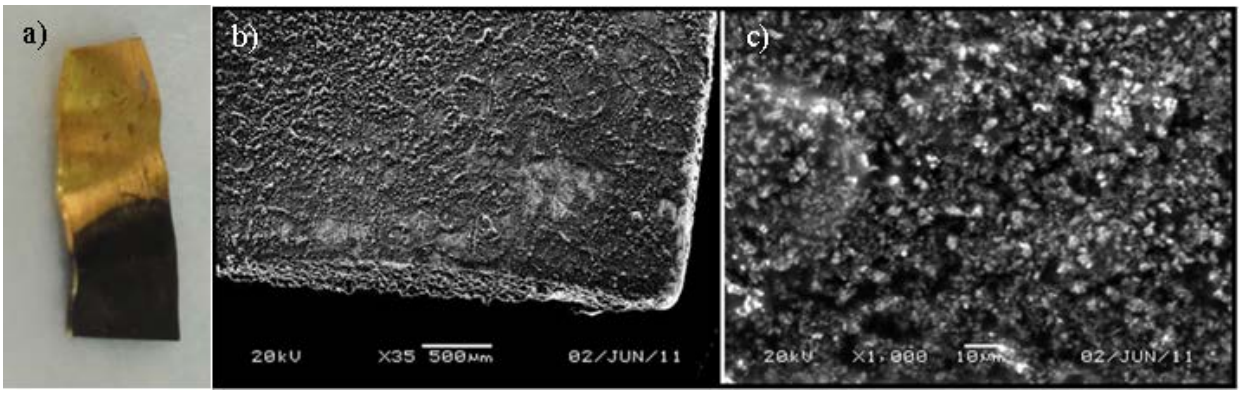


**Figure 44.** Images of **(a)** an Au electrode after deposition of uranium species from $U_3O_8$ dissolved into $[Me_3N^nBu][TFSI]$ containing 3.27 M HTFSI **(b)** SEM at x35 magnification of the deposit and **(c)** at x1000 magnification. Deposition for 48 hours at E = -1.8 V vs Ag/AgCl.

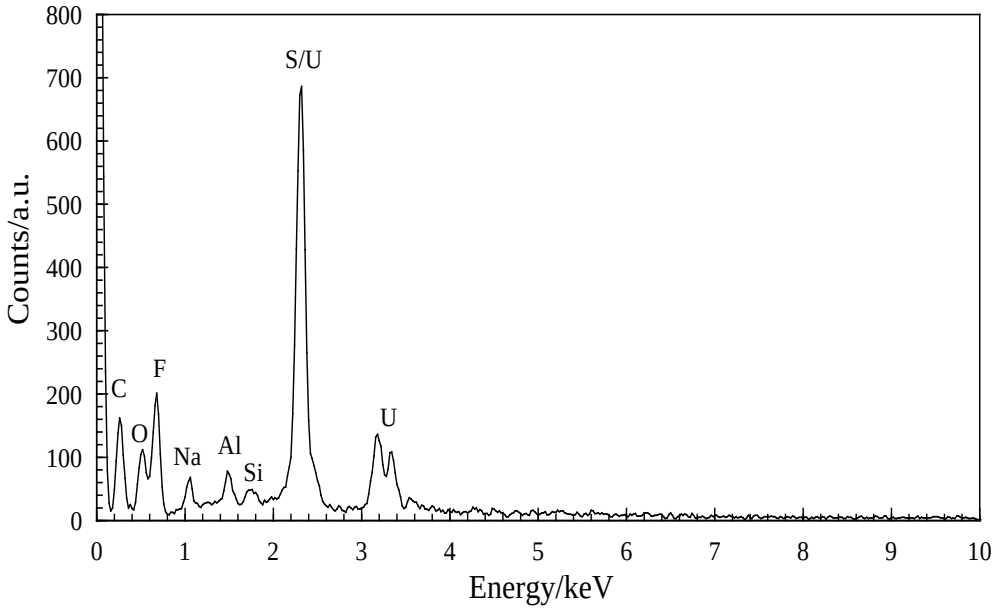


**Figure 45.** EDS analysis of the U surface deposits on Au from Figure 44, with species labeled.

However, it should be noted that not all depositions were successful to the extent of that presented. Optimization of electrodeposition still needs to be evaluated. Since this was one of the most successful electrodeposits, the inclusion of HTFSI may need to be investigated to understand if this does improve the ability to electrodeposit U from the IL.

## 5.7 Conclusions

The present work has demonstrated the direct dissolution of $UO_2CO_3$(s) in IL $[Me_3N^nBu][TFSI]$ containing water and HTFSI can be achieved. The data indicate that the direct dissolution can be initiated with degassing of the solution under argon atmosphere in pristine IL containing residual water. However, the process is slow and the solubility is limited due to the poor displacement of carbonate by low concentrations of proton in the IL. Enhanced dissolution was achieved with the addition of water and HTFSI to the IL providing a higher concentration of dissociated protons in the IL. The direct dissolution and solubility of $UO_2CO_3$(s)

was increased from 5 mM to 50 mM with the addition of HTFSI and water indicating that the solubility is enhanced through the increased dissociation of the acid allowing for proton facilitated displacement of carbonate.

Dissolution of the oxide, $U_3O_8$, required oxidizing gas. Studies of the dissolution determined that HTFSI acid was not necessary. The dissolution was attempted using various gases including air, $N_2$, $O_2$, and $N_2O$. However, only air feed gas to an ozone generator was successful in achieving dissolution. The dissolution mechanism therefore remains unknown, but may include ozone in combination with another nitrogen or oxygen based oxidizing gas or gas radical.

The UV-Vis data suggests that $UO_2^{2+}$ is the soluble species and in the IL solution as well as in water. In addition, the soluble $UO_2^{2+}$ was evaluated electrochemically and the reduction of U(VI) to form the stable intermediate U(V) was resolved. Additional reduction processes were elucidated and attributed to the two electron reduction of $UO_2^{2+}$ to $UO_2$ and the subsequent deposition of uranium oxide species at the electrode surface were identified using SEM and EDS analysis. Finally, the methods detailed provide pathways for increasing the solubility of actinide or lanthanide carbonates and oxides into ILs. Initial studies of the IL system, in the presence of water and HTFSI acid, demonstrate the electrochemical properties of the soluble uranyl and the potential dependent deposition of uranium oxide species at an electrode surface.

# Chapter 6: Initial Studies of Electrochemical Separation of Uranium from Neodymium in Ionic Liquids

This work was performed at Los Alamos National Laboratory under the mentorship of George S. Goff and Wolfgang H. Runde in the Chemistry Division.

The literature has suggested that the properties of ILs could potentially be utilized in the nuclear fuel cycle for separations and recycling. However, an important question remains whether a separation of uranium from other fission products such as the lanthanides could be achieved using electrochemical methods and ILs. This chapter provides an initial study of the feasibility of separating U from a mixture of U/Nd using electrochemical methods. The electrodeposition was examined for U/Nd mixtures in three different ILs which all contain the same TFSI anion. The electrochemical deposits obtained from the different ILs were rinsed and dissolved into 1 M $HClO_4$ for UV-Vis spectroscopy and ICP-AES analysis.

## 6.1 Introduction

When discussing separations, a separation factor (also referred to as a decontamination factor) may be stated. A separation factor is relating the presence of two constituent elements, for example element A and element B, before and after a separations process. For the purposes of calculating the separation achieved by the electrodeposition from the U/Nd mixture in ILs, the following relation was used where U was element A and Nd was element B:

$$SF = \frac{\left(\frac{Q_A}{Q_B}\right)_f}{\left(\frac{Q_A}{Q_B}\right)_i} \quad \textbf{(Eq. 30)}$$

Electrochemical methods utilizing molten salts have been developed and tested at the engineering scale for the separation of actinides and lanthanides in spent nuclear fuel, from molten salt or sodium-cooled fast reactors, which are some of the proposed future reactor designs. Recovery of U has been performed in chloride or fluoride based molten salts (for example LiCl-KCl and $UCl_3$).[130,131,132,133] Oxide based fuel is converted to metal during the electrolytic reduction process. Electrochemical refining is achieved by placing the spent fuel inside a basket followed by anodic dissolution into the molten salt. Subsequent deposition of high purity uranium metal is achieved at the cathode.

Herrmann and Li reported separation factors of the U metal product of electrorefining in a molten salt to be 5.3, 221, and 465 for Np, Pu, and Am respectively.[130] The other fission products and lanthanides primarily are retained within the molten salt after either the electrolytic reduction or electrorefining steps. A study performed by Kuznestov et. al. determined electrochemical potentials of uranium and lanthanum in the LiCl-KCl molten salt system but also observed that the separation coefficients decreased as the temperature of the molten salt was increased from 450 to 550 °C, suggesting that a better separation would be performed at lower temperature.[134] The drawbacks to pyroelectrochemical reprocessing include the operation at relatively high temperatures (500 – 650 °C) and the need for an inert gas atmosphere glovebox or hot cell.

ILs have shown promise due to their low vapor pressure and wide electrochemical windows.[13] Indeed, the studies up to this point have shown the capability of ILs to support electrodeposition of f-elements.[15,16] In addition, the ionic nature of the solvent has the ability to undergo minimal radiolysis.[135,136] All of these factors are reasons in which ILs have been investigated and proposed for possible applications to the nuclear fuel cycle for recycling.[137]

The use of ILs in an advanced recycling scheme would require that the separation of U or even perhaps group actinides (U, Np, Pu) from other fission products such as the lanthanides. The aqueous potentials of deposition for the f-elements suggest separation is feasible.[26] However, a review of the literature does not demonstrate that the electrochemical separation in ILs has been examined in detail.

In the present study, three ILs sharing the same bis(trifluoromethanesulfonyl)imide [TFSI] anion but different cations were investigated (**Figure 46**). These ILs exhibit different potential windows ([PMPip][TFSI] > [$Me_3N^nBu$][TFSI] > [EMIM][TFSI]) and relative melting points and viscosities to mention a couple differences which are in **Table 8**.[100] Consideration was given to selecting the lanthanide from which uranium would attempt to be separated in the ILs using potential mediated deposition processes. One of the most prevalent fission product lanthanides is Nd, previously presented in Chapter 1 (**Table 1**).[3] The selection of Nd was also due to the characteristic absorbance bands[138] in the visible spectrum which could be monitored in addition to the absorbance of uranyl.[139]

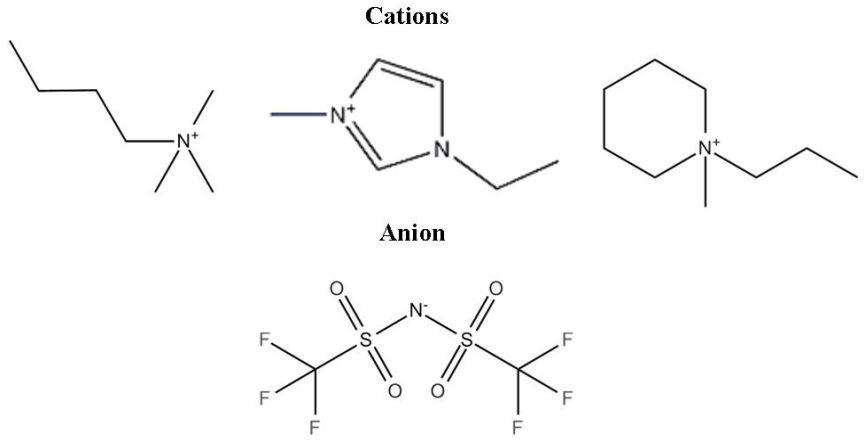


**Figure 46.** Cations (Left to right): n-trimethyl-n-butyl ammonium [$Me_3N^nBu$], 1-ethyl-3-methylimidazolium [EMIM], 1-methyl-1-propylpiperidinium [PMPip]. Anion: bis(trifluoromethanesulfonyl)imide [TFSI]

**Table 8.** Melting point and viscosity of the ILs

| Ionic Liquid | Melting point (°C) | Viscosity (cP, at 25°C) |
|---|---|---|
| [EMIM][TFSI] | -16 | 35.55 |
| $[Me_3N^nBu][TFSI]$ | 7 | 124.48 |
| [PMPip][TFSI] | 12 | 151 |

## 6.2 Methods and Materials

### 6.2.1 Chemicals and Solutions

Stock solutions were prepared as needed of 1 M perchloric ($HClO_4$) and 1 M bis(trifluoromethanesulfonyl)imide (HTFSI) acid solutions for the UV-visible spectroscopy. To prepare 1 M $HClO_4$, 8.700 mL of 70% concentrated $HClO_4$ was added to a 100 mL volumetric flask and diluted with ultrapure water. To prepare the 1 M HTFSI acid, 35.14375 g of 80% HTFSI (Io-li-tec) was diluted with ultrapure water in a 100 mL volumetric flask. A 2% HCl stock solution was prepared for dilutions of the dissolved deposits or extractions to prep the samples to concentrations appropriate for the ICP-AES analysis.

The neodymium source was the oxide ($Nd_2O_3$) from Alfa Aesar (99.9%, lot D22U013). It was thermally treated in a tube furnace under air and held at 800 °C and 1200 °C for six hours. This was done to confirm the material was not a hydroxide or hydrated form which can develop over time and helps ensure more accurate Nd concentrations in gravimetrically prepared samples. The oxide was characterized before and after being thermally treated. A stock of 0.297 M Nd in 1 M HTFSI would be made dissolving 0.4998 g dried $Nd_2O_3$ per 10 mL solution.

Depleted uranium was used in the form of uranyl carbonate ($UO_2CO_3$), which had been previously precipitated by passing $CO_2$ gas through an acidic solution of uranyl. The precipitated $UO_2CO_3$ product was kept under solution. A portion of the $UO_2CO_3$ would be transferred to a 50

mL plastic centrifuge tube and excess solution was removed before leaving the product to dry in the hood with the lid off. The $UO_2CO_3$ was massed (~3.6535 g, wet) and dissolved into 30 mL 1 M HTFSI to prepare a stock solution.

The ILs that were investigated were: n-trimethyl-butylammonium bis(trifluoromethanesulfonyl)imide $[Me_3N^nBu][TFSI]$ (Io-li-tec, 99%), 1-ethyl-3-methylimidazolium bis(trifluoromethanesulfonyl)imide [EMIM][TFSI] (Io-li-tec, 99%), and 1-methyl-1-propylpiperidinium bis(trifluoromethanesulfonyl)imide [PMPip][TFSI] (Io-li-tec, 99%). The ILs were used as received.

The Nd concentrations in the ILs were prepared to be approximately 50 mM. Preparing samples of either U, Nd, or both in the IL was accomplished by pipetting 8.929 mL of the Nd in 1 M HTFSI stock and/or 8.065 mL of the $UO_2^{2+}$ in 1 M HTFSI stock into a 100 mL round bottom flask. The flask was then connected to a rotavap evaporator with a water bath set to 65 - 85°C and allowed to dry until the excess water and acid were removed resulting in a thick sticky substance remaining. The flask was then removed and 50 mL of the IL was added and shaken or stirred until dissolved into the IL.

### 6.2.2 Powder X-ray Diffraction

Samples of $Nd_2O_3$ were first ground in a mortar and pestle to a powder and then an appropriate amount was used to fill the plastic sample puck. Powder X-ray diffraction data was collected on a Bruker D8 Advance diffractometer. The instrument was configured with Ni-filtered Cu Kα (1.54059 Å) radiation and a silicon strip detector (Lynxeye). Experimental diffraction patterns were compared with the Inorganic Crystal Structure Database (ICSD).

### 6.2.3 Electrodeposition

Electrochemistry was performed using EG&G Princeton Applied Research Potentiostats/Galvanostats Model 273A. Constant potentials of -1.2, -2.0 and -2.8 V were applied when attempting electrodeposition from samples and held for 12 hours. A Pt mesh or coil was used as the counter electrode and an Ag wire as a quasi reference electrode. The electrode for deposition was a piece of Cu foil (0.005" thick) that was cleaned by sandpaper, a 1 M $HClO_4$ wash, a water rinse, then methanol wash before drying in an oven at elevated temperature. Electrochemistry was performed under benchtop conditions with the sample in an oil bath at elevated temperature. All references to potentials in this chapter are reported versus the Ag wire quasi reference electrode.

Deposits that were obtained were rinsed with ultrapure water, dipped in methanol, allowed to dry, and then dissolved into 1 M $HClO_4$ for spectroscopic purposes.

### 6.2.4 Extractions

Extractions were performed on aliquots of the IL samples to determine the initial concentration and ratio of U/Nd and, when possible, also after electrochemistry was performed. 2 mL of the IL sample was contacted with 1 mL 1 M $HClO_4$ in 15 mL centrifuge tubes, vortexed for 2 minutes and then centrifuged (5000 rpm 5 minutes). The aqueous portion was removed by pipette and then the process was repeated once more for a total of 2 mL 1 M $HClO_4$ having been contacted with 2 mL of the IL sample. The aqueous phase was collected for spectroscopic and elemental analysis.

### 6.2.5 UV-Visible Spectroscopy

A Cary 6000i UV-Vis-Near IR spectrophotometer was used to collect UV-Visible data. Samples were analyzed at room temperature in 1 cm plastic cuvettes in the range of 820 – 300

nm. When appropriate, such as for deposit dissolutions or the aqueous phase of extractions, a baseline spectra of 1 M $HClO_4$ was collected and subtracted from sample spectra.

### 6.2.6 Inductively Coupled Plasma – Atomic Emission Spectroscopy (ICP-AES)

The aqueous portions of IL sample extraction and dissolved electrodeposits were diluted with 2 % HCl as necessary (1:10 up to 1:5,000 by serial dilution, depending on the estimated uranium or neodymium concentrations in the originating sample) and then underwent elemental analysis on a Thermo Scientific iCAP 6500. The appropriate dilution factors were accounted for in calculating uranium and neodymium concentrations. The results are further reported in the relative concentration of U:Nd in the originating IL sample and of the resulting dissolved deposit. The deposit ratio can be divided by the initial ratio to provide a separation factor (SF).

## 6.3 UV-Visible Spectroscopy of Soluble Uranium and Neodymium in Ionic Liquids

After preparing the combined uranium and neodymium in the ILs, the samples needed to be analyzed for relative metal concentrations. UV-Vis spectroscopy offers a non-destructive technique to check the concentration and relative ratio of U:Nd in the IL samples before and after various electrodeposition attempts. For the initial ratio, the metals were extracted from the ILs into 1 M $HClO_4$ and then UV-Vis spectroscopy was performed. For electrodeposits, as much of the deposit on Cu foil as possible was dissolved off into 1 M $HClO_4$ and the UV-Vis spectra was compared to the initial U:Nd concentration. Since the UV-Vis spectra presented are of combined uranium and neodymium in 1 M $HClO_4$, **Figure 47** provides an example absorbance spectrum of 50 mM Nd in 1 M $HClO_4$ featuring multiple transitions in the UV-Visible range with the most prominent being 801 and 575 nm. The prepared U and Nd in ILs were contacted with 1 M $HClO_4$ and the aqueous extractions are presented in **Figure 48**. This provides the initial

concentration and ratio of U:Nd in the samples prior to electrodepositions. The characteristic wavelength of 575 nm was monitored for Nd and 414 nm was monitored for $UO_2^{2+}$, respectively.

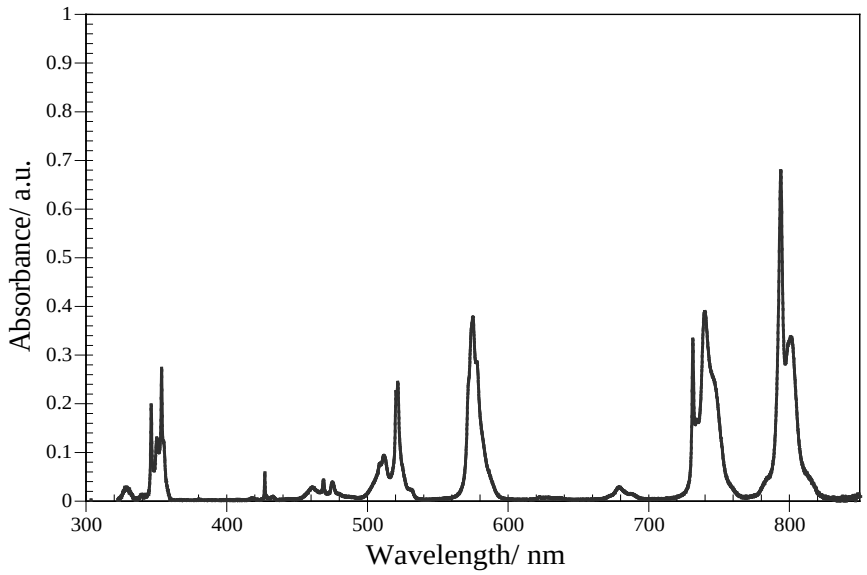


**Figure 47.** UV-Vis spectra of 50 mM Nd in 1 M $HClO_4$

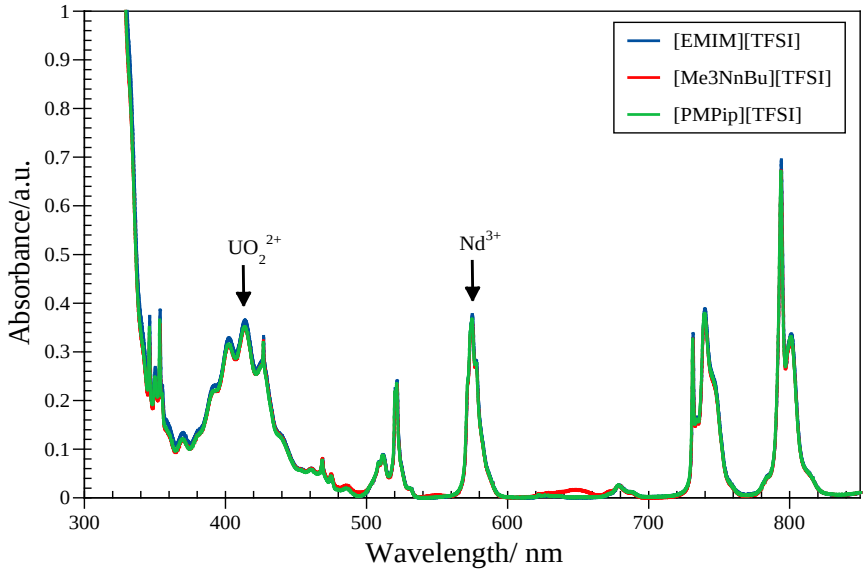


**Figure 48.** UV-Vis spectra of the mixed U and Nd in 1 M $HClO_4$ after extraction from the IL

Kondo et. al. reports that Nd was able to be electrodeposited from triethyl-pentyl-phosphonium bis(trifluoromethanesulfonyl)amide ([P2225][TFSA]) on Cu at -3.1 V under elevated temperature (150 °C) to lower the viscosity and increase mass transfer.[140] In addition, a number of studies have shown U to be electrodeposited from ILs as well.[125,129,141] Since ILs offer a wide electrochemical potential window for deposition of the actinides and lanthanides, a separation will rely upon sufficient differences in the reduction potentials or diffusion coefficients. The electrodeposition was also attempted for the individual species of neodymium and uranium from the ILs to determine the reduction potentials. The results indicate that neodymium is not deposited effectively at the potentials more positive of -2.8 V vs Ag wire quasi reference electrode. All potentials within this chapter are relative to the Ag wire quasi reference electrode. In contrast, uranium oxide was able to be electrodeposited to some extent from the ILs at these potentials. It was therefore anticipated that uranium would predominantly be electrodeposited and separated from the U/Nd mixture in the ILs at potentials of -2.8 V and more positive.

Examples of dissolved electrodeposits absorbance spectra are presented in **Figures 49**, **50**, and **51**. These represent an example of the deposits which resulted in the best separation factors obtained from the applied potential -2.0 V for each of the ILs. Deposit C from the U/Nd mixture in [EMIM][TFSI] in **Figure 49** had the lowest apparent separation factor as well as less apparent deposit compared to the other ILs. Deposit A from the U/Nd mixture in [$Me_3N^nBu$][TFSI] (**Figure 50**) and Deposit B from [PMPip][TFSI] (**Figure 51**) showed an increased separation of U from the Nd.

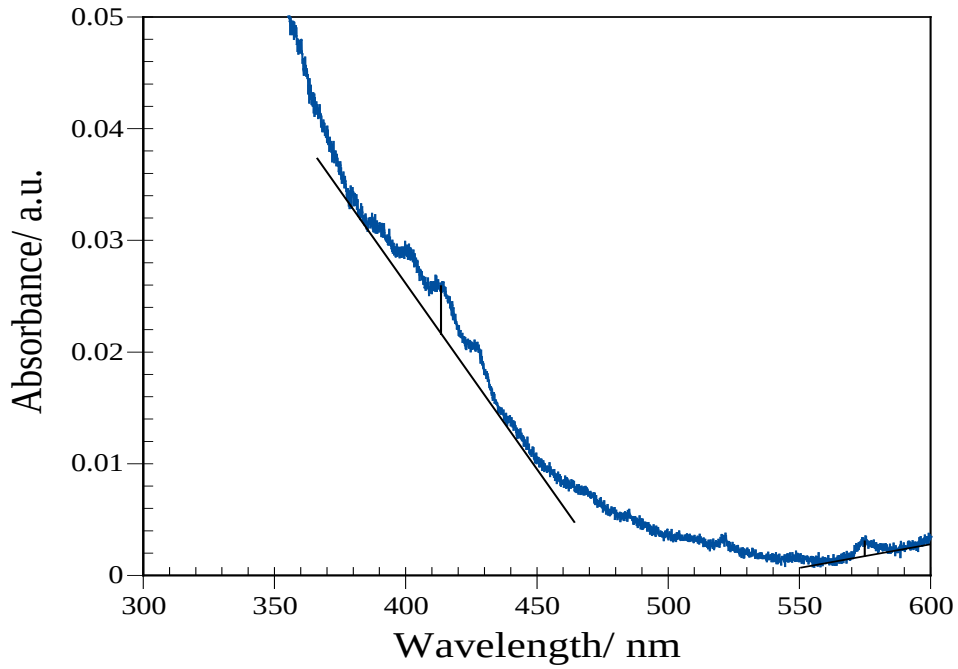


**Figure 49.** UV-Vis spectra of Deposit C obtained from -2.0 V applied for 12 hrs, Nd and U in [EMIM][TFSI], dissolved deposit in 1 M $HClO_4$

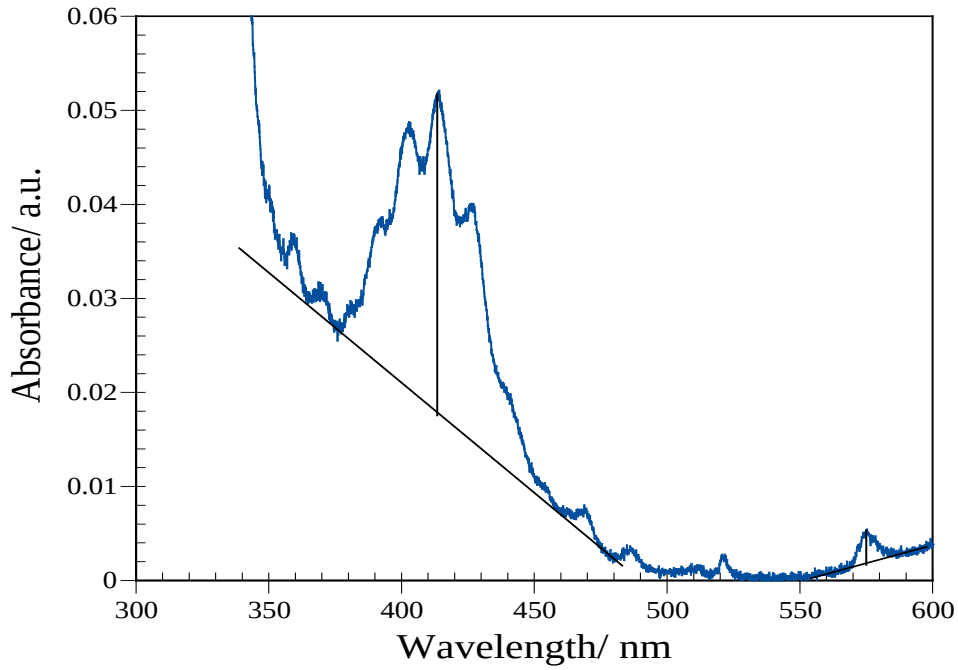


**Figure 50.** UV-Vis spectra of Deposit A obtained from -2.0 V applied for 12 hrs, Nd and U in $[Me_3N^nBu][TFSI]$, dissolved deposit in 1 M $HClO_4$

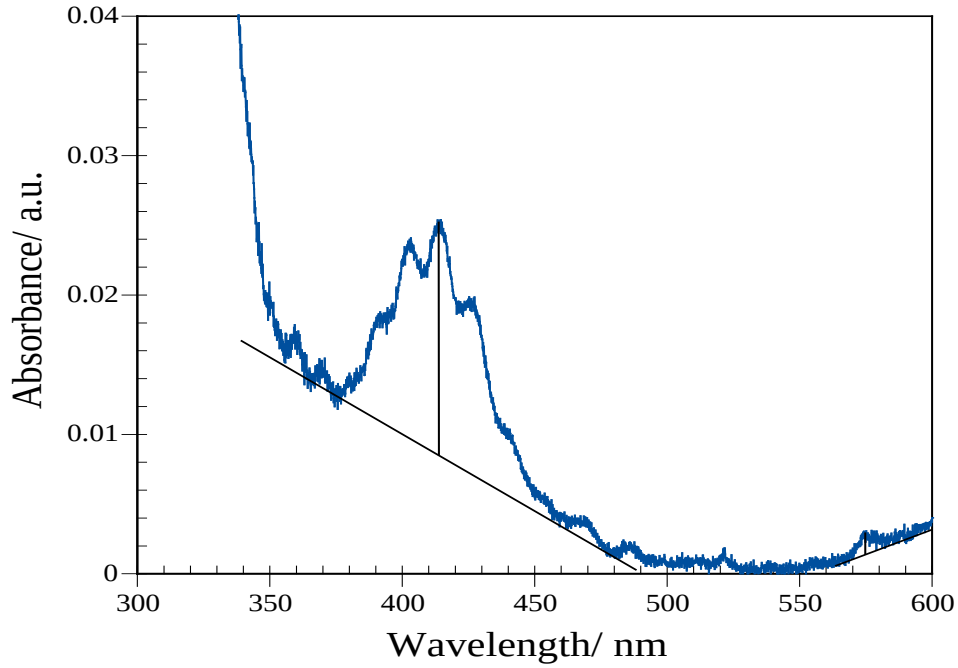


**Figure 51.** UV-Vis spectra of Deposit B obtained from -2.0 V applied for 12 hrs to Nd and U in [PMPip][TFSI], dissolved deposit in 1 M $HClO_4$

The UV-Vis spectra of dissolved deposits give an indication of the apparent success of the electrodeposition and separation due to the relative absorbance of the $UO_2^{2+}$ compared to $Nd^{3+}$ compared to the relative concentrations in the ILs. However, many of the absorbance spectra of dissolved deposits had extensive convolution due to some dissolved Cu from the working electrode and possibly some interference from residual or trapped ILs. These contaminants, along with limited obtained deposit in some samples, sometimes drastically influenced the baseline which made determining concentrations accurately more difficult. Black lines have been added to the spectra in an attempt to provide an adjusted baseline and another to relate the height of the absorbance lines at 414 nm and 575 nm. Due to these interferences, it was therefore necessary for a portion of the originating IL mixture samples and dissolved electrodeposits to also be analyzed by ICP-AES for more accurate determination of U:Nd ratios and for determination of separation factors (SF).

## 6.4 Inductively Coupled Plasma – Atomic Emission Spectroscopy Results

To achieve separation by electrochemical methods, an IL must have a suitable potential window and physical properties or operating conditions to enhance the deposition of U relative to the other components. More deposit could be obtained with a greater overpotential (potential much more negative than required for deposition), however extending the potential too much may negatively impact separation as other lanthanides and fission products could be deposited as well. Ideal separation therefore will require an understanding of the IL system and operational parameters and a selection to balance these properties. This represents an initial study probing the relative ability to achieve separation of U from Nd in these three selected ILs.

The results from the ICP-AES analysis of the dissolved deposits obtained at the three potentials for each of the ILs is presented below in **Table 9**. The initial U:Nd ratio in the sample was determined by analysis of the extraction performed in 1 M $HClO_4$. At least four deposits onto Cu were attempted from each IL sample at each increasing negative potential (-1.2 V, -2.0 V, and -2.8 V). A separation factor (SF) is calculated by dividing the ratio of U:Nd in the dissolved deposit by the U:Nd initially in the IL sample. As expected, most deposits indicate a higher relative deposition of U than Nd from the ILs.

There were some differences in the results comparing between the deposits obtained by the ILs. Deposits at -2.8 V from [EMIM][TFSI] appeared to be significantly degrading the IL and often resulted in poor deposit and separation within the deposit. Inversely, often not enough deposit was collected from [PMPip][TFSI] at the lowest potential of -1.2 V. Physical properties of the ILs, listed in Table 8, indicate that at room temperature the viscosity of [PMPip][TFSI] is the greatest among the three ILs. It is possible this could be affecting mass transfer to the electrode despite operating at elevated temperature in an effort to reduce the viscosity of the ILs

and boost diffusion coefficients. The wider electrochemical windows afforded by $[Me_3N^nBu][TFSI]$ and [PMPip][TFSI], however, allow for better deposition and separation at the more negative potentials of -2.0 V and -2.8 V.

**Table 9.** ICP-AES results presented as U:Nd ratios for each of the repeated electrodeposits at each potential (-1.2 V, -2.0 V, and -2.8 V) for the three ILs. The initial ration of U:Nd was also determined from extractions. A separation factor (SF) is calculated.

| [EMIM][TFSI] | | | | | | |
|---|---|---|---|---|---|---|
| initial U:Nd ratio | E = -1.2 V | | E = -2.0 V | | E = -2.8 V | |
| | U:Nd ratio | **SF** | U:Nd ratio | **SF** | U:Nd ratio | **SF** |
| 1.50 | 5.98 | **3.99** | 4.65 | **3.10** | 7.17 | **4.78** |
| 1.50 | 3.60 | **2.40** | 6.38 | **4.26** | 0.90 | **0.60** |
| 1.50 | 3.96 | **2.64** | 10.33 | **6.88** | 1.24 | **0.82** |
| 1.50 | 5.10 | **3.40** | 3.70 | **2.47** | 1.08 | **0.72** |
| Avg ± st dev | 4.66 ± 1.09 | **3.11 ± 0.73** | 6.27 ± 2.93 | **4.18 ± 1.95** | 2.60 ± 3.05 | **1.73 ± 2.04** |
| $[Me_3N^nBu][TFSI]$ | | | | | | |
| initial U:Nd ratio | E = -1.2 V | | E = -2.0 V | | E = -2.8 V | |
| | U:Nd ratio | **SF** | U:Nd ratio | **SF** | U:Nd ratio | **SF** |
| 1.49 | 7.88 | **5.29** | 18.14 | **12.18** | 4.81 | **3.22** |
| 1.49 | 11.93 | **8.01** | 14.70 | **9.87** | 4.07 | **2.73** |
| 1.49 | 6.84 | **4.59** | 7.39 | **4.96** | 1.53 | **1.03** |
| 1.49 | 12.79 | **8.58** | 7.61 | **5.11** | 14.29 | **9.59** |
| Avg ± st dev | 9.86 ± 2.94 | **6.62 ± 1.97** | 11.96 ± 5.34 | **8.03 ± 3.59** | 6.18 ± 5.59 | **4.14 ± 3.75** |
| [PMPip][TFSI] | | | | | | |
| initial U:Nd ratio | E = -1.2 V | | E = -2.0 V | | E = -2.8 V | |
| | U:Nd ratio | **SF** | U:Nd ratio | **SF** | U:Nd ratio | **SF** |
| 1.48 | Needs re-analysis | **----** | 16.97 | **11.47** | 7.66 | **5.18** |
| 1.48 | not enough deposit | ---- | 23.84 | **16.11** | 25.60 | **17.30** |
| 1.48 | not enough deposit | ---- | 12.19 | **8.24** | 10.38 | **7.02** |
| 1.48 | not enough deposit | ---- | 16.17 | **10.93** | 32.41 | **21.90** |
| Avg ± st dev | ---- | ---- | 17.29 ± 4.84 | **11.69 ± 3.27** | 19.01 ± 11.92 | **12.85 ± 8.05** |

Significant variance was apparent within the repetitive attempts to deposit from portions of the same IL sample at the same potential. One possible cause could be water content because all electrochemistry was performed under ambient bench-top conditions. Attempts were made to minimize water in the IL sample prior to setting up an electrodeposit through rotovaping. However, the water content of the sample may have increased by ambient exposure during the 12 hour deposits. While the presence of water may not inhibit deposition completely, it could present a competing reaction of hydrogen evolution at these potentials and therefore reduce the amount of deposit and influence the final deposit product. Literature also reinforces that as water content of ILs increases, the electrochemical window decreases and eventually could limit potential driven reactions.[70] Much like applying temperature, water in the IL could have the benefit of reducing viscosity which should increase mass transfer and diffusion coefficients. However, the benefits of these effects may not outweigh the limitation provided on the electrochemical window and water hydrolysis side reactions competing with electrodeposition. It was not within the scope of the work or within the capabilities of the lab to operate inside of an inert atmosphere glovebox for these studies.

Further optimization of electrodeposition from the IL system may provide even better and reproducible separation. Some suggestions would be to better control the water content of the ILs, whether pH may enhance deposition through the addition of HTFSI. Additionally, the three potentials (-1.2 V, -2.0 V, and -2.8 V) were chosen to study the deposits and separation of uranium from the U/Nd mixture in each of the ILs, but further studies are needed in order to determine whether another potential perhaps between -2.0 V and -2.8 V may provide even better deposition and separation.

## 6.5 Conclusions

The results of this initial study on the ability to separate uranium from neodymium provide evidence that electrochemical separation is possible. While UV-Vis spectroscopy was attempted and able to qualitatively compare the concentrations of uranium and neodymium initially within the ILs and within dissolved electrodeposits, quantitative determinations were made difficult due to limited obtained deposit and absorbance interferences from dissolved Cu and possible IL degradation. Therefore, ICP-AES was used to provide quantitative determination of the effectiveness of the electrochemical deposits and separation. Of the three ILs investigated, the $[Me_3N^nBu][TFSI]$ and [PMPip][TFSI] resulted in the best separation, with the highest obtained SF being 21.90 from [PMPip][TFSI] at -2.8 V. The [EMIM][TFSI] also resulted in separation of the U from Nd, but the SF were not as high and the shorter electrochemical window was apparent with increased degradation of the IL at -2. 8 V. However, there was a large amount of variance of the resulting deposits and apparent separation of uranium from neodymium among the four replicates for each potential. Consequently, there is still work to be done towards optimization of the electrodeposition to achieve optimal separation as well as overall recovery and reproducibility. The overall results highlight the ability to separate actinides such as uranium from lanthanides within ILs based upon differences in reduction potentials.

# Chapter 7 – Conclusions

The unique physical properties of ILs have widened their utility in various aspects of chemistry and encouraged further research. Applications to the nuclear fuel cycle have been proposed but further research is needed in a number of areas to evaluate the potential for robust nuclear technology.[6] One proposed process incorporates using the IL to electrochemically separate and recover species from dissolved used fuel. However, the research thus far has been limited. Further studies of the parameters associated with electrochemistry for non-aqueous reprocessing such as viscosity, conductivity, electrochemical windows, kinetics of electron transfer, and methods to dissolve used nuclear fuel into IL were areas of suggested focus.

This work has contributed to an increased understanding of methods for the the direct dissolution and electrochemistry of f-elements in ILs. First, the electrochemical effect of water and acid in the IL as well as any potential effects on the stability of the $Ag/Ag^+$ non-aqueous reference electrode were investigated. The inclusion of secondary species such as water and acid in second generation ILs can reduce the potential window and produce side reactions that convolute the electrochemical analysis of other soluble species. The cyclic voltammetry of ferrocene in the IL containing water and acid demonstrates that the junction potential of the reference electrode does not change appreciably. Therefore, as long as the reference electrode used is checked for its response with ferrocene and effective offset potential on a consistent basis, the inclusion of water or the HTFSI acid will not introduce other potential problems associated with the electrochemical system.

Additionally, it was found that cathodic stripping analysis of the reduction of gold oxide, $Au_2O_3$, provides an in-situ electrochemical method to quantitatively measure the water

concentration, with a linear range between 0.09 – 0.74 wt % for the IL, $[Me_3N^nBu][TFSI]$, as a function of either the reduction peak current ($I_{pc}$) or charge under the peak ($Q_c$). The electrochemical formation of bulk gold oxide remains constant and independent of water concentration in excess of 0.74 wt % in the IL. However, cathodic stripping analysis could also be a useful qualitative tool for monitoring water in the IL for concentrations that are outside the linear range. Purging IL solutions with dry nitrogen gas or treatment with molecular sieves are effective in reducing the water concentration to background levels. If acid was used during dissolution, the remaining proton can be neutralized with a base such as ammonium hydroxide and then the sample can purged to reduce the water concentration below the background level for the IL prior to use to minimize their impact in subsequent electrochemical measurements.

The direct dissolution of $(Ce_2(CO_3)_3 \cdot xH_2O)$ into protic IL $[Me_3N^nBu][TFSI]$ containing the conjugate acid, HTFSI, was demonstrated. The direct dissolution is achieved through the formation and decomposition of carbonic acid with subsequent degassing to remove $CO_2$ and water from the IL. This approach minimizes the inclusion of additional chemical species in the IL to promote coordination between soluble Ce and the TFSI ligand. Electronic transitions in the UV range are consistent with the formation of Ce/TFSI complexes and indicative of ligand-to-metal charge transfer complexes. Finally, changes in the absorbance intensities of IR vibrational bands associated with the sulfonyl oxygen are also indicative of the coordination between TFSI and soluble Ce.

Electrochemical analysis of soluble Ce in $[Me_3N^nBu][TFSI]$ was performed at electrodes including Au, Pt, and GC. The multi-wave voltammetry observed for all three electrodes suggests that the deposition of Ce species proceeds through and reductive loss of TFSI at the electrode surface. The deposition of Ce species at all three electrodes occurs at potentials more

positive than the reduction potential in aqueous solutions. The deposition of Ce species at Au was visualized using SEM and confirmed with EDS analysis. The results for $Ce_2(CO_3)_3$ suggests that the protic IL can be used to increase solubility of other trivalent lanthanide carbonate species through direct dissolution. Additional studies are needed to confirm the soluble Ce species produced from the direct dissolution of $Ce_2(CO_3)_3$ in IL using HTFSI. Finally, bulk electrolysis of Ce from IL should be performed to provide bulk deposits for more thorough examination to determine if the initial deposit is Ce metal or oxide.

As the largest component of nuclear fuel, studies of the soluble species of uranium in the IL and electrochemistry and electrodeposits were of interest. Direct dissolution of $UO_2CO_3$(s) in IL $[Me_3N^nBu][TFSI]$ containing water and HTFSI was first demonstrated to investigate the spectroscopy and electrochemistry of the soluble uranium species in the IL. The direct dissolution and solubility of $UO_2CO_3$(s) was increased from 5 mM to 50 mM with the addition of HTFSI and water indicating that the solubility is enhanced through the increased dissociation of the acid allowing for proton facilitated displacement of carbonate.

Used nuclear fuel however is often encountered as an oxide ($UO_2$). To reduce reprocessing steps and handling, a method to directly dissolve the oxide would be preferred. Dissolution of an oxide, $U_3O_8$, required the use of oxidizing gas. The dissolution was attempted using various gases including air, $N_2$, $O_2$, and $N_2O$. However, only air feed gas to an ozone generator was successful in achieving dissolution. The dissolution mechanism therefore remains unknown, but may include ozone in combination with another nitrogen or oxygen based oxidizing gas or gas radical. Studies of the dissolution determined that HTFSI acid was not necessary, however further studies are needed to understand if adding acid, such as HTFSI, allows for increased deposition.

The UV-Vis data suggests that $UO_2^{2+}$ is the soluble species and in the IL solution as well as in water. In addition, the soluble $UO_2^{2+}$ was evaluated electrochemically in the presence of water and HTFSI acid and the reduction of U(VI) to form the stable intermediate U(V) was resolved. Additional reduction processes were elucidated and attributed to the two electron reduction of $UO_2^{2+}$ to $UO_2$ and the subsequent deposition of uranium oxide species at the electrode surface were identified using SEM and EDS analysis. Finally, the methods detailed provide pathways for increasing the solubility of actinide or lanthanide carbonates and oxides into ILs.

Lastly, the results of the initial study on the ability to separate uranium from a lanthanide (neodymium) provide evidence that electrochemical separation through electrodeposition from the IL is possible. Quantitative determinations were made difficult due to limited obtained deposit and absorbance interferences from dissolved Cu of the working electrode and possible IL degradation. Therefore, ICP-AES was used to provide quantitative determination of the effectiveness of the electrochemical deposits and separation. Of the three ILs investigated, the $[Me_3N^nBu][TFSI]$ and [PMPip][TFSI] resulted in the best separation, with the highest obtained SF being 21.90 from [PMPip][TFSI] at -2.8 V. The [EMIM][TFSI] also resulted in separation of the uranium from neodymium, but the SF were not as high and the shorter electrochemical window was apparent with increased degradation of the IL at -2. 8 V. However, there was a large amount of variance of the resulting deposits. Further work is needed for optimization of the electrodeposition to achieve separation as well as overall recovery and reproducibility. The overall results highlight the ability to separate actinides such as uranium from lanthanides within ILs based upon differences in reduction potentials.

This research demonstrates that ILs and electrochemical methods can be used for electrodeposition and recovery of f-elements. For applications to the nuclear fuel cycle, other actinides of interest (Pu, Np, and Am for example) also need to be investigated for their potentials of deposition within the ILs and recovery. If the deposition of the actinides occur at sufficiently less positive potentials compared to the lanthanides, as was observed in the case of uranium and neodymium, perhaps a sequential series of potentials could be applied at increasingly negative potentials to group electrodeposit and separate the fission products, actinides, and lanthanides in series.

References

[1] U.S. Nuclear Regulatory Commission Radioactive Waste: Production, Storage, Disposal. NUREG/BR-0216, Rev.2 May 2002

[2] Neeb, K. H. (1997). *The Radiochemistry of Nuclear Power Plants with Light Water Reactors.* New York: Walter de Gruyter.

[3] Guenther, E. A. (1991). *Characterization of Spent Fuel Approved Testing Material ATM-105*. PNL-5109-105. Richland Washington: PNL.

[4] Wilson, P. D. (1996) The Nuclear Fuel Cycle: From Ore to Waste. New York, Oxford University Press.

[5] World Nuclear Association. "Chemistry of Purex" www.world-nuclear.org/info/Nuclear-Fuel-Cycle/Fuel-Reprocessing/Processing-of-Used-Nuclear-Fuel/. Accessed October 19, 2015.

[6] Venkatesan, K. A.; Srinivasan, T. G.; Vasudeva Rao, P. R. (2009) A review on the electrochemical applications of room temperature ionic liquids in nuclear fuel cycle. *J. Nuc. Rad. Sci*. **10**, R1-R6.

[7] Visser, A. E.; Rogers, R. D. (2003) Room-temperature ionic liquids: new solvents for f-element separations and associated solution chemistry. *J. Solid State Chem*. **171**, 109-113.

[8] Dietz, M. L. (2006) Ionic liquids as extraction solvents: where do we stand? *Sep. Sci Technol.* **41**, 2047-2063.

[9] Billard, I.; Ouadi, A.; Gaillard, C. (2011) Liquid–liquid extraction of actinides, lanthanides, and fission products by use of ionic liquids: from discovery to understanding. *Anal. Bioanal. Chem.* **400**, 1555-1566.

[10] Walden, P. (1914) Molecular weights and electrical conductivity of several fused salts. *Bull. Acad. Imper. Sci.* St. Petersburg, 405-422.

[11] Hurley, F. H.; Wier Jr., T. P. (1951) Electrodeposition of metals from fused quaternary ammonium salts. *J. Electrochem. Soc.* **98**, 203-206.

[12] Gale, R. J.; Gilbert, B.; Osteryoung, R. A. (1978) Raman spectra of molten aluminum chloride: 1-butylpyridinium chloride systems at ambient temperatures. *Inorg. Chem*. **17**, 2728-2729.

[13] Wilkes, J. S.; Zaworotko, M. J. (1992) Air and water stable 1-ethyl-3-methylimidazolium based ionic liquids. *J. Chem. Soc. Chem. Commun*. **13**, 965-967.

[14] Kiekens, P., Steen, L., Donche, H., Temmerman, E. (1981) Kinetics of cerium(IV) reduction at gold, carbon, and iridium electrodes. *Electrochim. Acta*. **26**, 841- 845.

[15] Bhatt, A. I.; Duffy, N. W.; Collison, D.; May, I.; Lewin, R. G. (2006) Cyclic Voltammetry of Th(IV) in the Room-Temperature Ionic Liquid $[Me_3N^nBu][N(SO_2CF_3)_2]$ *Inorg. Chem*. **45**, 1677-1682.

[16] Bhatt, A. I.; May, I.; Volkovich, V. A.; Collison, D.; Helliwell, M.; Polovov, I. B.; Lewin, R. G. (2005) Structural Characterization of a Lanthanum Bistriflimide Complex, $La(N(SO_2CF_3)_2)$ $3(H_2O)_3$, and an Investigation of La, Sm, and Eu Electrochemistry in a Room-Temperature Ionic Liquid, $[Me_3N^nBu][N(SO_2CF_3)_2]$. *Inorg. Chem.* **44**, 4934- 4940.

[17] Nockemann, P.; Thijs, B.; Parac-Vogt, T. N.; Van Hecke, K.; Van Meervelt, L.; Tinant, B.; Hartenbach, I.; Schleid, T.; Ngan, V. T.; Nguyen, M. T.; Binnemans, K. (2008) Carboxyl-Functionalized Task-Specific Ionic Liquids for Solubilizing Metal Oxides. *Inorg. Chem.* **47,** 9987- 9999.

[18] Rao, Ch. Jagadeeswara; Venkatesan, K. A.; Nagarajan, K.; Srinivasan, T. G. (2008) Dissolution of uranium oxides and electrochemical behavior of U(VI) in task specific ionic liquid. *Radiochim. Acta.* **96**, 403-409.

[19] Nockemann, P.; Thijs, B.; Pittois, S.; Thoen, J.; Glorieux, C.; Van Hecke, K.; Van Meervelt, L.; Kirchner, B.; Binnemans, K. (2006) Task-specific ionic liquid for solubilizing metal oxides. *J. Phys. Chem. B.* **110**, 20978-20992.

[20] Susan, A. B. H. Md.; Noda, A.; Mitsushima, S.; Watanabe, M. (2003) Bronsted acid-base ionic liquids and their use as new materials for anhydrous proton conductors. *Chem. Comm.* **8**, 938-939.

[21] Robert, T.; Magna, L.; Olivier-Bourbigouand, H.; Gilbert, B. (2009) A comparison of acidity levels in room-temperature ionic liquids. *J. Electrochem. Soc*. 2009, **156**, F115-F121.

[22] D'Anna, F.; Marca, S. L.; Noto, R. (2009) p-Nitrophenolate: A Probe for Determining Acid Strength in Ionic Liquids. *J. Org. Chem*. **74**, 1952-1956.

[23] Lohrengel, M. M.; Schultze, J. W. (1976) Electrochemical properties of anodic gold oxide layers. I. Potentiostatic oxide growth and double layer capacity. *Electrochim. Acta* **21**, 957-965.

[24] Lide, D. R. (Ed.), (2004) CRC Handbook of Chemistry and Physics, 85th ed., CRC Press.

[25] Brennan, M. P. J.; Brown, O. R. (1972) Carbon electrodes. 1. Hydrogen evolution in acidic solution. *J. Applied. Echem*. **2,** 43-49.

[26] Bard, A. J.; Parsons, R.; Jordan, J. (1985) Standard Potentials in Aqueous Solution, Marcel Dekker, Inc., New York, NY.

[27] Conway, B. E.; Wilkinson, D. P. (1988) Broensted relationships for heterogeneous proton transfer at electrode interfaces. *J. Chem. Soc., Faraday Trans*. **184**, 3389-3400.

[28] Nugent, L. J. (1975) Standard electrode potentials and enthalpies of formation of lanthanide and actinide aquo-ions. *J. Inorg. Nucl. Chem.* **37**, 1767-1770.

[29] Samhoun, K.; David, F. (1979) Electrochemical reduction by radiopolarography of some transplutonium aqueous ions. *J. Inorg. Nucl. Chem*. **41,** 357-363.

[30] Heyrovska, R. (2001) An estimation of the ionization potentials of actinides from a simple dependence of the aqueous standard potentials on the ionization potentials of elements including lanthanides. *J. Alloys Comp.* **323-324**, 614-617.

[31] Capdevila, H.; Vitorge, P. (1990) Temperature and ionic strength influence on uranium(VI/V) and uranium(IV/III) redox potentials in aqueous acidic and carbonate solutions. *J. Radioanal. Chem.* **143**, 403-414.

[32] Tryambake, M. U.; Kuchekar, B. S.; Chabukswar, A. R.; Lokhande, P. D.; Kadam, V. J.; Tryambake, M. B. (2011) A review on ionic liquids. *Int. J. Curr. Res. Rev.* **3**, 11-20.

[33] Buzzeo, M. C.; Hardacre, C.; Compton, R. G. (2006) Extended electrochemical windows made accessible by room temperature ionic liquid/organic solvent electrolyte systems. *ChemPhysChem* **7**, 176-180.

[34] Buzzeo, M. C.; Evans, R. G.; Compton, R. G. (2004) Non-haloaluminate room-temperature ionic liquids in electrochemistry-a review. *ChemPhysChem* **5**, 1106-1120.

[35] Howlett, P. C.; Izgorodina, E. I.; Forsyth, M.; MacFarlane, D. R. (2006) Electrochemistry at negative potentials in bis(trifluoromethanesulfonyl)amide ionic liquids. *Z. Phys. Chem* **220**, 1483-1498.

[36] Sun, J.; Forsyth, M.; MacFarlane, D. R. (1998) Room-temperature molten salts based on the quaternary ammonium ion. *J. Phys. Chem. B* **102**, 8858-8864.

[37] Schoebrechts, J. P.; Gilbert, B. P.; Duyckaerts, G. (1983) Electrochemical and spectroscopic studies of the lanthanides in the aluminum chloride + 1-n-butylpyridinium chloride melt at 40°C. Part II. The thulium(III-II), europium(III-II) systems, application of Nugent's linearization method. *J. Electroanal. Chem*. **145**, 139-146.

[38] Yamagata, M.; Katayama, Y.; Miura, T. (2006) Electrochemical Behavior of Samarium, Europium, and Ytterbium in Hydrophobic Room-Temperature Molten Salt Systems. *J. Electrochem. Soc*. **153,** E5- E9.

[39] Schoebrechts, J. P.; Gilbert, B. P.; Duyckaerts, G. (1983) Electrochemical and spectroscopic studies of the lanthanides in the aluminum chloride + 1-n-butylpyridinium chloride melt at 40°C. Part I. The ytterbium(III-II), samarium(III-II) systems. *J. Electroanal. Chem*. **145**, 127-138.

[40] Lodermeyer, J.; Multerer, M.; Zistler, M.; Jordan, S.; Gores, H. J.; Kipferl, W.; Diaconu, E.; Bayreuther, G. (2006) Electroplating of Dysprosium, Electrochemical Investigations, and Study of Magnetic Properties. *J. Electrochem. Soc*. **153**, C242-C248.

[41] Dietz, M. L.; Stepinski, D. C. (2008) Anion concentration-dependent partitioning mechanism in the extraction of uranium into room-temperature ionic liquids. *Talanta* **75**, 598-603.

[42] Dietz, M. L.; Dzielawa, J. A. (2001) Ion-exchange as a mode of cation transfer into room-temperature ionic liquids containing crown ethers: implications for the 'greenness' of ionic liquids as diluents in liquid-liquid extraction. *Chem. Comm*. **20**, 2124-2125.

[43] Huddleston, J. G.; Willauer, H. D.; Swatloski, R. P.; Vissser, A. E.; Rogers, R. D. (1998) Room temperature ionic liquids as novel media for 'clean' liquid–liquid extraction. *Chem. Comm*. **16**,1765-1766.

[44] Giridhar, P.; Venkatesan, K. A.; Subramaniam, S.; Srinivasan, T. G.; Rao, P. R. V. (2008) Extraction of uranium (VI) by 1.1M tri-n-butylphosphate/ionic liquid and the feasibility of recovery by direct electrodeposition from organic phase. *J. Alloys Comp.* **448**, 104-108.

[45] Giridhar, P.; Venkatesan, K. A.; Srinivasan, T. G.; Rao, P. R. V. (2005) Extraction of uranium(VI) from nitric acid medium by 1.1M tri-n-butylphosphate in ionic liquid diluent. *J. Radioanal. Nucl. Chem.* **265**, 31-38.

[46] Zuo, Y.; Liu, Y.; Chen, J.; Li, D. Q. (2008) The Separation of Cerium(IV) from Nitric Acid Solutions Containing Thorium(IV) and Lanthanides(III) Using Pure $[C_8mim]PF_6$ as Extracting Phase. *Ind. Eng. Chem. Res.* **47**, 2349-2355.

[47] Lohithakshan, V. K.; Aggarwal, K. S. (2008) Solvent extraction studies of Pu(IV) with CMPO in 1-octyl 3-methyl imidazolium hexa fluorophosphate (C8mimPF6) room temperature ionic liquid (RTIL). *Radiochim. Acta* **96**, 93-97.

[48] Hermann, S. D.; Li, S. X. (2010) Separation and recovery of uranium metal from spent light water reactor fuel via electrolytic reduction and electrorefining. *Nucl. Techol.***171**, 247-265.

[49] Willit, J. L.; Miller, W. E.; Battles, J. E. (1992) Electrorefining of uranium and plutonium – A literature review. *J. Nucl. Mat.* **195**, 229-249.

[50] Li, Y.; Zhou, T.; Zhou, K.; Liu, Y.; Liu, F.; Zhang, F. (2004) A new corrosion-resistant material for use as an inert anode in electrolytic molten salt aluminum extraction systems. *Anti-Corr. Meth. Mat.***51**, 25-30.

[51] Antoniou, S.; Kolokassidou, C.; Polychronopoulou, K.; Pashalidis, I. (2009) Effect of humic acid on the solid phase stability of $UO_2CO_3$. *J. Radioanal. Nucl. Chem*. **279**, 863-866.

[52] Meinrath, G.; Kimura, T. (1993) Behavior of uranium (VI) solids under conditions of natural aquatic systems. *Inorg. Chim. Acta* **204**, 79-85.

[53] Meinrath, G.; Kimura, T. J. (1993) Carbonate Complexation of the Uranyl (VI) Ion. *J. Alloys Compd.* **202**, 89-93.

[54] Chernorukov, N.G.; Knyazev, A.V.; Knyazeva, M.A.; Sergacheva, I.V. (2002) Synthesis, Structure, and Physicochemical Characteristics of Rutherfordine and Tetrasodium Uranyl Tricarbonate. *Radiochem*. **44**, 212-215.

[55] Finch, R.J.; Cooper, M.A.; Hawthorne, F.C. (1999) Refinement of the crystal structure of rutherfordine. *The Canadian Mineralogist* **37**, 929-938.

[56] Loopstra, B. O. (1977) On the Crystal Structure of α uranium oxide ($\alpha$-$U_3O_8$) *J. Inorg. Nucl. Chem.* **39**, 1713-1714.

[57] Babai, A.; Mudring, A. (2006) The first homoleptic bis(trifluoromethanesulfonyl)amide complex compounds of trivalent f-elements. *Dalton Trans.* **15**, 1828-1830.

[58] Nockemann, P.; Van Deun, R.; Thijs, B.; Huys, D.; Vanecht, E.; Van Hecke, K.; Van Meervelt, L.; Binnemans, K. (2010) Uranyl Complexes of Carboxyl-Functionalized Ionic Liquids. *Inorg. Chem*. **49**, 3351-3360.

[59] Ozone Solutions Inc. OZV-8 Ozone Generator Installation and Operation Manual.

[60] Skoog, D.; Holler, F. (2006). *Principles of Instrumental Analysis*, 6th ed. Canada: Thomson Learning.

[61] Knoll, G.F. (2000). *Radiation Detection and Measurement*. 3rd. Hoboken, NJ: John Wiley & Sons, Inc.

[62] *Tri-Carb 3110TR Low Activity Liquid Scintillation Analyzer* (2009). Waltham, MA: Perkin Elmer Inc.

[63] *LSC in Practice: Counting Aqueous Samples by LSC* (2008). Waltham, MA: Perkin Elmer Inc.

[64] Gordon, C.; Rohner, R. (2005.) *Fundamentals of the Coulometric Karl Fischer Titration with Selected Applications. Mettler Toledo Titrators DL32/DL39* Applications Brochure 32. Switzerland:Mettler-Toledo GmbH

[65] Saheb, A.; Janata, J.; Josowicz, M.(2006) Reference electrode for ionic liquids. *Electroanalysis* **18**, 405-409.

[66] ChemWiki: The Dynamic Chemistry Hypertext. 11D:Voltammetric Methods. http://chemwiki.ucdavis.edu/Analytical_Chemistry/Analytical_Chemistry_2.0/11_Electrochemical_Methods/11D%3A_Voltammetric_Methods

[67] Bard, A. J.; Faulkner, L. R. (2001). *Electrochemical Methods: Fundamentals and Applications,* 2nd ed., New York: John Wiley & Sons, Inc.

[68] Zawodzinski, T.A.; Osteryoung, R. A. (1990) Oxide and hydroxide species formed on addition of water in ambient-temperature chloroaluminate melts: an oxygen-17 NMR study. *Inorg. Chem.* **29**, 2842-2847.

[69] Handy, T. S. (2005) Room temperature ionic liquids: Different classes and physical properties. *Current Org. Chem.* **9**, 959-988.

[70] O'Mahony, A. M.; Silvester, D. S.; Aldous, L.; Hardacre, C.; Compton, R. G. (2008) Effect of Water on the Electrochemical Window and Potential Limits of Room-Temperature Ionic Liquids. *J. Chem. Eng. Data.* **53**, 2884-2891.

[71] Randtroem,, S.; Montanino, M.; Appetecchi, G. B.; Lagergren, C.; Moreno, A.; Passerini, S. (2008) Effect of water and oxygen traces on the cathodic stability of N-alkyl-N-methylpyrrolidinium bis(trifluoromethanesulfonyl)imide. *Electrochim. Acta*. **53**, 6397-6401.

[72] Rollet, A. L.; Porion, P.; Vaultier, M.; Billard, I.; Deschamps, M.; Bessada, C.; Jouvensal, L. (2007) Anomalous Diffusion of Water in [BMIM][TFSI] Room-Temperature Ionic Liquid. *J. Phys. Chem. B.* **111**, 11888-11891.

[73] Li, J.; Zhang, J. ; Han, B.; Zhao, Y.; Yang, G. (2012) Formation of multiple water-in-ionic liquid-in-water emulsions. *J. Colloid Inter. Sci*. **368**, 395-399.

[74] Widegren, J. A.; Saurer, E. M.; Marsh, K. N.; Magee, J. W. (2005) Electrolytic conductivity of four imidazolium-based room-temperature ionic liquids and the effect of a water impurity. *J. Chem. Thermodyn*. **37**, 569-575.

[75] Zhao, C.; Bond, A. M.; Lu, X. (2012) Determination of Water in Room Temperature Ionic Liquids by Cathodic Stripping Voltammetry at a Gold Electrode. *Anal. Chem.* **84**, 2784-2791.

[76] Tran, C. D.; De Paoli Lacerda, S. H.; Oliveira, D. (2003) Absorption of water by room-temperature ionic liquids: Effect of anions on concentration and state of water. *Appl. Spect.* **57**, 152-157.

[77] Zuliani, C.; Walsh, D. A.; Keyes, T. E.; Forster, R. J. (2010) Formation and Growth of Oxide Layers at Platinum and Gold Nano- and Microelectrodes. *Anal Chem*. **82**, 7135-7140.

[78] Pemberton, W. J.; Droessler, J. E.; Kinyanjui, J. M.; Czerwinski, K. R.; Hatchett, D. W. (2013) Electrochemistry of soluble UO22+ from the direct dissolution of UO2CO3 in acidic ionic liquid containing water. *Electrochim. Acta*. **93**, 264-271.

[79] Hatchett, D. W.; Droessler, J.; Kinyanjui, J. M.; Martinez, B.; Czerwinski,K. R. (2013) The direct dissolution of Ce2(CO3)3 and electrochemical deposition of Ce species using ionic liquid trimethyl-n-butylammonium bis(trifluoromethanesulfonyl)imide containing bis(trifluoromethanesulfonyl)imide. *Electrochim. Acta*. **89**, 144-151.

[80] Thomazeau, C.; Olivier-Bourbigouand, H.; Magna, L.; Luts, S.; Gilbert, B. (2003) Determination of an Acidic Scale in Room Temperature Ionic Liquids. *J. Am. Chem. Soc*. **125**, 5264-5265.

[81] Aldous, L.; Silvester, D. S.; Pitner, W. R.; Compton, R. G.; Lagunas, M. C.; Hardacre, C. (2007) Voltammetric Studies of Gold, Protons, and [HCl2]- in Ionic Liquids. *J. Phys. Chem. C*. **111**, 8496-8503.

[82] Tremiliosi-Filho, G.; Dall'Antonia, L. H.; Jerkiewicz, G. (1997) Limit to extent of formation of the quasi-two-dimensional oxide state on Au electrodes. *J. Electroanal. Chem*. **422**, 149-159.

[83] Blahusaik, M.; Schlosser, S. (2014) Physical properties of phosphonium ionic liquid and its mixtures with dodecane and water. *J. Chem. Thermodyn.* **72**, 54-64.

[84] Silvester, D. S.; Aldous, D.; Hardacre, C.; Compton, R. G. (2007) An Electrochemical Study of the Oxidation of Hydrogen at Platinum Electrodes in Several Room Temperature Ionic Liquids. *J. Phys. Chem. B*. **111**, 5000-5007.

[85] Goffart, G. (1948) Titrimetry of cerous ions by permanganate. *Anal. Chim. Acta*. **2**, 140-145.

[86] Desideri, P. G. (1961) The polarographic behavior of cerium(IV) and cerium(IV)-cerium(III) system in sulfuric media. Direct determination of cerium(IV). *J. Electroanal. Chem.* **2**, 39-45.

[87] Kunz, A. H. (1931) The reduction potential of the ceric-cerous electrode. *J. Am. Chem. Soc.* **53**, 98-102.

[88] Greef, R.; Aulich, H. (1968) The kinetics of the cerous-ceric redox reaction at a platinum electrode. *J. Electroanal. Chem.* **18**, 295-307.

[89] Galus, Z.; Adams, R. N. (1963) The investigation of the kinetics of moderately rapid electrode reactions using rotating disk electrodes. *J. Phys. Chem.* **67**, 866-871.

[90] Randle, T. H.; Kuhn, A. T. (1983) Kinetics and mechanism of the cerium(IV)/cerium(III) redox reaction on a platinum electrode. *J. Chem. Soc., Faraday Trans. I* **79**, 1741-1756.

[91] Bonewitz, R. A.; Schmid, G. M. (1970) Oxygen adsorption on gold and the cerium(III) /cerium(IV) reaction. *J. Electrochem. Soc.* **117**, 1367- 1372.

[92] Lewicka, G.; Sykut, K. (1980) Specific reduction of rare earth metals on the dropping mercury electrode in the presence of nickel. *Annales Universitatis Mariae Curie-Sklodowska, Section AA: Chemia*, **31-32**, 123-129.

[93] Lunstroot, K.; Nockemann, P.; Van Heck, K.; Van Meervelt, L.; Gorller-Walrand, C.; Binnemans, K.; Driesen, K. (2009) Visible and Near-Infrared Emission by Samarium(III)-Containing Ionic Liquid Mixtures. *Inorg. Chem.* **48**, 3018-3026.

[94] Varlashkin, P. G. (1985) Spectroscopic and electrochemical studies of selected lanthanides and actinides in concentrated aqueous carbonate and carbonate-hydroxide solutions and in molten dimethyl sulfone. Ph.D. dissertation, University of Tennessee, Knoxville.

[95] Zhang, T.; Guo, H.; Qiao, Y. (2009) Facile synthesis, structural and optical characterization of LnF3:Re nanocrystals by ionic liquid-based hydrothermal process. *J. Lumin.* **129**, 861-866.

[96] Herstedt, M.; Smirnov, M.; Johansson, P.; Chami, M.; Grondin, J.; Servant, L.; Lassegues, J. C. (2005) Spectroscopic characterization of the conformational states of the bis(trifluoromethanesulfonyl)imide anion (TFSI−). *J. Raman Spec.* **36**, 762-770.

[97] Hoefft, O.; Bahr, S.; Kempter, V. (2008) Investigations with Infrared Spectroscopy on Films of the Ionic Liquid [EMIM]Tf2N. *Langmuir* **24**, 11562-11566.

[98] Kiefer, J.; Fries, J.; Leipertz, A. (2007) Experimental Vibrational Study of Imidazolium-Based Ionic Liquids: Raman and Infrared Spectra of 1-Ethyl-3-methylimidazolium Bis(trifluoromethylsulfonyl)imide and 1-Ethyl-3-methylimidazolium Ethylsulfate. *J. Appl. Spec.* **61**, 1306-1311.

[99] Rey, I.; Johansson, P.; Lindgren, J.; Lassegues, J. C.; Grondin, J.; Servant, L. (1998) Spectroscopic and Theoretical Study of $(CF_3SO_2)_2N^-$ ($TFSI^-$) and $(CF_3SO_2)_2NH$ (HTFSI). *J. Phys. Chem. A 102*, 3249-3258.

[100] Solvionic. http://en.solvionic.com/files/solvionic/spectre_ir/Am0408b.pdf (accessed Feb. 20, 2012).

[101] Mudring, A.; Babai, A.; Arenz, S.; Giernoth, R. (2005) The "Noncoordinating" Anion $Tf_2N^-$ Coordinates to $Yb^{2+}$: A Structurally Characterized $Tf_2N^-$ Complex from the Ionic Liquid [mppyr][$Tf_2N$]. *Angew. Chemie. Int. Ed.* **44**, 5485-5488.

[102] Williams, D. B.; Stoll, M. E.; Scott, B. L.; Costa, D. A.; Oldham, W. J. (2005) Coordination chemistry of the bis(trifluoromethylsulfonyl)imide anion: molecular interactions in room temperature ionic liquids. *Chem. Comm.* **11**, 1438-1440.

[103] Thompson, A.; Attwood, D.; Gullikson, E.; Howells, M.; Kim, K.; Kirz, J.; Kortright, J.; Lindau, I.; Liu, Y.; Pianetta, P.; Robinson, A.; Scofield, J.; Underwood, J.; Williams, G.; Winick, H. "X-ray Data Booklet" Center for X-ray Optics and Advanced Light Source. October 2009 ed. http://xdb.lbl.gov/section1/Table_1-3.pdf (accessed Jan. 8, 2012).

[104] Constantin, V.; Popescu, A.; Zuca, S. (2003) Preliminary Studies of the Obtaining of Solid Metallic Cerium from Fluoride Melts. *Z. Naturforsch.* **58a**, 57-62.
[105] Binnemans, K. (2007) Lanthanides and Actinides in Ionic Liquids. *Chem. Rev.* **107**, 2592-2614.

[106] Galinski, M.; Lewandowski, A.; Stepniak, I. (2006) Ionic Liquids as Electrolytes. *Electrochim. Acta.* **51**, 5567-5580.

[107] Oldham, W. J.; J.; Costa, D. A.; Smith, W. H. Development of Room Temperature Ionic Liquids for Applications in Actinide Chemistry; Los Alamos National Laboratory: Division, Nuclear Materials Technology, 2001; p. 10.

[108] Cocalia, E. V. A.; Gutowski, K. E.; Rogers, R. O. (2006) The Coordination Chemistry of Actinides in Ionic Liquids: A Review of Experiment and Simulation. *Coord. Chem. Rev*. **250**, 755-764.

[109] Sakamura, Y.; Omori, T. (2010) Electrolytic Reduction and Electrorefining of Uranium to Develop Pyrochemical Reprocessing of Oxide Fuels. *Nucl. Technol.* **171**, 266-275.

[110] Paek, S.; Kim, S.-H.; Yoon, D.-S.; Ahn, D.-H. (2010) Performance of the Mesh-Type Liquid Cadmium Cathode Structure for the Electrodeposition of Uranium from the Molten Salt. *Radiochim. Acta.* **98**, 779-783.

[111] Gaillard, C.; Chaumont, A.; Billard, I.; Hennig, C.; Ouadi, A.; Wipff, G. (2007) Uranyl Coordination in Ionic Liquids: The Competition between Ionic Liquid Anions, Uranyl Counterions, and Cl- Anions Investigated by Extended X-ray Absorption Fine Structure and UV-Visible Spectroscopies and Molecular Dynamics Simulations. *Inorg. Chem.* **46**, 4815-4826.

[112] Nockermann, P.; Servaes, K.; Van Deun, R.; Van Hecke, K.; Van Meervelt, Binnemans, K.; Gorller-Walrand, C. (2007) Speciation of Uranyl Complexes in Ionic Liquids by Optical Spectroscopy. *Inorg. Chem.* **46**, 11335-11344.

[113] Billard, I.; Gaillard, C.; Hennig, C. (2007) Dissolution of $UO_2$, $UO_3$ and of Some Lanthanide Oxides in Bumim$Tf_2N$: Effect of Acid and Water and Formation of $UO_2(NO_3)_3^-$. *Dalton Trans.* **37**, 4214-4221.

[114] Billard, I.; Mekki, S.; Gaillard, C.; Hesemann, P.; Moutiers, G.; Mariet, C.; Bunzli, J.-C. G. (2004) EuIII Luminescence in a Hygroscopic Ionic Liquid: Effect of Water and Evidence for a Complexation Process. *Eur. J. Inorg. Chem*. **6**, 1190-1197.

[115] Kim, K. W.; Hyun, J. T.; Sung, S. R.; Lee, E. H.; Lee, K. W.; Song, K. C. (2010) Electrolytic Dissolution Characteristics of SIMFUEL in Carbonate Solutions of High Concentration. *J. Nucl. Mater*. **406**, 223-229.

[116] Kim, K. W.; Park, G. I.; Lee, E. H.; Lee, K. W.; Song, K. C. (2010) Electrolytic Dissolutions of $UO_2$ and SIMFUEL in Carbonate Solutions at Several pHs. *Int. J. Chem. Biochem. Eng.* **4**, 187-190.

[117] Pemberton, W. J.; Droessler, J.; Kinyanjui, J. M.; Czerwinski, K. R.; Hatchett, D. W. (2013) Electrochemistry of soluble $UO_2^{2+}$ from the direct dissolution of $UO_2CO_3$ in acidic ionic liquid containing water. *Electrochim. Acta,* **93**, 264-271.

[118] Gelis, V. M.; Shumilova, Y. V.; Ershov, B. G.; Maslennikov, A. G.; Mulyutin, V. V.; Seliverstov, A. F. (2011) Dissolution of Actinide Oxides in $HNO_3$ Using a Concentrated Ozone-Oxygen Mixture in the Presence of Ce(IV) Ions. *Radiochem.* **53**, 250-255.

[119] Morss, L. R.; Edelstein, N. M.; Fuger, J.; Katz, J. J.; Kirby, H. W.; Wolf, S. F.; Haire, R. G.; Burns, C. J.; Eisen, M. S. The Chemistry of the Actinide and Transactinide Elements; Third Edition; Springer Netherlands, 2006.

[120] Sornein, M. O.; Cannes, C.; Le Naour, C.; Lagarde, G.; Simoni, E.; Berthet, J. C. (2006) Uranyl Complexation by Chloride Ions. Formation of a Tetrachlorouranium(VI) Complex in Room Temperature Ionic Liquids [Bmim][$Tf_2N$] and [$MeBu_3N$][$Tf_2N$]. *Inorg. Chem*. **45**, 10419-10421.

[121] Gaillard, C.; Chaumont, A.; Billard, I.; Hennig, C.; Ouadi, A.; Georg, S.; Wipff, G. (2010) Competitive Complexation of Nitrates and Chlorides to Uranyl in a Room Temperature Ionic Liquid. *Inorg. Chem*. **49**, 6484-6494.

[122] Bernhard, G.; Geipel, G.; Brendler, V.; Nitsche, H. (1998) Uranium Speciation in Waters of Different Uranium Mining Areas. *J. Alloys Compd.*, **271**, 201-205.

[123] Sornein, M. O.; Mendes, M.; Cannes, C.; La Naour, C.; Nockemann, P.; Van Hecke, K.; Van Meervelt, L.; Berthet, J. C.; Hennig, C. (2009) Coordination Environment of $[UO_2Br_4]^{2-}$ in Ionic Liquids and Crystal Structure of $[Bmim]_2[UO_2Br_4]$. *Polyhedron* **28**, 1281-1286.

[124] Giridhar, P.; Venkatesan, K. A.; Subramaniam, S.; Srinivasan, T. G.; Vasudeva Rao, P. R. (2006) Electrochemical Behavior of Uranium(VI) in 1-butyl-3-methylimidazolium chloride and in 0.05 M Aliquat-336/chloroform. *Radiochim. Acta.* **94**, 415-420.

[125] Giridhar, P.; Venkatesan, K. A.; Srinivasan, T. G.; Vasudeva Rao, P. R. (2007) Electrochemical Behavior of uranium(VI) in 1-butyl-3-methylimidazolium chloride and Thermal Characterization of Uranium Oxide Deposit. *Electrochim. Acta.* **52**, 3006-3012.

[126] Selbin, J.; Ortego, J. D. (1969) Chemistry of Uranium (V). *Chem. Rev.* **69**, 657-661.

[127] Wander, M. C. F.; Shuford, K. L. (2012) A Theoretical Study of the Qualitative Reaction Mechanism for the Homogeneous Disproportionation of Pentavalent Uranyl Ions. *Geochim. Cosmochim. Acta.* **84**, 177-185.

[128] Smolenskii, V. V.; Bove, A. L.; Borodina, N. P.; Bychkov, A. V.; Osipenko, A. G. (2004) Behavior of $UO_2$ in a Room-Temperature Ionic Liquid in the Presence of $AlCl_3$. *Radiochem.* **46**, 583-586.

[129] Asanuma, N.; Harada, M.; Yasuike, Y.; Nogami, M.; Suzuki, K.; Ikeda, Y. (2007) Electrochemical Properties of Uranyl Ion in Ionic Liquids as Media for Pyrochemical Reprocessing. *J. Nucl. Sci. Technol*. **44**, 368-372.

[130] Herrmann, S. D.; Li, S. X. (2009) Separation and Recovery of Uranium Metal from Spent Light Water Reactor Fuel via Electrolytic Reduction and Electrorefining. *Nucl. Technol.* **171**, 247-265.

[131] Herrmann, S. D.; Li, S. X.; Westphal, B. R. (2012) Separation and Recovery of Uranium and Group Actinide Products from Irradiated Fast Reactor MOX Fuel via Electrolytic Reduction and Electrorefining. *Sep. Sci. Technol.* **47**, 2044- 2059.

[132] Kwon, S. W.; Ahn, D. H.; Kim, E. H.; Ahn, H. G. (2009) A Study on the Recovery of Actinide Elements from Molten LiCl-KCl Eutectic Salt by an Electrochemical Separation. *J. Ind. Eng. Chem.* **15**, 86-91.

[133] Korenko, M.; Straka, M.; Szatmáry, L.; Ambrová, M.; Uhlíř, J. (2013) Electrochemical Separation of Uranium in the Molten System LiF-NaF-KF-$UF_4$. *J. Nucl. Mater.* **440**, 332-337.

[134] Kuznetsov, S. A.; Hayashi, H.; Minato, K.; Gaune-Escard, M. (2006) Electrochemical Transient Techniques for Determination of Uranium and Rare-Earth Metal Separation Coefficients in Molten Salts.

[135] Berthon, L.; Nikitenko, S. I.; Bisel, I.; Berthon, C.; Faucon, M.; Saucerotte, B.; Zorz, N.; Moisy, Ph.(2006) Influence of Gamma Irradiation on Hydrophobic Room-Temperature Ionic Liquids [BuMeIm]$PF_6$ and [BuMeIm]$(CF_3SO_2)_2N$. *Dalton Trans.* **21**, 2526-2534.

[136] Bossé, E.; Berthon, L.; Zorz, N.; Monget, J.; Berthon, C.; Bisel, I; Legand, S.; Philippe Moisy, P. (2008) Stability of [$MeBu_3N$][$Tf_2N$] Under Gamma Irradiation. *Dalton Trans.* **7**, 924-931.

[137] Venkatesan, K. A.; Jagadeeswara Rao, Ch.; Nagarajan, K.; Vasudeva Rao, P. R. (2012) Review Article: Electrochemical Behaviour of Actinides and Fission Products in Room-Temperature Ionic Liquids. *Int. J. Electrochem.* **2012**, 1-12.

[138] Banks, C. V.; Klingman, D. W. (1956) Spectrophotometric Determination of Rare Earth Mixtures. *Anal. Chim. Acta*. **15**, 356-363.

[139] Bell, J. T.; Biggers, R. E. (1967) The Absorption Spectrum of the Uranyl Ion in Perchlorate Media. *J. Mol. Spectrosc.* **22**, 262-271.

[140] Kondo, H.; Matsumiya, M.; Tsunashima, K.; Kodama, S. (2012) Attempts to the Electrodeposition of Nd from Ionic Liquids at Elevated Temperatures. *Electrochim. Acta*. **66**, 313-319.

[141] Jagadeeswara Rao, Ch.; Venkatesan, K. A.; Nagarajan, K.; Srinivasan, T. G.; Vasudeva Rao, P. R. (2011) Electrodeposition of metallic uranium at near ambient conditions from room temperature ionic liquid. *J. Nucl. Mater.* **408**, 25-29.

Curriculum Vitae

Graduate College
University of Nevada, Las Vegas

Janelle Elizabeth Droessler

Degrees:

Bachelor of Science – Chemistry, 2009
Bachelor of Arts – Interdisciplinary Studies: Forensic Science, 2009
University of Nevada, Las Vegas

Publications:

Mausolf, E.; Poineau, F.; Hartmann, T.; Droessler, J.; Czerwinski, K. (2011) Characterization of Electrodeposited Technetium on Gold Foil. *J. Electrochem. Soc.* **158**, E32-E35.

Mausolf, E.; Poineau, F.; Droessler, J.; Czerwinski, K. (2011) Spectroscopic and structural characterization of reduced technetium species in acetate media. *J. Radioanal. Nucl. Chem.* **288**, 723–728.

Mausolf, E.; Droessler, J.; Poineau, F.; Hartmann, T.; Czerwinski, K. (2012) Tetraphenylpyridinium Pertechnetate: A promising salt for the immobilization of technetium. *Radiochimica Acta* **100**, 325-328.

Hatchett, D. W.; Droessler, J.; Kinyanjui, J. M.; Martinez, B.; Czerwinski, K. R. (2013) The Direct Dissolution of $Ce_2(CO_3)_3$ and Electrochemical Deposition of Ce Species using Ionic Liquid Trimethyl-n-butylammonium bis(trifluoromethanesulfonyl)imide containing bis(trifluoromethanesulfonyl)imide. *Electrochimica Acta* **89**, 144-151.

Pemberton, W. J.; Droessler, J.; Kinyanjui, J. M.; Czerwinski, K. R.; Hatchett, D. W. (2013) Electrochemistry of soluble $UO_2^{2+}$ from the direct dissolution of $UO_2CO_3$ in acidic ionic liquid containing water. *Electrochimica Acta* **93**, 264-271.

Droessler, J. E.; Czerwinski, K. R.; Hatchett, D. W. (2014) Electrochemical Measurement of Gold Oxide Reduction and Methods for Acid Neutralization and Minimization of Water in Wet Ionic Liquid. *Electroanalysis* **26**, 2631-2638.

Patent:

Hatchett, D. W.; Czerwinski, K. R.; Droessler, J. E., Kinyanjui, J. M. (2014) Room temperature electrodeposition of actinides from ionic solutions. Patent Ref: WO 2014124428 A1

Dissertation Title: Direct Dissolution and Electrochemical Investigation of Cerium and Uranium in Ionic Liquid

Dissertation Examination Committee:

Co-Chair, Kenneth Czerwinski, Ph.D.
Co-Chair, David Hatchett, Ph.D.
Committee Member, Ralf Sudowe, Ph.D.
Committee Member, Patricia Paviet, Ph.D.
Graduate Faculty Representative, Jaci Batista, Ph.D.